Extracting Primary Mechanical Neural Cellular Injury Thresholds Following High-rate Mechanical Deformations

by

Harry C. Cramer III

B.S., University of California - Merced, USA, 2014

Submitted in partial fulfillment of the requirements

for the Degree of Doctor of Philosophy in

Biomedical Engineering at Brown University

Providence, Rhode Island

February 2022

This dissertation by Harry C. Cramer III is accepted in its present form by the School of Engineering as satisfying the dissertation requirement for the degree of Doctor of Philosophy.

Date _____ _____

Christian Franck, Ph.D., Advisor

Recommended to the Graduate Council

Date _____ _____

Kareen Coulombe, Ph.D., Reader

Date _____ _____

David L. Henann, Ph.D., Reader

Date _____ _____

Diane Hoffman-Kim, Ph.D., Reader

Approved by the Graduate Council

Date _____ _____

Andrew G. Campbell, Ph.D.
Dean of the Graduate School

Abstract of "Extracting Primary Mechanical Neural Cellular Injury Thresholds Following High-rate Mechanical Deformations" by Harry C. Cramer III, Ph.D., Brown University, December 2021.

The successful detection and prevention of traumatic brain injuries relies on the quantitative identification of cellular injury thresholds associated with the underlying cellular pathology. First, a 3D *in vitro* cell culture platform will be described capable of being reproducibly mechanically deformed and efficiently immunolabelled for cytoskeletal markers of interest in diverse neural cell structures. This work will then combine recently developed inertial microcavitation rheology techniques with a 3D *in vitro* collagen-I hydrogel-based neural tissue model to provide the first quantitative experimental mechanical injury tolerance thresholds for neural cells at strain rates on the order of $10^3 - 10^8\ s^{-1}$. In this work the structural pathology of neural cells following inertial cavitation-induced mechanical deformations are resolved to allow for the quantification of critical injury strain thresholds of neural cell populations occurring at high loading rates such as those encountered in blast, cavitation or directed energy exposures. Specific thresholds for cellular projections are determined and indicate that neuronal dendritic spines characterized by MAP2 display the lowest physical failure strain at 7.3%, whereas general neural cellular projections containing microtubules and filamentous actin were able to tolerate appreciably higher strains (14%) prior to injury. Interestingly, while these critical injury thresholds were similar to previous literature values reported for moderate and lower strain rates (< 100 1/s), the pathology of primary injury reported here was distinctly different by being purely physical in nature as compared to biochemical activation during apoptosis or necrosis. The work concludes with the discussion and examination of primary mechanical injury in an integrin-rich hydrogel substrate to inform the future extension of high-rate mechanical neural cell injury to the regime of secondary biochemical injury activation through more diverse mechanotransduction pathways.

Curriculum Vitæ

Harry was born in Manchester, Connecticut, and raised in various locations across the United States. He received a Bachelor of Science degree in Bioengineering from the University of California, Merced in 2014. Prior to graduate school Harry worked at the Stem Cell Instrumentation Foundry under Anand Gadre, Ph.D. In the fall of 2015, Harry started doctoral research under Prof. Christian Franck in the Biomedical Engineering program. Outside of the laboratory, he acted as supplemental teaching assistant for one semester and as an instructor for Summer at Brown class for high school students for two years. The final years of his graduate career were spent as a visiting scholar at the University of Wisconsin-Madison in the Mechanical Engineering department where he was repeatedly invited to lecture on the topic of Hydrogel molding for classes on biomedical device design.

Refereed Journal Articles

(These authors contributed equally^{+})

Yang J, **Cramer III HC**, Bremer E, Buyukozturk S, Yin Y, Franck C. "Mechancical Characterization of Agarose Hydrogels and their Inherent Dynamic Instabilities at Ballistic to Ultra-high Strain-rates via Inertial Microcavitation." Extreme Mechanics Letters. December 2021, 101572, DOI: https://doi.org/10.1016/j.eml.2021.101572

Cramer III HC^{+}, Estrada JB^{+}, Buyukozturk S, Scimone MT, Franck C, "Neural cell injury pathology due to high-rate mechanical loading", Brain Multiphys., 2, 2021, 100034

2021. DOI: https://doi.org/10.1016/j.brain.2021.100034

Yang J, **Cramer III HC** , Franck C, "Extracting non-linear viscoelastic material properties from violently-collapsing cavitation bubbles." Extreme Mechanics Letters, 39: 100839. September 2020. DOI: https://doi.org/10.1016/j.eml.2020.100839

Sadick JS, Crawford LA, **Cramer III HC**, Franck C, Liddelow S, Darling E. "Generating cell type-specific protein signatures from non-symptomatic and diseased tissues". Ann Biomed Eng, April 2020, DOI: https://doi.org/10.1007/s10439-020-02507-y

Scimone MT, **Cramer III HC**, Hopkins P, Estrada JB, Franck C, "Application of mild hypothermia successfully mitigates neural injury in a 3D in vitro model of traumatic brain injury". PLOS ONE. 15(4): e0229520. April 2020, DOI: https://doi.org/10.1371/journal.pone.0229520

Scimone MT, **Cramer III HC**, Bar-Kochba E, Amezcua R, Estrada JB, Franck C, "Modular approach for resolving and mapping complex neural and other cellular structures and their associated deformation fields in three dimensions". Nature Protocols. 13, pp. 3042–3064. December 2018, DOI: https://doi.org/10.1038/s41596-018-0077-7

Polineni V, Romero S, **Cramer III HC**, Rodriguez M, Mann J, Huynh L, Gadre Anand. "Quantitative relationship between electrospinning parameters and fiber diameters of SU-8 and poly(lactic-co-glycolic acid) nanofibers". Advanced Science, Engineering and Medicine, Volume 6, Number 10, October 2014, pp.1086-1091(6). DOI: https://doi.org/10.1166/asem.2014.1621

Forthcoming Refereed Journal Articles

McGhee A^{+}, Yang J^{+}, Bremer E, **Cramer III HC**, Xu E, Franck C. "Full-field Deformations Measurements of Inertial Cavitation in Soft Materials using Digital Image Correlation". *In Preparation, 2021*

Conference Proceedings

(Oral Presentation*, Poster Presentation+, Conference Paper†)

†Yang J, **Cramer III HC**, Buyukozturk S, Franck C. "Probing Material Damage after Violently Collapsing Cavitation in Soft Viscoelastic Materials". In *Conference Proceedings of the Society for Experimental Mechanics*, 2022.

McGhee A+, Yang J+,*, Bremer E, **Cramer III HC**, Xu E, Franck C. "Inertial, Full-field Deformation Measurements of Inertial Cavitation in Soft Matter Using Embedded Speckle Plane Digital Image Correlation". Society for Experimental Mechanics Annual Conference (SEM), June 2022.

†Yang J, Yin Y, **Cramer III HC**, Franck C. "The Penetration Dynamics of a Violent Cavitation Bubble through a Hydrogel-water Interface". In *Conference Proceedings of the Society for Experimental Mechanics*, 2022.

Yang J*, **Cramer III HC**, Buyukozturk S, Franck C. "Probing inertial cavitation damage in viscoelastic hydrogels using dynamic bubble pairs". Society for Experimental Mechanics Annual Conference (SEM), June 2021.

Yang J*, Yin Y, **Cramer III HC**, Franck C. "The Penetration Dynamics of a Violent Cavitation Bubble through a Hydrogel-water Interface". Society for Experimental Mechanics Annual Conference (SEM), June 2021.

†Yang J, **Cramer III HC**, Franck C. "Dynamic Rugae Strain Localizations and Instabilities in Soft Viscoelastic Materials During Inertial Microcavitation". In *Conference Proceedings of the Society for Experimental Mechanics*, 2021.

Yang J+, Tzoumaka A, **Cramer III HC**, Murakami K, Johnsen E, Henann DL, Franck C. "Predicting Non-spherical Instability Shapes of Inertial Cavitation Bubbles in Viscoelastic Soft Matter". Society of Engineering Sciences (Virtual Session), 2021

Cramer III HC*, Estrada JB, Franck C. "Neural Cell Injury Pathology due to High-rate Loading from Blast or Directed Energy Exposures" Military Health Systems Research Symposium, August 2021

Yang J*, **Cramer III HC**, Franck C. "Dynamic Rugae Strain Localizations and Instabilities in Soft Viscoelastic Materials During Violent Inertial Microcavitation". Society of Engineering Science (SES), Virtual conference, October 2020.

Yang J*, **Cramer III HC**, Buyukozturk S, Franck C. "Extracting Nonlinear Viscoelastic Soft Material Properties from Inertial Micro-Cavitation bubbles". 5-th Annual UW-Madison Postdoctoral Research Symposium, September 2020. **Best Poster Award!**

Yang J*, **Cramer III HC**, Buyukozturk S, Franck C. "High Strain Rate Characterization of Soft Materials via Laser Induced Inertial Microcavitation Rheometry". ociety of Engineering Sciences, May 2019

Cramer III HC*, Estrada JB, Franck C. "Cavitation induced neural cell injury as a model of blast traumatic brain injury". Biomedical Engineering Society, October 2019

Koumlis S, Lamberson L, Rahaman M, Kesari H, González-Cruz RD, Hoffman-Kim D, Fawzi AL, Malave S, Szalkowski R, Hovey C, Wright-Carlsen R, White T, Adnan A, Rudraraj S, **Cramer III HC**, Scimone MT, Chukwu A, Summey L, Franck C. Physics-based neutralization of threats to human tissues and organs. Military Health Systems Research Symposium, August 2019

Cramer III HC^{+}, Estrada JB, Franck C. "Neural cellular response to cavitation-induced directed energy hazards". Military Health Systems Research Symposium, August 2019

Yang J, Estrada JB, Buyukozturk S, **Cramer III HC**, Franck C*. Inertial microcavitation in soft materials. American Physical Society, March 2019.

Cramer III HC^{+}, Estrada JB, Scimone MT, Franck C. Inertial Microcavitation as a neural cell damage mechanism in a 3D in vitro model of traumatic brain injury. Biophysical Society, February 2018

Sadick JS*, Crawford LA, **Cramer III HC**, Franck C, Darling EM. Assessing neural cell heterogeneity in Alzheimer's disease systems. conference abstract. Development & 3-D Modeling of the Human Brain, 2017

Estrada JB*, **Cramer III HC**, Scimone MT, Franck C. Microcavitation as a neural cell damage mechanism in an in vitro model of blast traumatic brain injury. Society of Engineering Science, July 2017

Estrada JB*, Scimone MT, **Cramer III HC**, Hopkins PR, Johnsen E, Franck C. Microcavitation as a neuronal damage mechanism in an in vitro model of blast traumatic brain injury. Society of Engineering Science, October 2016

Scimone MT*, Levine A, Estrada JB, **Cramer III HC**, Hopkins PR, Franck C. Quantifying hypothermia treatment efficacy on 3D neuronal cultures following traumatic brain injury. Biomedical Engineering Society, October 2016

Phong A^{+}, **Cramer III HC**, *et.Al.* Use of electrospun nanofibers to promote osteogenic differentiation of adipose-derived human mesenchymal stem cells. University of California - Merced's Research Week 2013

Cramer III HC^{+}, Romero S, Fernandez A, *et. Al.* Development of electrospun nanofibers to promote osteogenic differentiation of human adipose derived mesenchymal stem cells. California Research Symposium, Fresno, California. 2012

Acknowledgements

The roundabout route to my doctorate is one full of people to whom I owe an exceeding amount of gratitude, many more than I can mention here. To everyone who I have had the pleasure of working alongside academically from undergrad to my many friends in graduate school as well as those who led to the person I am today, you have my sincerest thanks.

To my wonderful committee members, Kareen Coulombe, Diane Hoffman-Kim, and David Henann. Without all of you, and the "sometimes" stress-inducing committee meetings and exams we shared, I sincerely doubt the rigor with which I approached this thesis work would have been possible. Your feedback and guidance throughout this journey has been immeasurably helpful and I am grateful you all could share in this work with me.

To the Franck Lab at Brown University, I put this in single space explicitly to have space to thank you each personally. You all made my time in this process remarkable and I can't thank you all enough, you're all family to me.

To Jon, I owe you more than I can put into words, you and Danielle made me feel truly at home in Providence. I am so incredibly lucky to have had you as my senior student and mentor in the lab. I am the scientist I am today because of you, thank you.

To Lauren and by extension Adam (and Mazie), your friendship is a literal cornerstone of this thesis, without you it would not have been possible. I would have gone insane during this process if not for rock climbing and Sunday morning brunch & Youtube *a la* Adam. You've grounded me when I needed it and been a constant source of support. Thank you for everything.

To Mark, your guidance and your insistence upon the biological side of our research has been a guiding force with which I approached this thesis. I will very fondly remember trivia nights at Round the Corner, and ping-pong here at UW. Thank you for being such an exceptional role model for this process for me, I have tried (and failed) to remain as effortlessly level-headed as you managed. Thank you.

To Mohak, your constant cheerfulness and levity in every situation made the move to UW bearable. Your facilitation of some of the most ludicrous debates over what constitutes a sandwich, or whether math was a language or the basis of the universe will be remembered fondly. Thank you for all the help you provided to make this thesis happen.

To Alex, your beta breaking rock climbing and your ability to pull random facts out of thin air has been nothing short of inspirational. I greatly appreciate your friendship and all of the guidance you provided in my classes. Thank you.

To Selda, my sister in arms, we did it! We made it... we're here! Thank you for all your help and friendship. I will remember our time in the lab together fondly, I'll see you in Boston!

To the Franck Lab at Wisconsin, I may just be getting to know you all, but your friendship means a great deal to me. You're all phenomenal individuals and I'm positive that your time in the Franck lab will be as enjoyable as mine has been, I promise that isn't a threat, you're all in for a wonderful journey together. I hope this document proves useful to you all as you begin your journeys towards your degrees.

To Christian, your guidance through this process has been exceptional, even if at times you had to tell me what I needed but didn't want to hear. I am extremely fortunate to have benefited from your optimism and general know-how on all things experimental and solid mechanics. You have provided me with every opportunity to become a better scientist, researcher, and general student of the world and I am truly grateful for our time together. Your belief in me has never wavered, and I cannot tell you how much it has meant to me. Thank you for everything.

To my amazing parents, despite moving on my birthday, you're all a pretty cool bunch. You both played a larger role in the development of this thesis than you know. I love each of you with all my heart. Mom, your patience and generosity truly knows no bounds and I am incredibly lucky to have you. Thank you for always 'encouraging' me to do pretty much everything that got me to where I am today. Dad, your weird engineering mentality has without a doubt been a guiding inspiration for my career path. Sorry I strayed into the 'weird squishy stuff' but the world of solid objects that behave as one would anticipate is boring.

To my siblings, despite living eleven-hundred to two-thousand miles away, you've all managed to have my back when I needed it. I appreciate each of you weird individuals immensely, and am grateful that despite the distance we are all just about as annoying when I left California for Rhode Island. Thank you all for everything up to now and for all that I am sure is to come.

To the infallible Kaylee, I would be remiss not to acknowledge my rock. You may only have a passing understanding of the English language but I will thank you here anyway. You've been a great comfort throughout the past 8 years of my life and have seen me through an incredibly trying experience. I look forward to spending the rest of your life paying you back with treats, belly pats, and walks. I love you pup.

And finally, To Adrienne. I could not have asked for a more wonderful friend and partner to go through the past nearly six years with. You've been an incredible confidante and shoulder to lean on and I cannot imagine having gone through this process with anyone but you. I'm incredibly proud of everything we've gone through and look forward to finding new adventures to surmount. Thank you for everything.

To my family and friends, thank you

Contents

List of Tables

List of Illustrations

Chapter 1

Introduction

Note: Portions of this chapter are in preparation for publication and may be reproduced at a later date.

1.1 Traumatic Brain Injury

Traumatic brain injuries (TBI) are a result of complex mechanical insults to the nervous system and represent a significant economic and societal burden [1]. Global estimates indicate that as many as sixty-nine million individuals suffer a TBI each year [2]. Despite years of research and mounting evidence towards a number of potential treatment avenues, no Federal Drug Administration approved treatment currently exists to treat TBIs [3]. To facilitate an understanding of the mechanisms underlying TBIs, a multitude of past and present efforts, both experimental [4–8] and model-based [9–12], have aimed to develop platforms intended to predict and mitigate the injury altogether. Despite progress, these efforts have failed to readily translate into a clinical setting where assessment of the severity of a TBI continues to rely on the use of the Glasgow Coma Scale (GCS) [3, 13]. The GCS assigns patients a numerical score (3-15) based on the presentation of neurosymptomatic effects following injury (e.g., loss of consciousness) [2]. According to a patients GCS score, TBI severity is designated a clinical assessment of mild (13-15), moderate (9-12), or severe

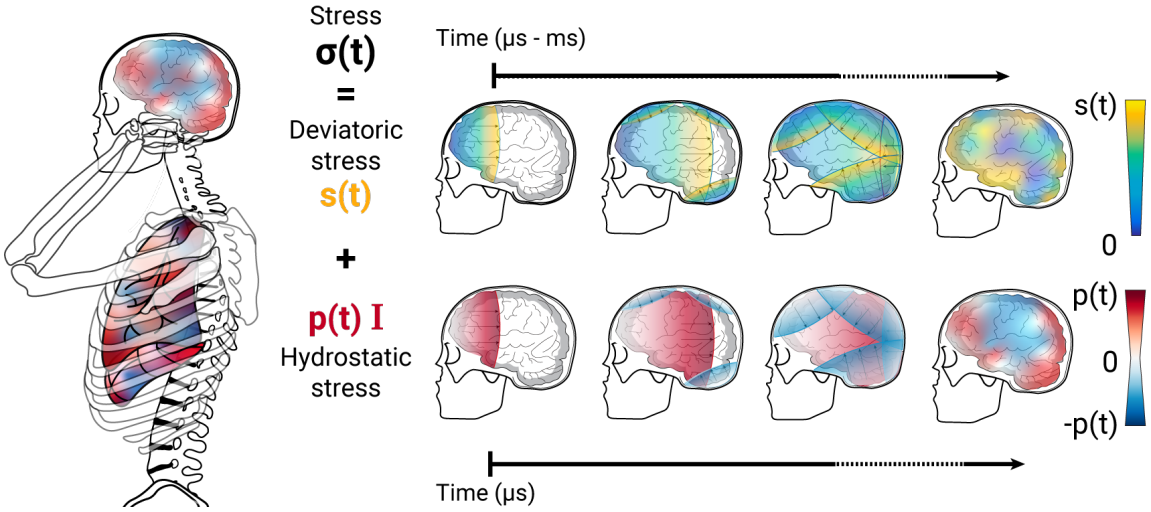

Figure 1.1: **Schematization of Stress Wave Propogation through tissue in TBI** From a mechanical standpoint this stress wave can be considered to consist of two major (potentially injurious) contributing portions of the stress wave, the deviatoric (yellow) and hydrostatic (red) components.

(3-8) [2]. This rating is assigned from primarily neurosymptomatic presentation in the field and corroborated clinic-side through costly medical imaging, with confirmational diagnosis often relying on postmortem analysis [3]. Traumatic brain injuries present under a broad array of symptoms, some of which present rapidly, like those of 'open' head injuries where the scalp or skull is penetrated [3]. The rapidly presenting injury pathologies which occur within the immediacy of impact, often termed primary injury, consist of both 'open' and 'closed' presentations on the order of microseconds to milliseconds. In addition to rapidly presenting pathologies, the disruption of blood vessels in the brain can lead to a secondary injury pathology including; edema, intracerebral or subarachnoid hemorrhages, and hematomas over the course of hours to days following the initial injury [3]. As TBI is at its core a soft tissue injury, the presentation of neurosymptomatic, or pathological effects originate at the cellular scale through an abnormal mechanical loading of the tissue.

While mechanical forces play a key role in many cellular functions, an excess or abnormal loading on the cellular scale can be distinctly injurious [4–8]. The mechanical loading causal to a TBI, regardless of the intial injury source, can be understood as the propagation of a stress wave through the tissue. From a mechanical standpoint this stress wave can be considered to consist of two major (potentially injurious) contributing portions, the deviatoric and hydrostatic components (Figure 1.1). Transmission of these different components

of stress through the tissue provide for different potential mechanisms of injury. Deviatoric stress relates a direct deformation-based injury modality to the tissue, whereas the hydrostatic stress relates a change in overall pressure on the tissue and cells. While the potential negative effects of a direct deformation on a tissue can be understood from an engineering perspective similarly to that of a material being deformed to failure when a critical load is applied, the effect of pressure on the tissue is more nuanced and is examined in more detail below.

To quantify the mechanical deformations experienced at the cellular scale in response to these stress waves, an understanding of the underlying mechanics is required. The magnitude (or intensity) of the stress wave in the tissue is considered an 'inferred' mechanical quantity, meaning that it is not a direct measure of an observable mechanical phenomenon, but rather a numerical representation of a more complex loading state. In this way the mechanical stress, or the force generated over a given area of the tissue, is dependent on the directly observable rate of deformation (strain rate) and the deformation (strain) itself, in addition to an assumed functional response of the material (tissue) to the measured deformations (material model). Within the context of engineering, the deformations—or shape changes—within a tissue can be mathematically described as material strains through a number of definitions and are described at length elsewhere [14]. As a consequence of inferred mechanical stress being dependent on the implementation of specific material models, many experimental (including this thesis) and analytical approaches to studying the effects of deformations in tissues report the directly quantifiable strains and strain rates in the system, rather than reporting mechanical stress. Commonly applied definitions for the reporting of strains in tissue and cell mechanics are varied and can include the logarithmic (true, or Hencky), engineering (Cauchy), or maximum principle strains (MPS), among others. These definitions each reflect related, but mathematically distinct, representations of the applied or measured strains within the system. Further discussion on the specific mathematical definitions and formulations for strain, strain rate, and stress employed in this thesis are described at length in Chapter 3 Section 3.3.

Consistent with this approach, in order to examine the transmission of stress waves

through the bulk tissue in greater detail as well as to highlight the effects of the rate of applied loading, modeling efforts traditionally construct homogenized geometric computational frameworks with unit sizes on the millimeter (mm) to centimeter (cm) scale [9–12]. These models are commonly informed with rate-dependent material properties of the tissue and/or surrogate tissue mimics consistent with an understanding that materials and tissues behave differently under increasing loading rates [9, 11, 15]. Exposure of these models to simulated injury sources at under different loading rates yield complex maps of various mechanical quantities throughout the tissue (i.e., mechanical strain, strain-rate, stress, pressure, etc.) indicating the intensity of many quantitative metrics vary both spatially and temporally within the tissue [9, 11]. One major shortcoming of these models is their limited predictive power with respect to the loads experienced at the cellular scale (order micrometer; μm). These models indicate that the loads experienced by the brain differ greatly with several factors, including the rate of the applied loading regime [9, 11]. Interestingly, several models and experimental platforms employing high-rate deformations from exposure to purely pressure-based shock or blast waves indicate that pressure drops experienced by the brain can reach levels sufficient to generate a tensile fluidic breakdown of the cerebrospinal fluid resulting in a potentially highly disruptive nucleation of cavitation, or spontaneous bubble formation, events within the tissue [16, 17].

The finding of differing behavior of the modeled tissue at different rates is in good general agreement with clinical observations of the postmortem pathology of different types of closed-head cortical injury (CCI) [18]. Under histological examination, a unique rate-dependent injury pathology has previously been reported between different rate CCIs [18]. Historically, pathological examination has shown that the hallmark pathomorphological presentation of CCI is the presence of focal swellings along neural cellular projections over time following injury, often referred to as 'blebbing' [19, 20]. Repeated exposure to head impacts (e.g., sport-related head contact) has additionally been shown to be positively correlated with later secondary development of significant tauopathy and reactive gliosis [21, 22]. Examination and spatial localization of these pathologies within the brain plays a critical role in the confirmational diagnosis and the delineation of severity for the neurosymptomatic

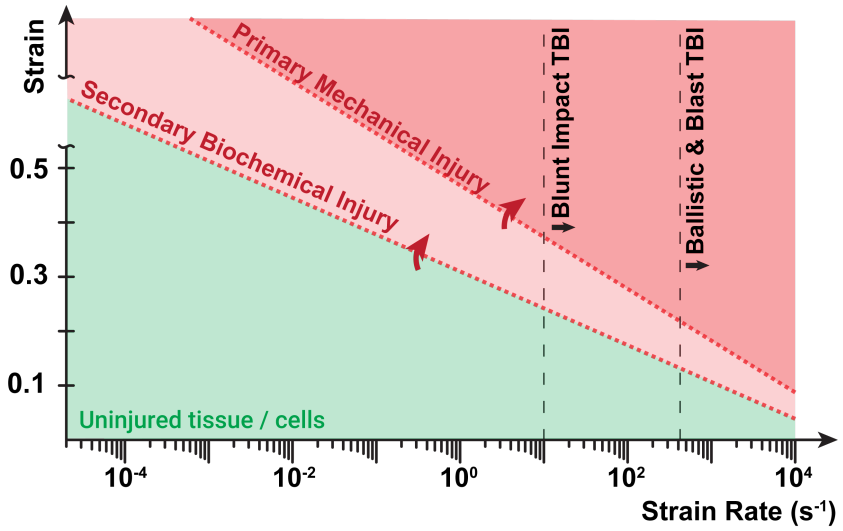

Figure 1.2: **Experienced Injury Type as a result of Mechanical Strain and Strain Rate** The delineation of strain-based injury tolerance thresholds for primary (mechanical) or secondary (biochemical) injury pathology is dependent on the strain rate of the applied loading. High strain rate deformations of cells and tissues display differing strain tolerance thresholds when compared to low strain rate injury [4, 24–26]. The presentation of mechanical and biochemical injury phenomena in *in vitro* models similarly display a rate dependence at similar strain magnitudes [4, 25].

presentation of several neurological disorders [23]. Histological comparisons performed by Shively et. al. of single and chronic blunt TBI to those having been exposed to single, or repeated exposure to high-rate blast events detail previously unreported focal scarring at interfaces and within the parenchyma of the brain [18]. These trends, highlighted in Figure 1.2, further re-enforce the importance of mechanical loading rate on CCI outcomes.

With the effects of loading rate on brain injury becoming more widely observed, TBI can be more specifically, and usefully, classified with respect to different rate-dependent loading regimes. Broadly, TBI can be considered to originate in several ways including, blunt loading (at rates of order 10^0-10^2 1/s), ballistic loading (at rates of order 10^2-10^4 1/s), and blast loading or directed energy hazards (at rates greater than order 10^4 1/s) as highlighted in Figure 1.3 [27, 28]. The examination of these different regimes has revealed a number of clinical pathologies to be positively correlated with previous diagnosis of TBI including; Chronic Traumatic Encephalopathy [19,21,29,30], and Alzheimer's Disease [19,21]. However, at present these conditions are typically diagnosed and assessed neurosymptomatically with their full cellular mechanisms remaining incompletely understood. To expand our current understanding of high-rate injuries at the cellular scale, the work presented in this thesis

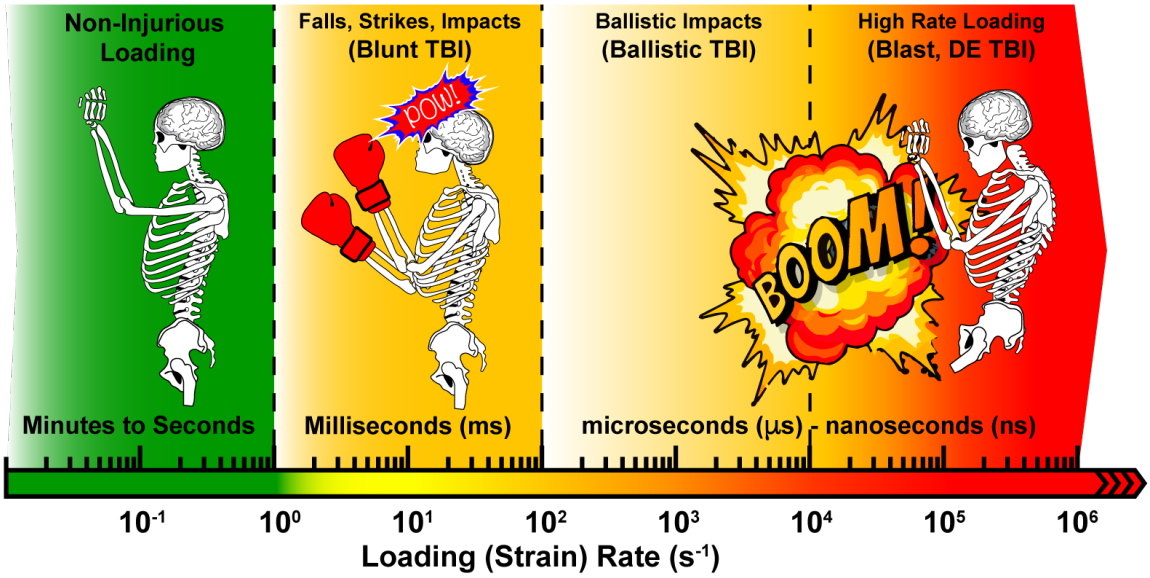

Figure 1.3: **Loading Rate-dependent Classification of Traumatic Brain Injury** The delineation of traumatic brain injury by the type of causal mechanical exposure presents important information to the type of injury pathology that may present within the immediacy of injury as well as over time following exposure. TBI can be considered to originate in several ways including, blunt loading (at rates of order 10^0-10^2 1/s), ballistic loading (at rates of order 10^2-10^4 1/s), and blast loading or directed energy hazards (at rates greater than order 10^4 1/s) [27, 28].

employs localized high strain, high strain rate (10^3 – 10^6 1/s) mechanical deformations consistent with loading rates expected to occur in CCIs of blast and directed energy-based TBIs.

1.1.1 Blast & Directed Energy-based Traumatic Brain Injury

Blast-induced TBI (bTBI) originates from the exposure of the brain to high-rate shock waves and associated comorbid injuries originating from blast events (e.g., improvised explosive devices (IEDs), explosive ordinance, etc.) [27, 31]. Blast TBI is generally divided into four subcategories termed: primary, secondary, tertiary, and quaternary blast injury [27]. These subcategories are broken down as follows: primary (non-penetrating) injury corresponds to the passage of a blast wave through a tissue leading to injury; secondary injury where foreign objects are brought into contact with the body leading to injury; tertiary injury where the body is brought into contact with a surface/object like a vehicle or wall; and quaternary injury which encompasses all other associated injurious effects (e.g., smoke inhalation, and

thermal injuries) [27]. Despite awareness and efforts to treat mental health conditions associated with brain injury since WWI, TBIs did not become a focus of military medicine until the 1990s [27]. Blast TBI has only more recently become a specific focus of medical research during the U.S. wars in Iraq and Afghanistan with the increased risk of exposure to Coalition warfighters with an increased use of IEDs in conflict zones [32]. The Defense Veterans Brain Injury Center indicates that during the wars in Iraq and Afghanistan 2,700 U.S. troops have experienced a mild TBI, with hundreds of thousands (at least 30% of active combat troops) having experienced a TBI as a result of exposure to IED blast waves [32].

Attempts to understand and study bTBI classically attempt to isolate each individual injury type to assess the effects of the different portions separately [33,34]. For example, primary injury is typically studied in model systems with use of shock-tubes where experimental systems are exposed to simplified waveforms generated through either compressed-gas or the detonation of small explosive charges distal to the sample [33,35]. These experimental waveforms attempt to replicate open-field exposure to shockwaves by generating a single large amplitude pressure pulse, or over-pressure, followed by a negative pressure region [31]. The full waveform persists for several milliseconds and is commonly described by the Friedlander waveform [31]. Early work has indicated that the full extent of the neurosymptomatic effects observed in bTBI cannot be explained fully by the exposure to a peak over-pressure alone [18, 27, 31]. Changes in hydrostatic pressure on cells have been shown to result in a heterogenous and temporary cessation of cellular signaling and neuronal activity [36]. Additional experimental and modeling work has indicated that through the spallation and reflection of pressure waves within the head the generation of cavitation, or spontaneous bubble nucleation within the tissue, is possible [9, 31]. Inertial cavitation events are well known to the physics community to be highly destructive and could, in theory, result in significant local material deformation at high strain rates within the brain [37].

Pressure changes and the induction of cavitation within tissues, specifically within the central nervous system (CNS), have recently become the subject of much conjecture with the advent of the novel neurological syndrome, Havana Syndrome [38, 39]. Havana Syndrome, first reported in U.S. diplomats in Cuba in 2016, is speculated to be the result of the targeted

attacks through the use of sonic or microwave weapons platforms, and has led to a resurgence in interest to understand the effects of directed energy weapons systems on the human body [38]. Directed energy (DE) weapons systems consist of a family of platforms involving the weaponized use of focused sonic, laser, or microwave irradiation technologies [38–40]. Despite the controversial nature of both cavitation in the brain, and Havana Syndrome, the effects of focused energy technologies are quite well qualitatively understood when harnessed intentionally [39]. The use of focused (directed) energy technologies in medical applications is increasingly widespread. Techniques such as diagnostic [41–43] and therapeutic ultrasound [44–47] and laser-based ablation methods [48, 49] are commonly used in an array of medical procedures, from tumor resection to corrective surgery for glaucoma. Despite the qualitative understanding and use of DE in medicine, little is quantitatively known about the injurious mechanisms employed in these techniques on tissues [50]. In these techniques, the focused use of the destructive power of cavitation and the high strain rates imparted to target tissues is well documented, however, only recently has exploration into their use in the brain begun [51].

The neurosymptomatic and pathological presentation of directed energy TBI has been described as unique from that of low-rate TBI similarly to the unique presentation of blast exposure [18, 38]. With the increased focus on high-rate loading, it is then also important to understand how these loads are physically experienced by the cells; to this end an understanding of the structural arrangement of the cells of interest and their cytoskeletons must be examined.

1.2 The Structural & Cytoskeletal Organization of the Neuron

Within the nervous system the neuron is generally considered the principle functional unit and is the focus of discussion for a large portion of the peer-reviewed literature studying the cellular effects of TBI [4, 7, 52–54]. When considering the effects of a mechanical load on the CNS as a complete soft tissue, however, it is important to concern ourselves with not only the neuron, but also the supporting cells of the brain like glia, myelinating cells (e.g.,

oligodendrocytes in the CNS), as well as the diverse vasculature that supports the demands of the highly metabolically active brain [55]. As the predominant type of cell employed in the *in vitro* hydrogel models discussed throughout this thesis is the neuron, the discussion in this section will focus on the description of stereotypical neuronal structure and cytoskeletal organization [56].

To discuss the injurious effects of abnormal mechanical loading on the neuron it is important to understand the physical organization of both the neuronal structure and its cytoskeleton. The structure of the neuron is dependent on several factors including the origin of the cell (e.g., the central or peripheral nervous system; PNS), as well as the signaling target distal to the cell body (i.e., the structure and organization of an interneuron differ from that of an efferent neuron originating in the motor cortex) [57]. Many in-depth reviews and texts are available which provide examinations of the organization and function of the cytoskeleton of different types of neurons in much greater detail than will be discussed here [57, 58]. Beginning with the earliest description of neuronal form by Ramon y Cajol in 1909 the differentiation of neuronal type and function has been determined based on the overall form and structure of the cell [58]. This structural organization is often dictated by the cytoskeleton [57]. The cytoskeleton of any cell, especially the neuron, is a diverse interconnected network of filamentous and globular proteins that allow a cell to support complex functions both intra- and extracellularly. The cytoskeleton plays a major role in a wide array of cellular processes, including compartmentalization of the cell into functional units, intracellular organization of organelles, the trafficking of proteins, providing for structural integrity, the transduction of forces, in addition to many others. For brevity, discussion here will be limited to the organization of sub-compartments common to most neuronal sub-types with emphasis on several key cytoskeletal components and associated proteins.

1.2.1 The Structural Organization of the Neuron

The typical neuron can be subdivided into two major sub-compartments, a soma (or cell body) with many neurites (cellular projections) protruding from the cell body. A schematic of a stereotypical neuron and the structural organization as discussed in more detail below

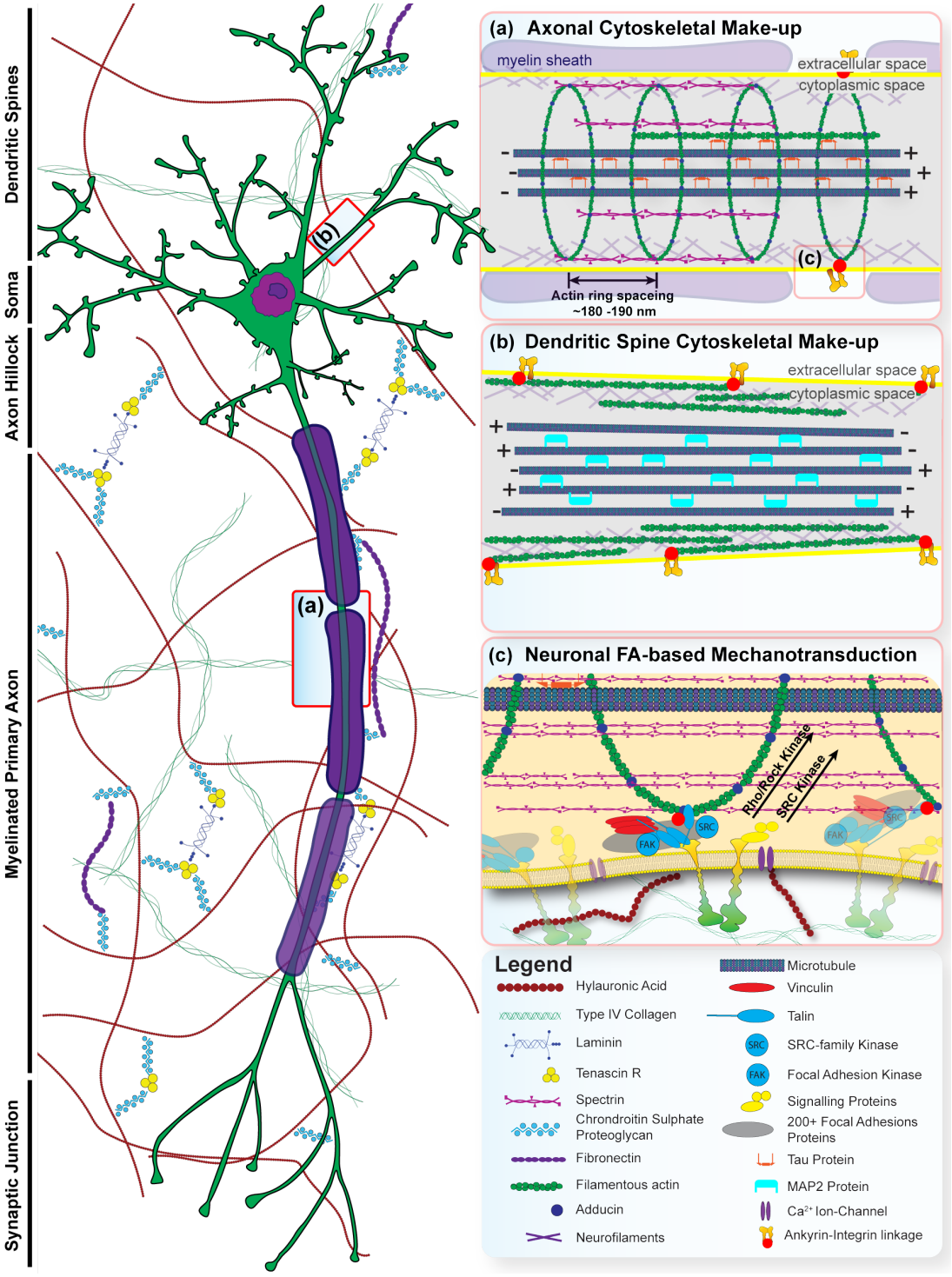

Figure 1.4: **Neuronal Superstructure and Cytoskeletal Schematic** Schematic overview of neuronal superstructure and cytoskeleton. Cytoskeletal organization of major cytoskeletal components in the (a)axon and (b)dendrites of a stereotypical neuron. (C) Schematic of cellular integrin connection to the ECM.

can be seen in Figure 1.4. The cell soma is home to major organelles like the nucleus and endoplasmic reticulum and handles most of the protein transcription and translation for the cell. The neurites fall into two families: the dendrites (Figure 1.4b), and the axon (Figure 1.4a) [57]. Dendrites are shorter, highly branched neurites extending from the soma enabling the cell to communicate with neighboring cells as a form of receiver network, providing for mostly incoming signal propagation, and limited outgoing signaling [57, 59]. Dendritic trees, often called dendritic arbors, are broader at the base and thin with each subsequent set of branches [59, 60]. Alternately, the axon extends from a large protrusion of the soma, termed the axon hillock, and forms a single long projection which forms few branches near its terminus at the synaptic junction. This junction acts as the primary avenue of outgoing signal transduction for the cell employing neurotransmitters as signaling molecules between the neuron and neighboring cells [57]. The axon, in addition to axonal bifurcations, maintain a relatively consistent caliber, or diameter, throughout its length [57]. In both the native CNS and PNS, the axon is usually wrapped in a myelin sheath by either oligodendrocytes or Schwann cells, respectively [57]. Myelination, coupled with a consistent axonal caliber, enables the axon to efficiently propagate voltage-based action potentials over great distances [61]. The delineation of these sub-compartments is primarily governed by the development of the cytoskeleton due to internal and external signaling queues during synaptogenesis and maturation of the cell [57]. The specific protein make-up of the cytoskeleton in these compartments is important for the specialization of neural cell types and sub-compartment specification [62].

1.2.2 The Neuronal Cytoskeleton

The cytoskeleton of the neuron consists of a mixture of microtubules (MTs), microfilaments, and intermediate filaments (IFs), in addition to an array of associated proteins organized to preform specific functions [57]. Microtubule filaments are hollow dimeric cylindrical filaments consisting of repeating units of α- and β-tubulin monomers [61, 63]. Commonly existing in a dynamic state of polymerization and de-polymerization, MTs develop a distinct polarity that serves as both a protein and organelle trafficking network in addition

to a structural element within the neuron [61, 63]. This polarity differs between axons and dendrites. Within the axonal sub-compartment, organization of MTs is such that the positive—or polymerizing—end of an individual MT is always oriented away from the soma towards the synapse [61, 63]. Microtubules form multi-filament bundles along the length of the axon connected by several protein families including the microtubule-associated protein (MAP) family [63]. Microtubules within the dendritic arbor are randomly oriented along the length of the projection and are in a constant state of rearrangement in response to cellular signaling [59,61]. As in the axon, MTs in the dendrite are associated as bundles and to other structural proteins through the MAP protein family [61, 62]. While the population of MAPs in the neuron is diverse, dendritic versus axonal sub-compartment identification is commonly achieved through the identification of specific MAPs within the cell (i.e., MAP2 is specific to dendrites, and Tau protein is specific to the axon) [57, 62, 63]. MT number and packing density within dendrites and the axon is dependent both on the type and function of the specific neuronal cell type being considered, though estimates indicate that axonal sections can maintain ∼10-100 MTs [63].

In addition to microtubules, microfilaments (e.g., filamentous actin; f-actin) play an important role in the maintenance of the neuronal cytoskeleton and on protein trafficking [57]. Filamentous actin, a major microfilament in the mammalian cells, is a linear polymer microfilament composed of monomeric globular actin (g-actin) and is associated with other cytoskeletal components including MTs and IFs through an array of accessory proteins including the MAP family [64, 65]. Seminal super-resolution microscopy examinations of the f-actin cytoskeleton by Xu et. al. in 2013 revealed a highly complex structural organization of f-actin within the mature neuron that differs with localization to either the axonal or dendritic sub-compartments [64]. The axon of the neuron contains f-actin in the form of uniformly spaced, concentric rings of f-actin filaments, associated with periodically spaced adducin proteins along their circumference (Figure 1.4a) [64]. These ring-shaped actin-adducin co-filaments form an alternating periodic structure with the actin-associated microfilament protein spectrin [64]. The resulting ring-to-ring spacing of this structure is ∼180—190 nm [64]. Organization of actin filaments in the dendrites of the neuron takes

the form of linear fibers aligned with the dendritic shaft that are closely associated to the plasma membrane (Figure 1.4b) [64, 66]. F-actin in the dendritic portion of the synapse, or the dendritic spine, forms short interconnected filaments closely associated with the ends of MTs and IFs [66, 67]. The microfilament-associated protein ankyrin serves to link actin filaments to the cellular membrane at focal adhesion sites, as discussed later [64].

The final major category of proteins that make up the neuronal cytoskeleton are intermediate filaments [57]. Intermediate filaments are a broad classification of filaments that form close associations with other cytoskeletal components within the cell. Several in-depth reviews of IFs are available that cover these components of the cytoskeleton in greater detail within neurons and glia [68, 69]. Intermediate filaments are highly specific to neural cell type and are commonly used in their delineation, as with glial fibrillary acidic protein (GFAP) used to identify astrocytes within culture [56]. Neurofilaments, a subset of highly cross-linked IFs, are long polymeric coiled proteins common to neural cells (including the neuron) [68]. An examination of neurofilaments (NF) within the neuron has shown that near the cell membrane IFs form a highly crosslinked mesh with α-internexin along the circumference of the axon [68]. The neurofilaments in this mesh have been shown to include neurofilament-light (NFL), neurofilament-medium (NFM), and neurofilament-heavy chain (NFH) [70]. NFs have been shown to play an important, but not exclusive, role in determining the diameter of the axon [70, 71]. NF localization within the neuron exist in many different phosphorylation states suggesting that NFs play a more complicated biological role than simply the maintenance of axonal caliber and represent an active area of research [70–72].

The dynamic cytoskeleton of the neuron is associated to the extracellular environment through several families of transmembrane proteins which govern the type of cellular interactions formed with the surrounding extracellular environment (i.e., cell-to-cell, or cell-to-extracellular matrix) [57, 73, 74].

1.3 The Cellular Interface with the Extracellular Space

The connection, and interaction, of a cell with the extracellular environment is controlled by several so-called protein 'superfamilies' that control cell-to-cell, cell-to-extracellular matrix (ECM), and cell signaling interactions [57, 73, 74]. These protein 'superfamilies' include cadherins, integrins, selectins, proteoglycans, and IgCAMs [57, 75]. Here, discussion will focus on a pseudo structural examination of major cell-to-cell (cadherin-based) and cell-to-extracellular matrix (integrin-based) interactions as the most thoroughly characterized avenues for biomechanical force transmission into and out of the cell [73, 74]. A complete understanding of the cellular interaction with the extracellular space should not, however, neglect the potential for force transmission from other protein 'superfamilies'. Nor neglect the role of cadherins and integrins in cellular signaling and functional specification with respect to cellular fate and function during injury in the native CNS or static *in vitro* cultures [73, 74]. A schematic of generalized integrin-ligand interactions can be seen in Figure 1.5; box (b), which ha been adapted from the literature to highlight the neuron specifically [73, 74]. Several excellent reviews of cadherin and integrin interactions exist that address cell adhesion in greater detail and are excellent references for understanding the complex protein interactions networks and signaling cascades that can occur within adherin junctions (AJ) and focal adhesions (FA) [73, 74]. A brief examination of integrins and cadherins will be presented here as a primer on the subject.

1.3.1 Cell-to-cell Connections Through Cadherins.

The cadherin 'superfamily' of transmembrane proteins is generally responsible for the formation of cell-to-cell adhesions known as the adherin junction (AJ), or the adhesome [74]. These proteins consist of an intracellular domain, a transmembrane domain, and five extracellular subdomains [74]. Prior to the formation of an initial cell-to-cell connection, cadherins exist dispersed across the cell surface [74]. Upon interaction with a cadherin of an adjacent cell the local concentration of cadherins increase reinforcing the junction through the formation

of additional interactions in a Ca^{2+}-dependent binding cascade [74, 76]. Subsequent recruitment of a multitude of proteins (∼170 reported; reviewed elsewhere [74, 76]) result in the formation of plaques at the intracellular domain of the cadherins which associate the AJ with internal cytoskeletal components including, f-actin, microtubules, intermediate filaments, and other intracellular structures [74]. While examination of the dynamic AJ-to-cytoskeleton structural connection remains incomplete, many cytoskeletal-associated proteins have been shown to inhabit AJs, reviewed in detail by Yonemura et. al. in 2011 [76]. Briefly, several notable actin- and microtubule-associated proteins have been shown to play critical roles in the connection of the AJ to the cytoskeleton for the transduction of forces [74, 76]. These include the accessory proteins α-catenin, β-catenin, p120-catenin, and vinculin [74, 77]. α-catenin, β-catenin, and vinculin have been shown to support a force dependent linkage in the association of the AJ with the f-actin cytoskeleton [76]. In this way, α-catenin is bound to intracellular domain of the cadherin, and β-catenin is bound to f-actin and are connected through a tension-dependent recruitment of vinculin to the AJ [77]. Microtubule connection to the AJ has been shown to include minus-end association of p120-catenin through several associated AJ components [74]. Further, β-catenin has been shown to associate with the plus-end of microtubules through dynein motor protein binding [74]. Notably, discussion here will neglect much of the well-documented role of motor proteins (e.g., myosin II/IV and dynein) in the AJ. Motor proteins have been shown to enable the generation of forces from the cell outward and play an important role in the maintenance of cortical tension [57]. Force transduction at the AJ is generally studied within the context of developmental biology and the potential role of cadherins as a force transduction pathway in TBIs is generally underrepresented in the literature [74, 76]. Much of the literature on force-based cellular injury in TBI is focused on *in vitro* models that rely primarily on integrin-ECM loading despite cellular density in the CNS being estimated to be of order 10^5 cells/mm^3 [78]. At this density of cells, force transduction through the AJ represents a potentially important avenue for force-dependent injury in these cells. This apparent bias is likely due to difficulties in generating and maintaining high cellular density experimental systems capable of faithfully replicating the native CNS ex vivo [78].

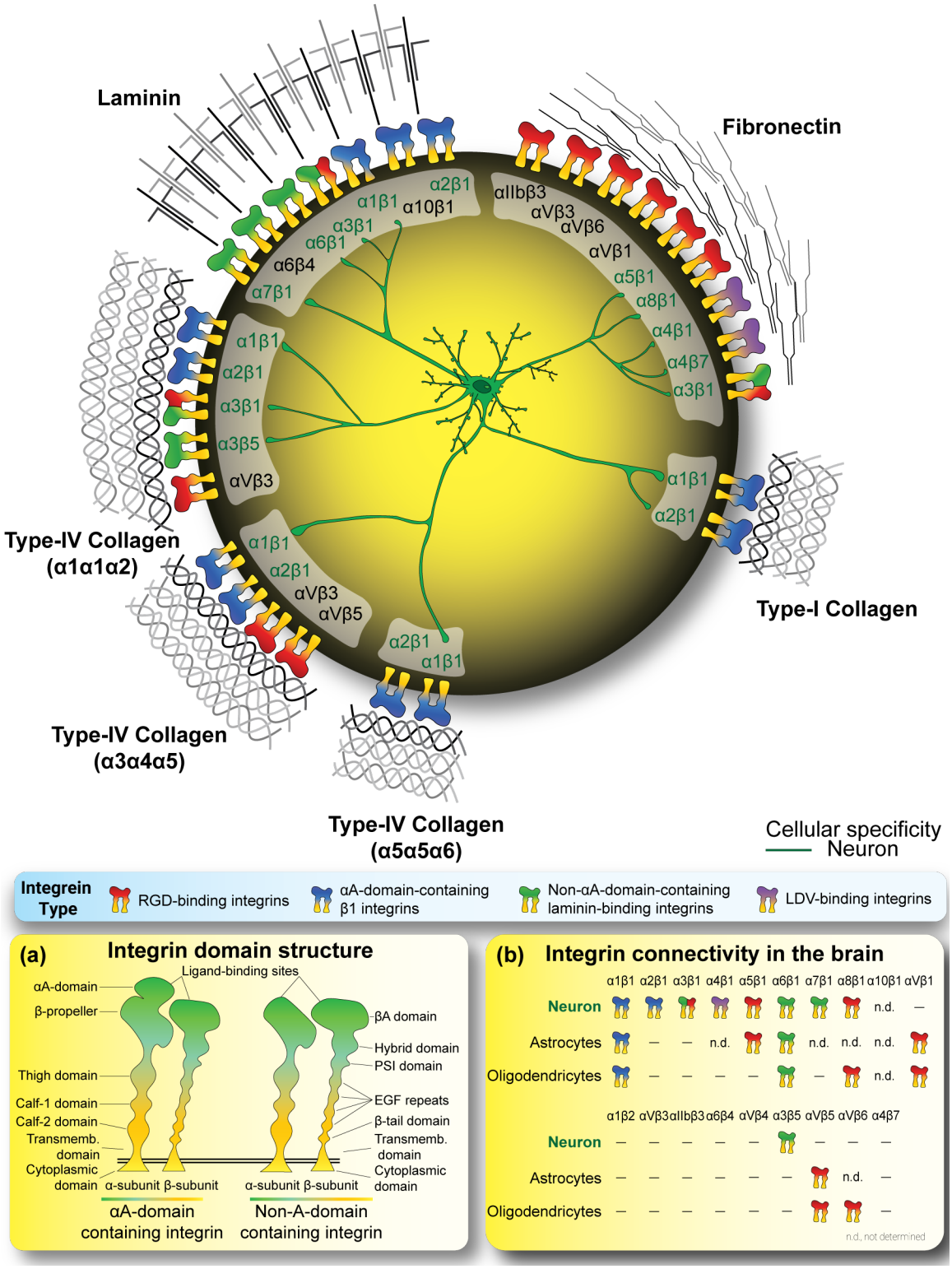

Figure 1.5: **Integrin Interactions within the Brain** (a) Integrin domain structure. (b) Integrin Connectivity in the brain. Adapted from [73, 74]

1.3.2 Cell-to-Extracellular Matrix Connections Through Integrins.

Similarly to that of the cadherin literature, integrin-based force transduction through the formation of focal adhesions is well documented and several substantial in-depth reviews of the subject are available [73, 79–81]. In contrast to cadherins which associate with like structures of an adjacent cell, integrin-based binding to the ECM is dependent on the presentation of a binding motif, or ligand, on an ECM protein in the extracellular space [73]. The specific constituents that make-up the extracellular space of the brain is dependent not only on the types of cells present, but the specific localization of the cells or structures of interest [82]. The extracellular space in the brain is believed to consist of approximately four-fifths cellular material with only one-fifth consisting of ECM proteins [83]. The specific localization and types of extracellular proteins have been discussed at length elsewhere [57]. Briefly, the neural ECM contains a spatially variant mixture of many proteins including fibronectin, laminin, collagen type-IV, and hyaluronic acid, in addition to various proteoglycans and linker proteins [84, 85]. As integrins are generally considered the primary mode of extracellular adherence for cells to the ECM, they exist in sufficient diversity as to match the diversity of ligands (i.e., ECM protein binding domains) that exist in biology [73]. Considering this diversity and the fact that this thesis focuses on cellular injury within the context of the CNS, the discussion in this section will be limited to the integrin-ligand interactions currently known to be available to cells in the CNS. Special emphasis will be placed on discussion of integrins shown to enable neuronal association with the ECM proteins.

Integrins are a dimeric transmembrane protein consisting of an of α and β subunit [73]. Each subunit contains a large extracellular domain, a single transmembrane domain, and a small intracellular domain [73]. There are currently a total of 24 α-β combinations that have been described at the protein level, a schematic of the structure of general integrin α/β pair can be found in Figure 1.5a. Integrins are separated into four families, those which are RGD-binding integrins, those that are LDV-binding, those containing an A-domain on the β1 subunit, and those that are non-αA-domain-containing laminin binding integrins [73]. Integrins capable of binding ligands of major extracellular matrix constituents of the neural microenvironment (18 known, in total) can be found summarized in Figure 1.5b, in addition

to the ligands available on collagen type I for cellular adhesion [86, 87].

As with cadherins, prior to contact with an appropriate ligand on the extracellular space, integrins exist as individual protein complexes dispersed across the cell membrane and upon binding recruit additional integrins to form a nascent, or early, focal adhesions [73]. The binding of an integrin to a ligand of the ECM is dependent on the presence of divalent cations (i.e., Ca^{2+}, and Mg^{2+}) [73]. As the focal adhesion develops, the cytoplasmic domain of the β subunit associates with intracellular proteins (over 200 known; reviewed elsewhere [88]) to form a plaque that associates the FA to the cytoskeleton [73, 89]. Most focal adhesions are believed to primarily associate with the f-actin cytoskeleton through 'anchor' proteins known to facilitate a force-sensitive linkage between the β subunit and the actin cytoskeleton [89]. Some of these anchor proteins include ankyrin, talin, filamin, and α-actinin which associate either directly with the f-actin cytoskeleton or indirectly through the recruitment of additional proteins like vinculin [73]. Many integrins are capable of binding to multiple ECM proteins through similarities in binding motifs expressed across many ligands' protein structure [57, 73]. For example, one of the most common integrin binding motifs is the tripeptide Arg-Gly-Asp (RGD) ligand motif, which many different integrins can associate to with varying degrees of affinity [73]. Integrins, as with all cell-to-extracellular space linkages maintained by neural cells, exist as an active signal transduction pathway modulating cellular responses to external stimuli and affecting the extracellular environment through the generation of forces [57, 73, 75].

While more broadly studied from an injury standpoint than the AJ, FA complexes remain primarily understood as a mechanotransduction signaling pathway from a homeostatic biology or force generation standpoint (Figure 1.4c) [75]. The literature understanding of FAs for the transduction of abnormal loading to a cell from the extracellular environment remains naïve [75]. Previous *in vitro* studies that rely on integrin-based associations of cells to substrates have examined the tensile response of neural cells to mechanical injury. These studies have shown that tensile deformations elicit increased levels of kinase activity, namely, SRC-kinase, and Rho/ROCK-kinase activity [90, 91]. Indeed, a wealth of literature exists indicating that abnormally large mechanical loading of cells can activate an array

of downstream biochemical pathway activities occurring over several hours following injury (e.g., generation of excess reactive oxygen species, and apoptosis) [4,7,75,92]. Despite these observations, the specific connection of downstream biochemical cellular injury pathology and its root mechanical deformation-based trigger remains, to date, largely unknown [75].

1.3.3 Electrostatic Gradient Modulation through Ion Channels

In addition to cytoskeletal association to the extracellular space through transmembrane proteins like cadherins and integrins, the cytoskeleton associates itself with the cellular membrane and associated transmembrane proteins like ion-channels. While this thesis does not specifically measure or assess signaling activity (or the disruption thereof), as a protein family that plays a critical role in neural cellular function this primer would be remiss to exclude the discussion of ion-channels as a potential mechanically sensitive source of cellular injury.

Ion channels, a type of transmembrane ionophore, as well as other cell membrane transport molecules are amphiphilic protein structures that facilitate the transfer of ions and proteins across the cellular membrane. In the neuron a diverse array of transmembrane proteins facilitate the generation and propagation of chemo-electric voltage potentials, or action potentials, over exceptionally long distances [57]. Stereotypically, an action potential is propagated along the axon to the synaptic terminal through a modulation of intra and extracellular concentrations of calcium, sodium, and potassium to generate a transmembrane electrical (voltage) potential [57]. At the synapse of the neuron and a neighboring cell these voltage potentials enable the release of various neurotransmitters, including glutamate, dopamine, and serotonin, among others into the extracellular space through voltage-gated channels [57]. Ionophores are a widely studied class of proteins; the general diversity, biochemical function, and the specific dysregulation of individual channels have been previously examined in detail elsewhere [93, 94]. For the purpose of this primer, discussion will be focused on general cell membrane biology with special emphasis placed on ionophores, like ion-channels.

As with the cytoskeleton, the organization, protein density, and diversity of ionophores

in the cell membrane vary spatiotemporally depending on both the type of neuron examined, and the specific extracellular cues an individual cell receives from the microenvironment [57]. Along the length of the axon, myelin sheaths envelope the cell membrane and partition regions of high-density ionophores into the so-called nodes of Ranvier [57]. This densification is believed to allow for more uniform signal propagation among other biological cues for the cell [57]. As a form of both incoming and outgoing signaling, the function of transmembrane proteins, including ionophores, in cell-to-cell communication provide essential chemical cues for neuronal survival [92]. Disruption to the proper function of ion channels, and more broadly, dysfunction of the cell membrane they inhabit are common targets used to assess the health of neural cell populations following injury [95, 96]. For example, the disruption of cellular signaling at high loading rates has been shown to exhibit a transient stall of signaling under high-rate blast conditions where it is theorized that dramatic variations in hydrostatic pressure disrupt the function of these proteins [36]. While several directly mechanically-gated ion channels in the CNS have been described (namely piezo1 and 2) which rely on mechanical force for normal operation, most ionophores have been shown to operate as forms of either active or passive membrane transport [97]. Despite the general mode of operation being typically chemical in nature, ionophores have been shown to closely associate with cell-to-extracellular space junctions and the cytoskeleton through proteins like ankyrin [57]. These close-associations have been shown to induce increased membrane transport in response to extracellular mechanical stimuli and the association of ionophores to cellular connections in the extracellular space serves to coordinate and support cellular signaling in different portions of the cell (e.g., Na+ and K+ ion channel localization in the nodes of Ranvier) [57].

In the TBI literature, disruptions to signal propagation have classically been demonstrated to be perturbed through a transient mechanical disruption, or poration, of the cell membrane [7, 95]. The cell membrane, consisting of a lipid bilayer, acts as a partially water-free exclusion layer between the cytoplasmic and extracellular spaces for the cell. The lipid bilayer is associated to the cytoskeleton through actin-associated proteins like ankyrin, and directly through associations to spectrin I/II molecules [57]. This attachment is not fixed

in nature, but instead the lipid bilayer allows for lipid-flow and the diffusion and recruitment of many lipid-bound and transmembrane proteins across the surface in a fluid-like manner [57]. A disruption to the membrane integrity through mechanical force, or so called mechanoporation, allows for the free flux of ions across the normally semi-permeable cell membrane resulting in disruption of ion gradients and a dysregulation of cellular signaling capabilities [95]. It remains an area of active interest to determine both the amount and type of abnormal mechanical loading that disrupts cellular signaling and results in significant negative biochemical pathway activation beyond which a cell cannot recover.

1.4 Accomplishments

This thesis presents the first quantitative experimental measurements of neural cellular projection and structural failure providing unprecedented levels of new detail into the cellular pathology of neural cells affected by high-rate injury. The thresholds derived in this work represent the first experimentally derived quantitative high-rate injury threshold metrics for neural cell and major neural cellular cytoskeletal components including filamentous actin, β3-tubulin, and microtubule associated protein 2 (MAP2) at average loading rates on the order of 10^3 - 10^3 s^{-1}.

Chapter 2 provides in-depth protocols for the creation of healthy 3D *in vitro* collagen-I-based hydrogels of interconnected neural cells are explored. Furthermore, protocols for the non-destructive immunological examination of large hydrogel constructs is described, allowing for the preservation of spatial fidelity with respect to the deformed cellular configuration in injured cellular constructs. It then provides an exploration of the inertial cavitation experimental platform employed as primary mode of cellular injury in this thesis. Finally, the general governing assumptions of the inertial microcavitation analytical framework are described to validate the selection of data for continued analysis as described in detail in chapters 3.

Chapter 3 utilizes the experimental methodologies expanded upon in Chapter 2 to describe the first experimentally derived high rate neural cellular injury tolerance thresholds.

The radius of total cellular disruption, R_{PI}, under high rate cavitation-based mechanical loading is described. Immunological staining protocols are employed to highlight the cytoskeletal architecture of neural cells in order to quantify the stretches, strains, and strain rates required for neural projection failure. Discussion of the susceptibility of different sub-cellular compartments to mechanical stretch-induced failure is examined through immunolabeling of β3-tubulin and MAP2. Finally, estimates of stress-based cellular injury tolerance thresholds are provided.

Chapter 4 opens the primary injury thresholds, explored in Chapter 3, to the discussion of more complex cellular microenivronments through the incorporation of a Matrigel-based 3D *in vitro* cell culture model. The efficacy of Matrigel platforms for neural cell culture and cavitation-driven high rate mechanical deformations are considered and the feasibility of continued use of this platform is discussed. Observations of the integrin-dependence of primary mechanical injury, as in chapter 3, are examined and show good general agreement with previously established trends.

Chapter 5 summarizes the thesis and discusses suggestions for future examinations of relevant topics for neural cellular injury delineation.

Chapter 2

Extended Methodology for Inertial Microcavitation-assisted high-rate mechanical loading of cellular constructs

Note: Portions of this chapter have been published. All data and figures included are done with co-authors' consent.

Scimone MT, **Cramer HC III**, Bar-Kochba E, Amezcua R, Estrada JB, Franck C. "Modular approach for resolving and mapping complex neural and other cellular structures and their associated deformation fields in three dimensions". *Nat. Protoc.*, Volume 13, 3042–3064, 2018, DOI: 10.1038/s41596-018-0077-7.

Estrada JB[1], **Cramer HC III**[1], Scimone MT, Buyukozturk SB, Franck C. "Neural cell injury pathology due to high-rate mechanical loading". *Brain Multiphys.*, Volume 2, 2021, 100034, DOI: 10.1016/j.brain.2021.100034.

Yang J, **Cramer HC III**, Franck C. "Extracting non-linear viscoelastic material properties from violently-collapsing cavitation bubbles". *Ext. Mech. Lett.* Volume 39, September 2020, 100839. DOI:10.1016/j.eml.2020.100839

2.1 Introduction

High fidelity *in vitro* studies of TBI can offer high throughput, and highly controllable environments with repeatable outcomes. To date, many conventional *in vitro* methods utilize two-dimensional (2D) culture environments, which have been shown to be incapable of reproducing some of the salient features of neural structures found *in vivo*. 2D models do not accurately represent the interstitial space of the brain, where neuronal cells exist in a 3D interwoven mesh [98,99]. To better model the structure of the brain, there have been many 3D *in vitro* neuronal culture systems documented, ranging in complexity [100]. Organotypic slices (sometimes categorized as *ex vivo* because they are obtained from a live animal) contain the same architecture as the native brain, only lacking vasculature perfusion; accordingly, they are an attractive culture platform [101,102]. Self-organized organoids are an alternative model that have been shown to recapitulate much of the complexity observed during brain development [103–105]. Whilst organotypic slices or *in vivo* systems can replicate the *in situ* brain structure, heterogenous loading can be experienced on a cell-to-cell basis, which can make correlations of biological outcomes to measures of cellular strain challenging.

Many in-vitro neuronal models are established by seeding cells into a 3D matrix of extracellular matrix (ECM) proteins. Many different scaffold materials have been used (see the book chapter by LaPlaca et al. in [78] for a table of examples) including synthetic polymers such as polydimethylsiloxane (PDMS) [99] and poly(L-lactic acid) (PLLA) [106], and biological substrates, such as Matrigel [78], different types of collagen [107], and laminin in conjunction with other substrates like PDMS and microbeads [107–109].

3D *in vitro* hydrogel models that use Matrigel [6] can achieve a cell viability approaching 95% [78]. However, Matrigel consists of isolated basement membrane and can vary in relative protein and growth factor concentration. Furthermore, the presence of different fibers

can lead to local inhomogeneities in both the distribution of the physical structure of the gel as well as in the distribution of ligand density and type. The native brain consists of primarily hyaluronan, proteoglycans, and tenascins, with small amounts of other adhesive proteins such as fibronectin and laminin. Moreover, in some regions, the composition may be much more complicated and varied, with at least 17 different matrix proteins occupying the brain ECM in some way [109]. Some research suggests that a substantial amount of mechanosensing and mechanotransduction in the brain occurs intercellularly through connexins or pannexins [109–112]. To achieve physiologically matched intercellular mechanotransduction the seeding density needs to be much higher. However, regions of necrosis can be a problematic obstacle in 3D *in vitro* systems with very high seeding densities that rely solely on diffusion for nutrient delivery.

Because our study required the imaging and resolution of single cells by confocal and multiphoton microscopy, we selected an optically transparent scaffold material in which to grow our cells [113]. We used primary cortical tissue, harvested from the basal forebrain from P0-P2 Sprague-Dawley rats embedded in a 3D collagen-I hydrogel. In addition to being optically transparent, type-1 collagen was used because the fibers form a relatively homogeneous substrate that neurons and glial cells alike can bind to using the canonical $\alpha1\beta1$ and $\alpha2\beta1$ integrins. Using immunofluorescence staining, and confocal or multiphoton microscopy these cultures have been shown to contain mature neurons, astrocytes, and neural progenitors as seen in Figure 2.1. The concentrations and antibodies to label cell can be found in Table 2.1 The culture contains some cells which co-express $\beta3$-tubulin and nestin, markers that have been historically classified as neuron-specific and progenitor-specific, respectively. Co-expression of nestin and $\beta3$-tubulin has been shown to occur in class III rat cells found primarily in the basal forebrain and in differentiating neuronal cells in the human subventricular zone [114, 115]. Staining of cells harvested using this protocol but plated on a 2D surface of laminin showed a limited number of cells positive for CD11B and O1, indicating the presence of microglia and oligodendrocytes. However, these cells were not observed in the 3D collagen gels.

Table 2.1: **Immunolabeling probes for cell typing**

Antibody Target	Species	Manufacturer	Catalog No.	Conc.
Primary Antibodies				
anti-β3-tubulin	Mouse (IgG)	Biolegend	801201	1:100
anti-GFAP	Rabbit (IgG)	Aligent Tech.	Z0334	1:100
anti-O1	Rabbit (IgG)	EMD Millipore	MAB344	1:500[a]
anti-nestin	Rabbit (IgG)	EMD Millipore	MAB353	1:100
anti-CD11b	Rabbit (IgG)	EMD Millipore	CBL1512	1:500[a]
Secondary Antibodies				
Anti-Rabbit AF488	Goat	ThermoFisher Sci.	A11008	1:200
Anti-Mouse Cy5 AffiniPure	Goat	Jackson Im. Res.	115-175-146	1:200

[a]Concentrations referenced are for 2D immunostaining staining, These cell types were not observed in 3D

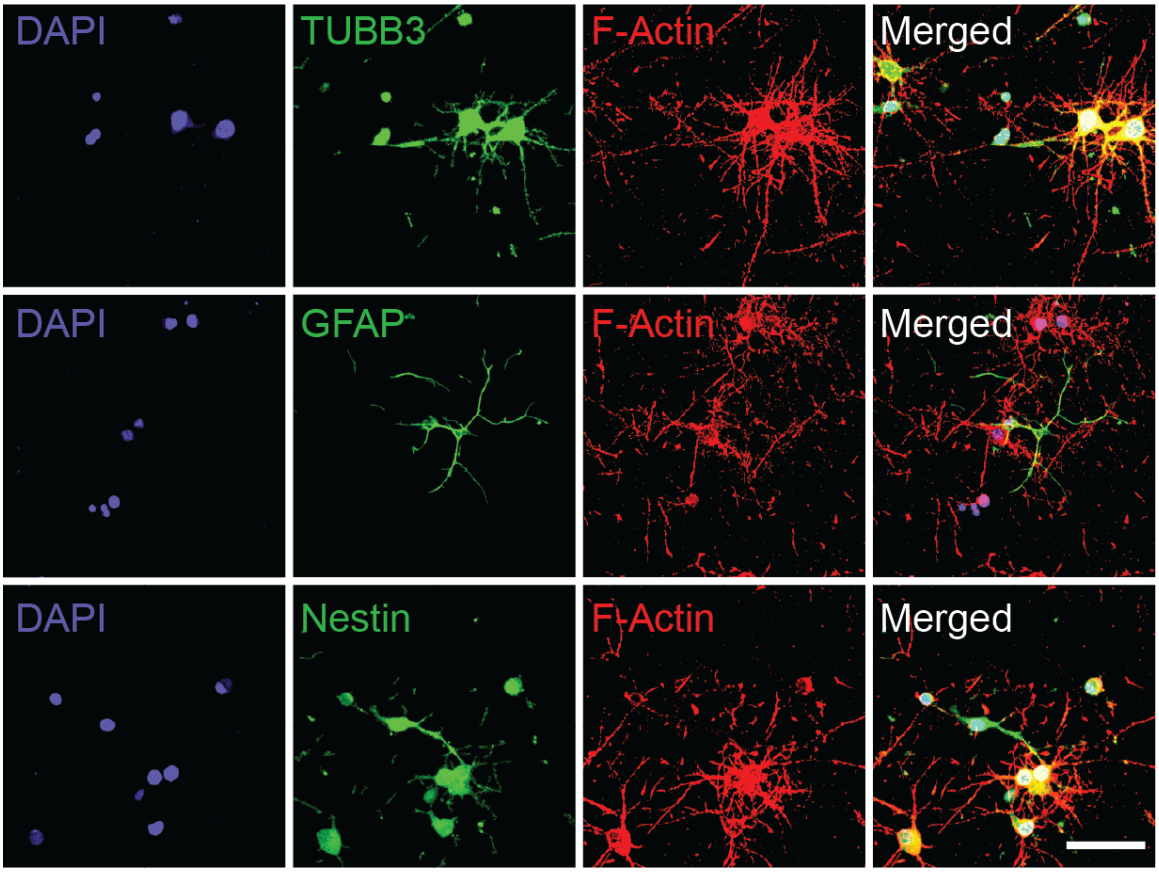

Figure 2.1: **Maximum intensity–projected confocal micrographs showing immunofluorescent signals of cells.** Cells positive for β3-tubulin (TUBB3; green), a neuronal-specific marker; GFAP (green), an astrocytic-specific marker; and nestin (green), a marker specific to neural progenitors, are shown. All cells were counterstained with phalloidin (red) to show the actin cytoskeleton and DAPI (blue) to show the nucleus. Scale bar, 50 μm. Reproduced from Scimone et al. *Nat. Protoc.* 2018 [56].

A potential criticism of the culture platform we use is that collagen-I does not appear natively in the brain. However, neurons and glial cells can bind to collagen-I via the $\alpha 1\beta 1$ and $\alpha 2\beta 1$ integrins [86, 87, 116, 117]. Mechanotransduction through this integrin has been well documented [118–120] and collagen-I has been used widely as a scaffold in 3D *in vitro* cultures in the past [121–124]. The homogeneity of the hydrogel leads to high levels of experimental repeatability. However, this simplification does not truly represent the heterogeneous tissue architecture found in the brain. The ECM of the brain is quite heterogeneous, resulting in each cell's connectivity being potentially unique, the implication being that vulnerability to mechanical insult can vary [120]. By using collagen-1, we ensure that the population is experiencing homogeneous loading. In doing so, our model affords an attractive repeatability for investigating neuronal injury from a reproducible mechanical standpoint.

2.2 Formation of large 3-dimensional collagen type I hydrogel-based cellular constructs

2.2.1 Cell Culture Platform

The hydrogel platform used in the majority of this thesis is a collagen-I hydrogel cast in the inset wells of a glass-bottomed 48 well plate (Mattek, Ashland, MA). The resulting hydrogel is a 6 mm in diameter, and $\sim$ 2 mm in height cylinder and does not require chemical adherence to the glass-bottom of the well plate. It is of note that, as with the use of Matrigel in chapter 4, the culture system will support all hydrogel cell culture systems, provided they polymerize sufficiently to fill the inset well. As compared with the cell culture platform outlined in Scimone et al. *Nat. Protoc.* 2018 that this platform is based on, the smaller sample geometry employed in this work negates the nutrient diffusion limitation issue present in larger free-standing hydrogels that results in a large necrotic core in the center of the sample [56]. The glass-bottom of the imaging dish is a No. 1.5 coverslip, which while optically transparent can present slight issues with light penetration for extremely

Table 2.2: **Reagent List for Dissection, Culture and Immunostaining Protocols**

Reagent	Manufacturer	Catalog No.
Type-I collagen, rat tail	Corning	354236
No 1.5 glass-bottom multiwell plate	Mattek	P48G-1.5-6-F
Papain (lyophilized)	Worthing Biochemical	LS0003120
Paraformaldehyde (20% (v/v)	Thermofisher Sci.	50-980-493
Phosphate buffered Saline (1X)	Thermofisher Sci.	70011044
Hibernate-A media	Thermofisher Sci.	NC9063747
Hibernate-A ($-CaCl_2$) media	Thermofisher Sci.	HACA
B-27 supplement (50X)	Thermofisher Sci.	17504044
Dulbecco's Modified Eagle Medium	Thermofisher Sci.	12430054
L-Glutamine	Thermofisher Sci.	25030081
Penicillin–streptomycin	Thermofisher Sci.	01378016
Neurobasal-A medium	Thermofisher Sci.	10888022
GlutaMAX	Thermofisher Sci.	35050061
Fetal Bovine Serum	Thermofisher Sci.	10437010
Sucrose	Thermofisher Sci.	S3-500
Triton X-100	Sigma-Aldrich	T8787
Sodium hydroxide (1M)	Sigma-Aldrich	221465
Bovine Serum Albumin	Sigma-Aldrich	A4737

sensitive assays.

2.2.2 Isolation of primary P0-P2 Sprague-Dawley cortical neural cells

The dissection protocol, and its individual steps are described in detail, and troubleshooting steps are provided in the *Nature Protocols* publication for this portion of the chapter. All commonly used solutions are described in Table 2.3, and all required materials are provided in Table 2.2. Briefly, P0-P2 Sprague-Dawley rat pups are euthanized according to IACUC approved protocols from the University of Wisconsin, Madison and Brown University. Pups are cold anesthetized for at least 20 minutes prior to euthanasia through cervical dislocation.

The brain is then removed from the skull under a dissection microscope. The hemispheres are separated from the cerebellum and the meninges removed in a bath of cold Hibernate A media (Thermo Fisher Scientific) supplemented with 2% (v/v) B-27 supplement and 0.25% (v/v) Glutamax (Fig: 2.2). The isolated cortices are then cut into three to four pieces, placed in a solution of Hibernate A -$CaCl_2$ media (Thermofisher Scientific) with 2 mg/mL

Table 2.3: **Reagent Setup for Dissection & Cell culture Protocols**

Reagent	**Instructions**
HA-B-27 media	2% (vol/vol) B-27 and 0.25% (vol/vol) GlutaMAX in Hibernate-A (HA) medium; store the medium at 4°C for up to 1 week
DMEM slurry	Filter DMEM through a 0.22-m filter. DMEM slurry is 2%(vol/vol) L-glutamine, 1% (vol/vol) pen–strep, and 10% (vol/vol) FBS in DMEM; store DMEM slurry at 20°C for up to 1 year from most recent manufacture date
Cortical Base Media	filter Neurobasal-A medium through a 0.22-m filter. Cortical base medium (CBM) is 1% (vol/vol) pen–strep and 0.25% (vol/vol) GlutaMAX in Neurobasal-A medium; store the medium at 4°C for up to 1 year from the most recent date of manufacture among its ingredients
Cortical Complete Media	2% (vol/vol) B-27 and 1% (vol/vol) DMEM slurry in CBM; make the medium fresh for dissection. Store it at 4°C for up to 1 week
Papain solution	8 mg of lyophilized papain (wt/vol) in 4 mL of HAMC per brain. A separate tube for each brain is ideal. Prepare the solution fresh and vortex it.
Fixation buffer	8% (wt/vol) sucrose and 4% (vol/vol) paraformaldehyde in 1×PBS; store the buffer at 4°C for up to 1 week
Phosphate Buffered Triton-X	0.5% (vol/vol) Triton X-100 in sterile 1× PBS; store PBT at 4°C.
Blocking Buffer Solution	10% Bovine Serum Albumin in 1×PBS. Store at 4°C for up to 1 week
Washing & Staining Buffer Solution	0.5% Bovine Serum Albumin in 1×PBS. Store at 4°C for up to 1 week

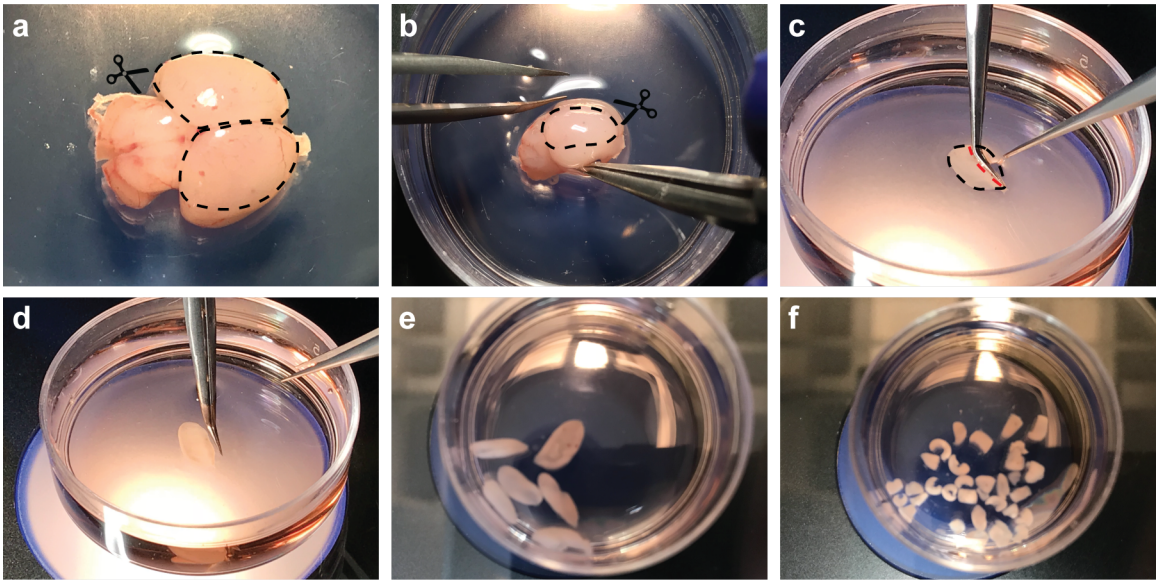

Figure 2.2: **Images of critical steps during dissection and sample preparation.** a, Black dotted lines indicate where to separate hemispheres. b, Black dotted line shows the ridge above the entorhinal cortex for isolating the desired cortex region. c, Removal of the meninges is performed with tweezers. The black dotted line outlines the hemisphere, whereas the red dotted line indicates how far the meninges have been pulled in the image. d, Final isolated cortex with inner layers and meninges removed. e, A group of isolated cortices. f, Cortices minced before dissociation in papain solution. Modified from Scimone et al. *Nat. Protoc.* 2018

(w/v) lyophilized papain (Worthington Biochemical) and incubated at 37^{o}C for 30 minutes, agitating gently every five minutes. After incubation, 2 mL of supernatant are replaced with 2 mL of Hibernate A supplemented with B27 and Glutamax as before, the Ca^{2+} in the media will inhibit the enzymatic activity of the papain. Each tube is centrifuged at 150×g at room temperature ($\sim$ 20^{o}C) for 5 minutes, before the supernatant can then be removed, and the cell pellet resuspended in 7 mL total of cortical complete media (Table 2.3). Through a pre-wetted 40 μm cell strainer, the cell solution is filtered into a 50 mL conical tube. Once filtered the cell suspension should then be centrifuged at 150×g once again for 5 minute at room temperature. The supernatant can then again be removed and resuspended in 3 mL of cortical complete media before determining the cell density via manual or automatic cell counting

To determine the cell density using a hemocytometer, first dilute 50 μL of cell suspension in 450 μL of cortical complete media, with an additional 500 μL of Trypan Blue (Thermofisher Scientific). Allow this solution to rest $\sim$1 minute before carefully pipetting 10

μL of solution onto the hemocytometer grid, sandwich the solution between the grid and a glass coverslip and place on light microscope. Focus the microscope on one of the nine grids, consistently count every cell within the grid ignoring cells overlapping the outside edge of the grid, and then count every cell that appears dark blue and record these values. Repeat this procedure for at least three grid sections before calculating cell density as:

$$\text{Cell density} = \frac{\text{Total No. of cells} - \text{Total No. of Trypan Blue cells}}{\text{No. of grids counted}} * \text{dilution factor} * 10,000$$

where, the dilution factor is the volume of cell solution (10 μL) over the total mixture volume (1 mL), following these instructions results in a dilution factor of 20.

To prepare the final collagen-I/cell solution, Calculate the amount of collagen needed to obtain a final concentration of 2 mg/mL based on the initial concentration. Based on the amount of acetic acid in the collagen stock solution, the volume of 1 N NaOH needed to neutralize the solution is 0.023% (vol/vol), per the manufacturer's protocol. The remaining volume should be made up of PBS and the cell/CCM suspension, which should be diluted such that the seeding density is 3,750 cells/mm^3 [78]. For example one 48-well plate requires 2.88 mL of total collagen/cell mixture to fill at 60 μL per well. It is advisable to add $\sim$ 10% extra volume to avoid the injection of bubbles during mixture and polymerization. The pH of the mixture prior to pipetting into the well plate should be confirmed, the target pH should be $\sim 8 - 8.5$. It is important to note that pH, as with temperature, and collagen I concentration will effect the microstructure of the final polymerized gel. Once each inset well has been cast, allow the plate to polymerize at 37^{o}C and 5.0 % CO_2 for 20 minutes before covering carefully with 300 μL of cortical complete media. Samples should be fed after the first 24 hours and every 48 hours after that on a consistent schedule for at least seven days *in vitro* or until the desired day of use.

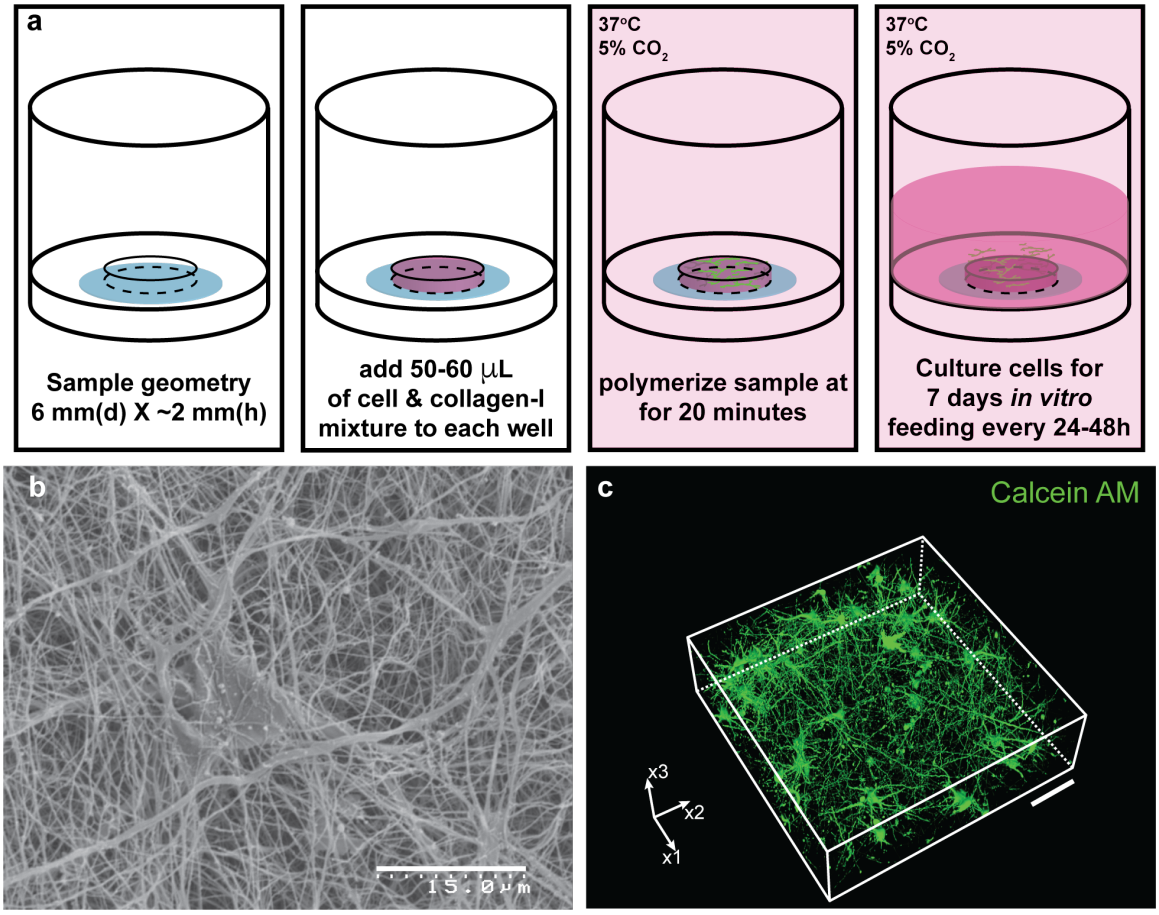

Figure 2.3: **48 well Plate Sample Making Procedure.** (a) multipanel sample making procedure for generation of 6 mm×2 mm cylindrical collagen-I hydrogels in the inset wells of a 48 well plate. 50-60 μL of cell/collagen-I solution is pipetted into the inset well and polymerized for 20 minutes in a humidity controlled incubator. Samples are cultured for 7 days *in vitro* and fed every 24-48 hours. (b) Scanning electron micrograph of the collagen architecture. Scale bar 15.0 μm. (c) 3D confocal micrograph of a network of cells stained with calcein-AM. Volume dimensions = 509 509 150 μm. Scale bar, 100 μm. Modified from Scimone et al. *Nat. Protoc.* 2018

.

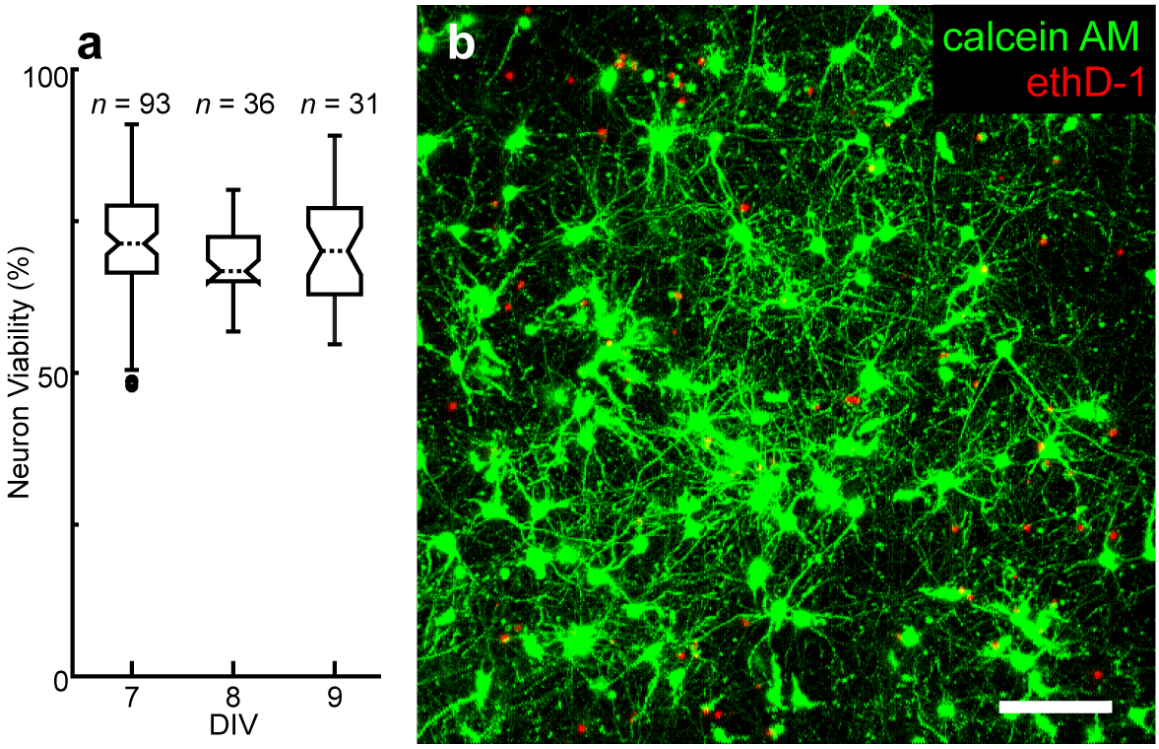

Figure 2.4: **Neural Cell Viability at 7,8,9 DIV.** (a) Box-and-whisker plot showing the control viability of the culture platform at 7 d *in vitro* (DIV; $n = 93$ distinct volumes), 8 DIV ($n = 36$), and 9 DIV ($n = 31$). No significant difference is seen between datasets using two-way ANOVA. Dotted bands: median; top and bottom boxes: upper and lower quartiles, respectively; whiskers: 5th and 95th percentiles.. (b) Representative maximum intensity–projected confocal micrograph of cell population after 7 d of culture. Healthy, live cells are stained green by calcein-AM, and dead cell nuclei are stained red by ethidium homodimer-1 (EthD-1). Scale bar, 100 μm. Reproduced from Scimone et al. *Nat. Protoc.* 2018 [56].

Successful completion of the cell culture protocol will yield a collagen I hydrogel with a viable interconnected network of cells consisting of neurons, astrocytes, and neural progenitors. See Figure 2.4b for a representative maximum intensity–projected confocal micrograph of cells stained with calcein-AM, as well as viability data (Figure 2.4a). Cells will form networks; for examples, see Figs. 2.3c and 2.4b. If the collagen concentration and polymerization environment (e.g., temperature, humidity, pH) are followed as described in this protocol, the gel should consist of a dense network of randomly oriented fibers averaging 175 nm in width. Collagen fiber width can be measured via scanning electron microscopy (SEM) and confocal reflectance imaging. The cells embedded can attach to collagen I via the $\alpha 1\beta 1$ and $\alpha 2\beta 1$ integrins. See Figure 2.3b for a scanning electron micrograph of a gel, which shows the collagen architecture.

2.3 Microscope-based laser-induced inertial microcavitation experimental platform

With a culture platform in hand, reproducing resolvable, high-rate mechanical deformations at the cellular level remains challenging. For example, traditional approaches for mechanically loading cellular constructs at high-rates (i.e., those relevant to blast TBI) generally rely on use of shock, or blast tubes [27]. These techniques employ shaped explosive charges, or pressure devices distal to the sample to deliver a pressure wave to load the sample and rely on external measurements of the shape of the applied pressure to relate sample injury to quantitative metrics [125,126]. As the measurement is distal to the sample, and the reference configuration of the cells within the tested cellular construct is unknown, quantitative cellular scale injury metrics are challenging to interpret [56]. Previous work has highlighted techniques for the segmentation of cells following mechanical injury *in vitro* [4,56], however, these techniques still primarily rely on measurements of cells with respect to their deformed, or post-injury configuration. In order to generate resolvable deformations at the cellular level, we turn to the recently developed experimental platform foundational to the Inertial Microcavitation Rheometry (IMR) technique [127]. This platform employs a laser-induced single-bubble inertial cavitation event to locally generate high strains at strain rates on the order of 10^3 to 10^8 s^{-1} [15, 127]. Further, by coupling the laser-induced cavitation system to an inverted microscope, the full sample history can be obtained through acquisition of reference multiphoton images, high-speed videography of the cavitation deformation, and multiphoton images of the cells in their deformed configuration post cavitation.

Briefly, laser-induced cavitation is generated through the deposition of spatially-focused laser energy into the focal plane of a sample. This laser energy causes the dielectric breakdown of the medium resulting the nucleation of a plasma within the material [127]. As the bubble rapidly expands and cools a subsequent recombination of the plasma into gaseous species occurs and the system reaches an eventual thermodynamic equilibrium with the surroundings at radius maximum of bubble expansion [127,128]. The expansion of the bubble to its maximum radius generates significant pressure differentials between the gaseous

mixture within the bubble and the surrounding microenvironment leading to an unstable mechanical equilibrium with the surroundings [127]. Once thermodynamic equilibrium with the surrounding material is achieved at maximum bubble radius, a combination of the pressure differential across the bubble wall and material stresses force the bubble to collapse and undergo an oscillatory behavior characteristic of cavitation dynamics [37, 127]. While the full time-scale of the inertial dynamics, as well as the dynamics themselves, are dependent on both the bubble size as well as the material properties being probed, experiments typical of this thesis reach a quasi-stable equilibrium radius on the order of 120 μs (Figure 2.5). An in-depth explanation of the Inertial Microcavitation Rheometry analytical framework is discussed in-depth elsewhere [127], and is expanded upon within the context of this thesis in Chapter 3. Here, we broaden the use of the IMR experimental platform from the quantification of material properties to perform high-rate deformations of neural cells to probe their mechanical failure criteria.

To make use of this technique to experimentally deform neural cells or to probe material properties, a laser-induced cavitation system is constructed on an optical breadboard coupled to a combined Nikon Instruments confocal & multiphoton platform. This is accomplished by aligning a high-powered q-switched Continuum Minilite II pulsed Nd:YAG laser (Continuum, San Jose, CA) to the microscope imaging optics. The Nd:YAG laser is frequency doubled to 532 nm in order to maximize the efficiency of light microscope optics, and is optically pathed co-linearly with an 635 nm continuous alignment diode (Thorlabs, Newton, NJ). An alignment diode is necessary to conveniently align the pulsed laser train through the microscope optical path, where optical access is limited. The Nd:YAG laser is passed through a 2-5X variable magnification beam expander (Thorlabs, Newton, NJ) in order to increase the beam width from it's native 3 mm diameter to a 15 mm diameter to fill the back aperture of the eventual target 20X magnification microscope objective (Nikon Instruments). Following beam expansion, the laser is passed through the back imaging port of a inverted Nikon TI2 multiphoton microscope base, and reflected to the back aperture of the imaging objective off a 532 nm notched-dichroic mirror (Semrock, Rochester, NY). The imaging objective focuses the laser light to a diffraction limited spot within the focal plane of the

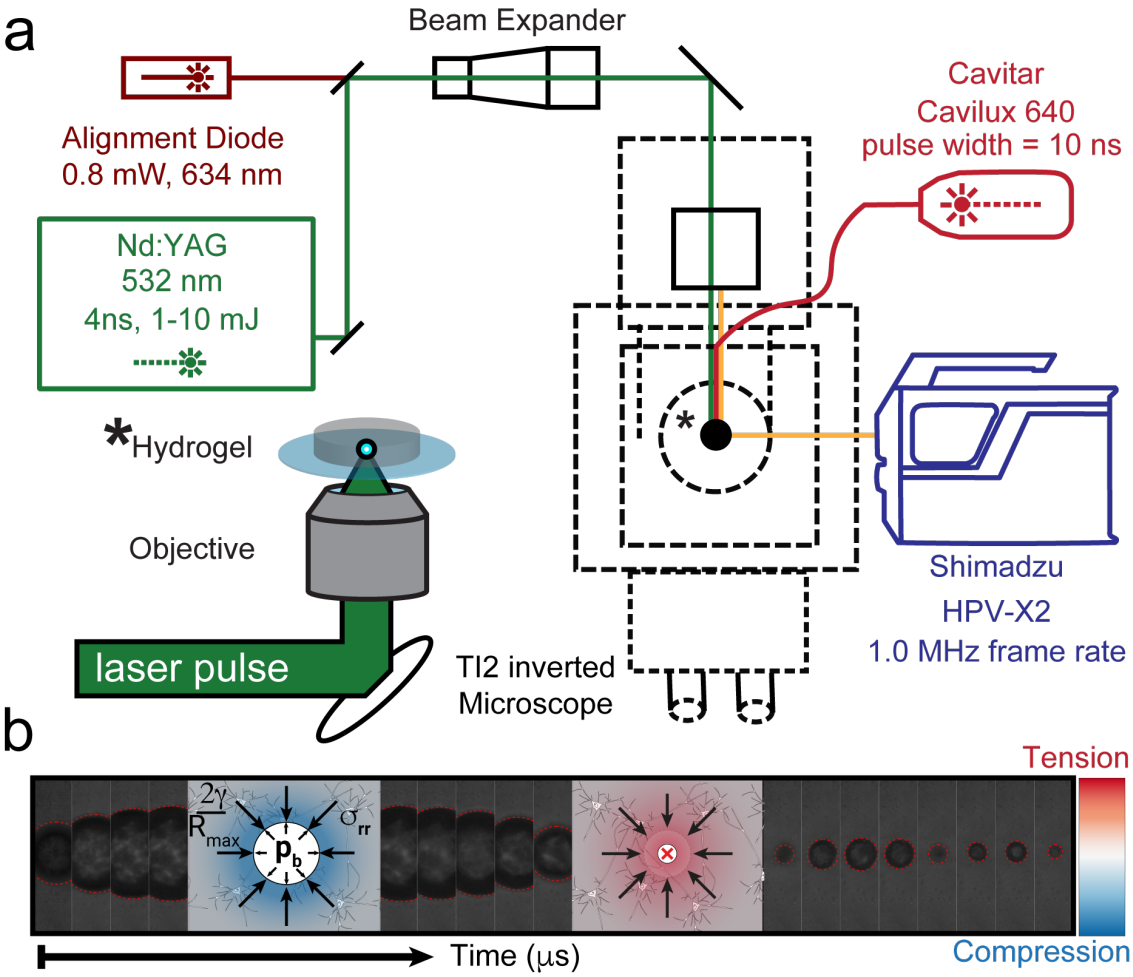

Figure 2.5: **Experimental laser-induced inertial cavitation platform and schematicized high speed videography frames** (a) Line diagram of the LIC optical platform for the controlled generation and high-speed videography of inertial microcavitation events. Single, high-energy laser pulse trains from the Nd:YAG laser are beam expanded and passed to the back aperture of the 20X imaging objective. Cavitation is generated within the sample plane (Star*) of a TI2 inverted microscope. High speed videography is captured at 1.0 MHz by a Shimadzu HPV-X2 illuminated by pulsed cavitar 640 illumination laser with a pulse width of 10 ns. (b) Example frames of high-speed videography recordings of inertial microcavitation with experimentally determined bubble radius fit (red dotted line). Inertial microcavitation events rapidly expand compressing the material around them at maximum bubble radius, the material stresses, and pressure differential across the bubble wall cause the bubble to collapse, eventually falling below the equilibrium bubble radius causing the material to be pulled in tension. Cavitation dynamics are characterized by a exponentially decaying series of oscillitory expansion-collapse cycles eventually decaying to a quasi-stable equilibrium bubble radius. Modified from Estrada et al. *JMPS* 2018 [127].

sample generating a plasma-induced cavitation event as described previously.

Simultaneously to the initiation of an the cavitation event, high-speed videography of the sample is accomplished through the same imaging objective by illuminating the sample from the top-down with an caviLUX pulsed illumination system (Cavitar, Tampere, Finland). The illumination light is passed through the dichroic mirror to a Shimadzu HPV-X2

(Shimadzu Corporation, Kyoto, Japan) high speed camera. The inertial cavitation event is recorded at 1 million frames per second which is sufficient to capture the full period of the cavitation dynamics as well as to fully resolve the quasi-stable equilibrium bubble radius. The high-speed videography and cavitation laser are time synchronized with a delay generator to obtain several frames of the sample prior to initial plasma formation. The illumination laser is temporally synchronized to each acquisition frame directly by the Shimadzu HPV-X2 camera software such that a 50 ns delay between the start of each 10 ns illumination pulse and the beginning of each 200 ns collection window exists per frame. As such an increased confidence in the radial measurement and temporal resolution of each frame (500 ns between each frame) is obtained by minimizing motion blur of the cavitation expansion and collapse internal to each frame through the use of short illumination pulses.

The Inertial Microcavitation Rheology(IMR) analytical framework, is based on a series of well-founded assumptions, discussed at length elsewhere [127]. Within the context of cavitation as a mode of mechanical deformation in this thesis, the use of IMR is limited to the temporal interpolation of the strains and strain rates within the surrounding material. In this way a requirement of adherence to the experimental limitations of the IMR analytical framework is required. The current state of IMR at the time of this thesis is predicated on several governing assumptions that affect the validity of experimental data sets, namely, the assumption of spherical symmetry, and the assumption that the material remains undrained (i.e., there is no water flux in the surrounding material) [127]. These idealizations allow us to interpret the material as nearly incompressible, which allows us compute the stretches, strains, and strain rates in the surrounding material. As such, cavitation events valid for analysis must remain measurably axisymmetric throughout the full recorded dynamics. To this end the cavitation event is generated in the center of each sample, within approximately the mid plane of the sample 600 μm above the bottom coverslip surface, to ensure a minimization of boundary effects on the cavitation dynamics. With this said, as a limitation of the experimental platform in fibrous materials in addition to requirements for other portions of the experimental setup (e.g., cellular viability and staining) the spherical symmetry assumption is relaxed at long times ($t >\sim 100\mu$s), where the quasi-stable equilibrium bubble

often splits into several small bubbles. As these bubbles are stable, they are assumed to be non-injurious as compared to the maximum bubble size. Any bubble that visibly 'jets' into the surrounding material, cannot reasonably be assumed to remain either axisymmetric, nor non fluid-flux inducing and is subsequently excluded from further analysis within the context of this work. It is important to note, however, that as the native brain is not a homogeneous material, and in-fact exists as a mixture of high density architectured cellular materials [78, 129] and as such the effects of asymmetric bubble collapse remain a valid and valuable avenue of research. However, at present the extension of quantitative mechanical analysis to these bubble systems is limited and outside of the scope of this thesis. All data-sets generated in this work have been preserved, and when sufficient advancements have been made to our understanding of the mechanics of asymmetric bubble dynamics would be valid for further analysis to this end.

2.4 Live Cell Fluorescent Imaging

As previously discussed, a major limitation of most mechanical assessments of TBI is the use of the deformed configuration for the application of mechanical tolerance thresholds. In this work, given the use of microscope-based carrier optics for the generation of mechanical injury, we preserve access to the reference configuration of each sample, without sacrificing resolution on the injurious deformations, or deformed configuration of the sample. To accomplish this, live-cell imaging of the focal region of interest within the sample is acquired immediately prior to, and immediately following the initiation of cavitation injury. Live-cell imaging is acquired through use of the classical live-cell image assay, Calcein AM (Thermofisher Scientific). Calcein AM is a cell permeable fluorophore that only fluoresces once cleaved by intracellular esterase activity present in living cells. Calcein AM is unbound within the cytoplasm of the cell and as such is a robust direct reporter for total cell morphology. The acquistion of pre- and post-cavitation images, coupled with high-speed videography of the cavitation dynamics preserves a high degree of fidelity for the full history of the sample region of interest. The specifics of image acquisition parameters will be discussed in Chapters 3 and 4 in addition to the image analysis for the calcein AM before and

after images, and the image processing algorithms for acquiring the radius versus time for each sample. Immediately following post-cavitation imaging samples are chemically fixed, and immunolabeled for protein structures of interest as described below.

2.5 Immunostaining Protocols

The immunolabeling of large hydrogel or tissue constructs is challenging. The length of time required in each individual step is dependent on a number of factors including both type of immunostaining being performed as well as the specific sample being labeled. In this work, given the optical transparency of the sample being employed, the typical use of clearing or sectioning protocols can be neglected. By neglecting these steps we preserve the spatial fidelity of each sample to their reference, and deformed configurations following cavitation-injury. This spatial-fidelity allows us to mechanically interpret, for the first time, the specific failure criteria of different cytoskeletal components of neural cellular projections in a 3D hydrogel system following high-rate mechanical deformation.

The general overview of a typical immunolabeling procedure is nuanced and must be gleaned from many literature sources and synthesized into a cohesive protocol [55, 104, 130]. Many decisions made in the literature, as will be discussed further, are left vague and subject to the individual practioners decisions. This is due to the nature of sample specificity required in each protocol, and as such many specifics must be experimentally determined by the end user. The discussion in this section will focus on the general concepts behind immunolabeling protocols and antibody selection criteria to allow the reader to make informed decisions regarding immunolabeling protocols.

A typical immunolabeling procedure for the labeling of different types of cellular proteins consists of four major steps: Fixation, Permeabilization, Blocking, and Antibody labeling. Additionally, there are two main approaches for immunofluorescent antibody labeling, direct and indirect. Direct immunolabeling, which relies on the use of primary antibodies specified against the target protein of interest, which are directly conjugated to a fluorescent reporter

molecule, and indirect immunolabeling which relies on a paired unconjugated primary antibody and a fluorescently conjugated secondary antibody. In indirect immunostaining, the primary unconjugated antibody is selected for specificity to the target molecule of interest, and the secondary fluorescently-conjugated antibody is specific for the species and isotype of the primary antibody, as discussed below. In this work, the immunolabeling protocol employs an indirect immunofluorescent labeling technique.

Typically, when selecting an immuno-panel for staining, there are several key features of your protocol to consider when selecting an antibody. To begin, a selection of primary antibody against your intended protein target is required. Primary antibodies are generally categorized by target protein, host species, isotype, clonal type, and species reactivity. The target protein, and species reactivity requirements are specified inherently by the desired fluorescent target and the species of cellular protein intending to being examined. The host species, clonal type, and isotype of an antibody are less restricted and can be selected to allow for flexibility within the protocol to stain multiple targets of interest. Most commonly, primary antibodies are raised in either a rabbit or mouse host specied against the proteins of interest in a polyclonal clonality format, this means that the antibody will recognize many different epitopes for the same target protein. Antibodies are available for purchase and can be generated in a wide array of host species, and a practitioner should not limit their selections to exclusively rabbit or mouse hosts. Primary antibodies can be further specified to an individual specific epitope of a target protein by acquiring/generating monoclonal antibodies against the desired target protein. Further, the isotype and host species can be selected to afford flexibility in staining targets for secondary antibody selection. Finally, the majority of antibodies are of the isotype IgG fraction (the most common antibody isotype), though antibodies can additionally be found that are of isotype IgM. Though challenging to accomplish successfully, the co-paneling of IgG antibodies with IgM antibodies is possible when paired with a secondary antibody specific for a specific isotype of a host species to afford flexibility when antibody selection is limited, this is however, inadvisable for inexperienced practitioners.

With respect to secondary antibody selection, the selection criteria are determined by

the desired conjugate (fluorescent reporter molecule) and selection of primary antibody. Conjugate selection is decided based on the intended fluorescent channel available for experimental imaging. It is advisable to ensure the fluorophores are well distinguished to ensure a minimization of channel cross-bleed with standard detector filter sets, though it is important to understand the optics, and available fluorescent imaging channels available to the end user. It is important to ensure your secondary antibody is selected to recognize the species and isotype of your primary antibody target. This is especially important if two antibodies of the same species are employed with differing isotypes, as previously discussed. Once antibodies are appropriately selected, the next consideration is the method of fixation and permeabilization required to appropriately label a sample protein.

The selection of an appropriate fixation method depends on both the type of protein structure that is intended to be stained in addition to the mode of imaging desired (i.e., electron microscopy versus fluroescent imaging). Most commonly immunohistochemistry protocols employ a formalin or formaldehyde-based fixation methods. Aldehyde-based fixation cross-links and stabilizes the sample to prevent autolysis, or necrosis of the sample. Cold methanol fixation is also available for specific antigens of interest, usually surface bound antigens where aldehyde or formalin fixation may overly mask binding epitopes of proteins on the surface of the cell. The fixative solution in this work consists of an aldehyde-based mixture consisting of 4% (v/v) paraformaldehyde in 1X Phosphate-buffered Saline (PBS) supplemented with 8% (w/v) sucrose to act as a stabilizing agent as the 3D neural cellular morphology consists of many fine cellular projections that require additional stabilization under fixation. Aldehyde-based fixation techniques chemically cross-links the cellular material, this cross-linking can mask binding epitopes leading to issues with antibody binding on low abundance proteins. The protocol employed in this thesis does not perform either a heat or enzymatic-based antigen retrieval step as the cytoskeletal markers investigated are typically large structures and in high abundance. Over fixation of a sample from either fixative concentration or the amount of time fixation is applied can lead to epitope masking. As such, the ideal fixation time and concentration of fixative used for a type of sample should be determined experimentally.

The selection of whether to permeabilize the sample is determined by the protein target panel desired to be immunolabeled. If the panel of target proteins consists of exclusively surface bound proteins, permeabilization of the cell membrane can potentially result in the loss of these proteins as lipids are removed by permeabilization surfactants. The cell membrane is comprised of lipids and is highly susceptible to degradation by detergent agents like Triton-X. Any protocols employing permeabilization should ensure sufficient washing is performed to ensure the sample is not overly degraded. If the intended target structure is internal to the cell and not freely floating in the cytoplasm, a permeabilization step is important to allow access to the cytoplasmic space for the non cell membrane-permeable antibodies. The protocol in this thesis employs a 0.5% (v/v) Triton-X 100 solution in 1X PBS solution. It is important to note that the amount of time the sample is exposed to the permeabilization agent must be carefully determined to avoid overly degrading the sample and destroying target protein structures.

The final step before labeling a sample with primary antibody is a blocking step intended to mitigate non-specific interactions of the antibody with the sample. Typically, blocking buffers consist of normal serum, isolated from the same species as the antibody employed, and bovine serum albumin. Blocking buffers mitigate non-specific antibody interactions with the sample by presenting similar antigens to the environment allowing for any non-specific associations to be masked by the blocking buffer rather than the antibody. The concentration and duration of blocking steps should be determined experimentally for every sample type. The protocol in this thesis employs a 10% (w/v) bovine serum albumin (BSA) in 1X PBS, with no additional serum reagents, as was experimentally determined as unnecessary. Following initial blocking steps, all wash and staining solutions in the protocol consist of a 0.5% (w/v) BSA solution in 1X PBS.

The protocol used in this thesis for the immunostaining of large 3D collagen-I and Matrigel cellular constructs in a 48-well plate format is as follows. Sample wells are fixed for 30 minutes in 4% (v/v) paraformaldehyde in 1X PBS supplemented with 8% (w/v) sucrose at room temperature ($\sim 22^{o}$C), or at 37^{o}C. All steps are subsequently performed at room temperature. Wells are then quickly washed with 1X PBS, and soaked in 1X PBS four

times for 15 minutes each. Wells are then permeabilized with a 0.5% (v/v) Triton-X 100 solution in 1X PBS for 30 minutes. Samples are subsequently rinsed, and soaked four times in 1X PBS to dilute out the Triton solution. The blocking step consists of a two hour block in 10% (w/v) BSA solution in 1X PBS followed by four wash steps in 0.5% (w/v) BSA solution. Primary antibodies are quickly centrifuged at 1000 rpm for 2-5 seconds to pellet large aggregates of antibody. Antibodies are then diluted to the desired concentration in the 0.5% BSA staining solution. The concentration of antibody employed in this study can be found in Tables 3.2, and 2.1. Samples are stained overnight ($\sim 18-20$ hours) at room temperature, on a gentle ($\sim$20 rpm) rocker table. Following incubation, antibodies are removed and replaced with washing buffer four times for 15 minutes each. From this point in the protocol the samples should be protected from light at all times, all steps should be completed away from ambient light sources with the room lights off. Secondary antibody solutions are prepared similarly to primary antibodies, relevant concentrations can be found in Tables 3.2, and 2.1. Samples are then stained with secondary antibody solution for 6 hours, or overnight at room temperature, on a gentle rocker table. The length of secondary incubation is dependent on the concentration and target protein abundance in the sample. Samples are subsequently washed in 1X PBS without BSA four times, 15 minutes each. If DAPI or phalloidin staining is required, samples are incubated with Actin ReadyProbes (Thermofisher) or NucBlue ReadyProbes (Thermofisher) kits at four drops per milliliter of solution. A final set of wash steps should be completed in 1X PBS, plates should be parafilm sealed. It is advisable to proceed to imaging as soon as possible as signal can degrade over time, however, standard probes and antibodies tend to be stable for several weeks following initial staining. Well plates should be protected from light prior to imaging.

Chapter 3

Neural cell injury pathology due to high-rate mechanical loading

Note: A version of this chapter has been published. All data and figures included are done with co-authors' consent.

Estrada JB[1], **Cramer HC III**[1], Scimone MT, Buyukozturk SB, Franck C. "Neural cell injury pathology due to high-rate mechanical loading". Brain Multiphysics, Volume 2, 2021, 100034, https://doi.org/10.1016/j.brain.2021.100034.

[1]Authors contributed equally.

3.1 Introduction

Mechanical forces play a critical role in maintaining the form and function of many biological systems from single cells to entire organisms [131, 132]. From the perspective of a cell, maintenance of physical homeostasis involves a constant balancing act between internal and external forces and deformations. Critical cellular processes such as tissue morphogenesis [133], protein expression [134], and cell differentiation [135], are often a result of slight and well-coordinated changes in a cell's physical homeostasis. In cases of significant disruption in homeostasis, such as in physical trauma, cells can produce a spectrum of insult-dependent pathologies, broadly classifiable as either immediate mechanical breaking

of cellular microstructural components (primary injury), or the activation of apoptotic or necrotic pathways (secondary injury) [4, 56].

Abnormal loading conditions can occur from unintentional causes (e.g., during Traumatic Brain Injuries or TBI), or through intentionally administered therapeutic treatments including many modern surgical or disease-mitigating procedures [136]. Particularly, the last decade has seen rapid growth in the use of focused energy techniques including diagnostic [41–43] and therapeutic ultrasound [44–47] and laser-based ablation methods [48, 49] for a variety of patient treatment procedures, from removing tumors to correcting eyesight. The physical mechanism of tissue removal in ultrasound-based procedures such as histotripsy is the generation of cavitation bubbles that impart extremely high-rate and large deformations onto the surrounding cells and tissues which lead to tissue fragmentation, lysis and cell death. Laser-based ablation procedures can also produce significant microcavitation while heating the tissue [48, 49, 51]. Despite these methods' growing popularity and the well-defined qualitative understanding of their use, little is quantitatively known about the relationship between bubble size, bubble pressure, and resulting tissue stresses and strains on cellular and tissue damage and injury [50].

Recently, blast-related traumatic brain injuries in the armed forces have pointed toward the possibility of a brain injury signature distinctively different from those associated with the pathologies of commonly diagnosed blunt-force mild to severe TBIs [18]. The chief distinction between these types of TBI could be the significantly higher deformation or strain rates experienced under such conditions, similar to those occurring during exposure to either electromagnetic or sonic-based directed energy devices [39]. To this end, a variety of efforts aimed toward mitigating or preventing TBI have turned to advanced computational models of the head and neck to better understand the role of high-rate deformations, forces, stresses and strains in the overall associated injury risk potential [137, 138]. While these models have progressed in their complexity and predictive power, their experimental validation—specifically resolution of critical cellular and subcellular injury or damage thresholds—has remained elusive.

Considering that mechanical loading on the tissue and cells can be highly disruptive and

destructive, it is paramount to resolve critical thresholds in force and deformation along with cellular pathologies under such conditions. Understanding the extent of disruption and injury is especially important in neural tissues to prevent any loss of function within the central nervous system.

Careful resolution and quantification of the mechanical forces and deformations, or strains, that lead to injurious cellular disruptions and possible cell death have remained a formidable challenge in practice. This is in part due to the fast, high-rate character of the mechanical deformations imparted onto the cells, which require camera frame rates on the order of hundreds of thousands to millions of frames per second to resolve. Furthermore, the generation of high-strain rate loading above 100 1/s is a significant technological challenge for any electromechanical device, and gas and gravity driven impact devices often struggle with achieving well-characterized, repeatable and appropriate loading conditions for such compliant viscoelastic materials as cellular brain tissue. Furthermore, in order to remove loading and boundary artifacts that could complicate the post analysis of cellular injury, sample preparation and mounting cannot be injurious to the cells and tissues. This poses a major challenge to most traditional mechanical loading stages or bioreactors. Finally, and especially for neural tissues, scaffolds or tissue structures promoting three-dimensional (3D) cellular architectures are crucial for replicating physiologically relevant mimics of the *in vivo* tissue microenvironment.

To address these key challenges and to provide a robust method for quantitatively resolving cellular injury thresholds and pathologies with high spatial resolution, we combine our recently developed inertial microcavitation rheology (IMR) technique [139] with an established 3D *in vitro* neural cell tissue model [56]. Through 3D-positioning of a spatially-controlled inertial cavitation bubble within the 3D neural tissue model, high-rate mechanical deformations (material strain rates on the order of $10^3 - 10^8$ 1/s), are achieved without the need to handle, mount or condition the tissue prior to loading. This is a significant advancement over current state of the art cellular and tissue TBI injury devices, which tend to produce loading rates up to 100 1/s or less [4, 140–142]. By integrating this technique into the optical path of a multiphoton microscope, high-resolution, 3D volumetric image

stacks can be acquired before and after an induced high-rate loading event. To construct a strain- and strain-rate-dependent pathology atlas, common immunocytochemical markers are employed and correlated to the applied high-rate deformations. Additionally, by employing our previously developed quantitative theoretical framework built into IMR, we can estimate cellular strains and provide stress threshold estimates for cellular projections containing each subcellular structural component represented in the injury pathology. Taken together, this study provides a significant quantitative advancement in our understanding of this biologically and clinically important injury pathology, and provides actual, measured cell-level details on the critical strain and stress thresholds associated with structural degeneration across key cellular constituents including microtubules, filamentous actin, and microtubule-associated protein-2 (MAP2).

3.2 Methods

3.2.1 Isolation of primary neural cells

All procedures were performed in full accordance with the Institutional Animal Care and Use Committee's of Brown University and the University of Wisconsin, Madison. Unless otherwise stated, reagents were acquired from Thermo Fisher (Waltham, MA). Primary neural cells were isolated from postnatal day 0-1 Sprague-Dawley rats (Charles River, Wilmington, MA). Pups were anesthetized with hypothermic treatment and euthanized through cervical dislocation. The cerebral hemispheres were removed and placed in a cold solution of Hibernate A (HA; Brain Bits LLC, Springfield, IL) + 2% B-27 serum-free supplement (50×) + 0.25% GlutaMAX (100×), ventral side down. A cut was made around the lateral side of the brain, just above the entorhinal and perirhinal cortices, followed by separation at the corpus callosum. The excess tissue was removed from the cerebral cortex and the cortices were minced (∼0.5 mm) and digested in a solution of Hibernate A (HA) –$CaCl_2$ (Brain Bits LLC) + Papain (2 mg/mL; Worthington, Biochemical Corporation, Lakewood, NJ) for 30 minutes at 37°C with gentle agitation every 5 minutes. An equal volume of pre-warmed HA/B-27 was added to the HA-$CaCl_2$/papain solution and centrifuged at 150g for 5 minutes. After

removal of the supernatant, the dissociated tissue was re-suspended by gentle mechanical trituration in cortical complete media (Neurobasal-A medium + 1% Penicillin/Streptomycin + 0.25% GlutaMAX 100×), allowed to settle for 1-2 minutes, and passed through a sterile cell strainer (40 μm mesh size) to filter large tissue debris. The suspension was again centrifuged at 150g for 5 minutes, the supernatant was removed, replaced with 3 mL cortical complete media, and cells were re-suspended by gentle mechanical trituration and counted with a hemocytometer (Hausser Scientific, Horsham, PA). Cell solution was diluted with cortical complete media to 10^6 cells/mL prior to preparation of 3D collagen gels to yield a final seeding density of 3,750 cells/mm^3 [4, 78, 143]. Additional information and specifics of the cortical isolation and a more detailed protocol can be found in Chapter 2 section 2.2.2 and the associated publication, Scimone et al 2018 [56].

3.2.2 Preparation of 3D collagen hydrogels

Type I Collagen (rat tail; Dow Corning, Tewksbury, MA) hydrogels were made at a concentration of 2.2 mg/mL according to the manufacturer's standard protocol. 10× Phosphate-buffered Saline (PBS) was mixed with type I collagen stock solution (3.3−3.7 mg/mL) in 0.02 M acetic acid, triturated, and kept on ice. Neuron-cell media suspension was then added to the collagen mixture to get a collagen concentration of 2.2 mg/mL and neuron density of 3,750 cells/mm^3, and brought to a target pH of 8.4 through the addition of 1 M NaOH (Sigma-Aldrich, St. Louis, MO). Collagen gel composition is shown in Table 3.1. 50 μL volumes of cell-collagen gel solution were seeded directly into 48-well #1.5 glass-bottomed plates (MatTek, Ashland, MA). Dimensions of the samples were approximately 6 mm in diameter and 1.2 mm in height.

Table 3.1: **Concentrations for 3D type I Collagen hydrogels.**

Component	**10× PBS**	**1 M NaOH**	**Stock Collagen-I**	**Cell Suspension**
Volume %	10	1.4	56.2	32.4

Gels were polymerized in a humidified incubator at 37°C in 5% CO_2 for approximately 20

minutes after which 300 μL of cortical complete media is added to each well after polymerization. Each plate of samples was incubated at 37°C, 5% CO_2 for 7 days *in vitro*, after which neurons showed a high degree of network connectivity (Figure 3.1a).

3.2.3 Live-cell fluorescence

Cell morphology was assessed before and immediately following microcavitation via cell-permeant Calcein Acetoxymethyl (AM). Cell cultures were incubated with 200 μL of pre-warmed HA+2% B-27 buffer with Calcein AM (20 μM) for 45 minutes to 1 h to allow for sufficient penetration into the gel, after which media was replaced with naïve pre-warmed HA+B-27 buffer. Samples not exhibiting healthy, fully-connected morphology were discarded from further data processing. Control cultures were incubated with 200 μL of pre-warmed HA+2% B-27 buffer containing both Calcein AM (20 μM) for 1 hr, after which media was replaced with naïve pre-warmed HA+B-27 buffer.

3.2.4 Fixation and Cytoskeletal Labeling

Neural cell cultures were fixed post-live-cell fluorescent imaging using a solution of 4% v/v paraformaldehyde (Electron Microscopy Sciences, Hatfield, PA) + 8% w/v sucrose in 1× PBS for 30 minutes. Samples were subsequently washed four times with 1× PBS and stored at 4°C prior to additional labelling procedures. Samples were permeabilized in 0.5% (v/v) Triton ×100 for 30 minutes, washed three times with 1× Phosphate Buffered Saline (PBS). Non-specific staining was limited through a blocking step using 10% (w/v) Bovine Serum Albumin (BSA) (Jackson ImmunoResearch, PA, USA) for 2 hours at room temperature (measured at 22-23°), and all subsequent wash and stain steps were completed using 0.5% (w/v) BSA at room temperature. After blocking, samples were washed twice and stained overnight at room temperature for the primary antibody marker of interest, see Table 2. Samples were washed four times, and submerged in secondary antibody for six hours. Alternatively, if not antibody-stained, samples were washed four times and stained with Phalloidin stain ActinRed 555 ReadyProbes for 2 hours at 4 drops/mL in 0.5% BSA and washed four times with 1× PBS.

Table 3.2: **Immunolabeling probes for proteins of interest**

Antibody Target	Species	Manufacturer	Catalog No.	Concentration
Primary Antibodies				
β3-tubulin	Mouse (IgG)	ThermoFisher Sci.	MA1-19187	1:200
MAP2	Rabbit (IgG)	ThermoFisher Sci.	PA5-17646	1:200
Secondary Antibodies				
Anti-Mouse AF555	Goat	ThermoFisher Sci.	A32727	1:100
Anti-Rabbit AF555	Goat	ThermoFisher Sci.	A32732	1:100
Phalloidin Probes				
Filamentous actin		ThermoFisher Sci.	R37112	4 drops/mL

3.2.5 Microscopy and imaging

For all live-cell experiments and controls, three-dimensional image stacks of cells immediately before and immediately following laser-induced cavitation were acquired using a Nikon A-1 laser scanning confocal or multiphoton system, mounted on a Ti-Eclipse inverted optical microscope controlled by NIS-elements software (Nikon, Tokyo, Japan). To maintain physiological conditions, a custom-made environmental chamber was built around the microscope and thermally-controlled at 37°C with a closed-loop Air-Therm heater (World Precision Instruments, Sarasota, FL). Samples in 48-well glass-bottomed plates were secured using a well plate holder (Ti-SH-W; Nikon), which was allowed to thermally equilibrate before imaging to avoid thermal drift in imaging locations. All cavitation events were performed 600 μm above the top of the glass coverslip, or approximately at the mid-plane of the gels.

3.2.6 Laser-induced microcavitation

The generation of laser-induced cavitation and a full exploration of the governing parameters and physics have been described elsewhere [127]. Briefly, experimental inertial cavitation was generated via single pulses of a 3-5 ns, 1-10 mJ frequency-doubled 532 nm Q-switched Nd:YAG laser (Continuum, San Jose, CA) through a Plan Fluor 20×/0.5 NA objective (Nikon Instruments, Japan). Single laser pulse energy is straightforwardly modulated between 1 and 10 mJ by rotation of a polarized waveplate in the laser head. Laser energy is minimized to the experimentally determined threshold required for the generation of a

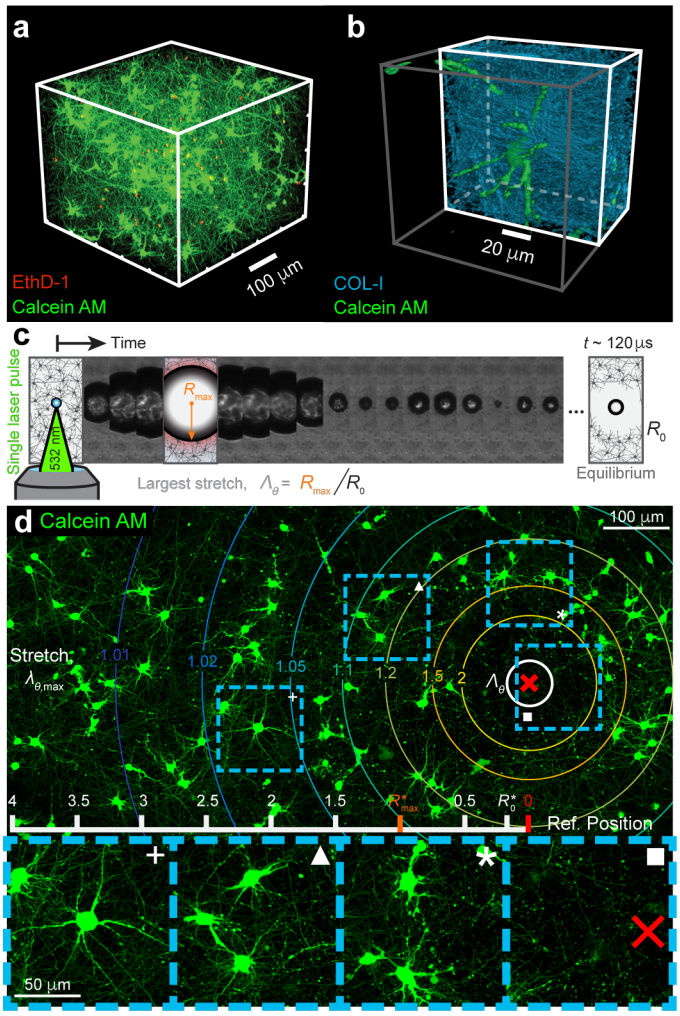

Figure 3.1: **Experimental injury platform and projected, 3D micrographs of high loading rate cellular pathology.** (a) 3D type I collagen gels are fabricated *in vitro*, containing primary neural cells (green) which grow and form healthy, connected networks. (b) Cells (green) are well-encapsulated by type I collagen (sky blue). (c) A single, 4 ns laser pulse focused through a microscope objective induces microcavitation in the gel. The cavitation microbubble rapidly grows in the sample, reaching a maximum radius $R_{\max}$ (orange tick mark), and subsequently collapses and oscillates, finally reaching a quasi-equilibrium state R_0. (d) Cells in the vicinity of the bubble are rapidly deformed by radially-decaying circumferential (hoop) stretch levels, $\lambda_{\theta,\max}$, indicated by the color-coded radial rings. Each radial ring represents the maximum tensile (hoop) stretch, $\lambda_\theta = \lambda_{\theta,\max}$ experienced by each cell. While cells that experience stretches less than $\lambda_{\theta,\max} < 1.05$ remain morphologically intact (plus), cells closer to the bubble center exhibit varying degrees of degenerate projections $1.05 < \lambda_{\theta,\max} < 1.2$ (triangle) and somatic disruption $1.2 < \lambda_{\theta,\max} < 2$ (star, inset image rotated). Very near to the bubble epicenter (red x), cell somas and projections are entirely fragmented at $\lambda_{\theta,\max} > 2$, (square, inset image rotated). The overall spatial extent of injury is dependent on the maximum bubble size ($R_{\max}$), and is generally contained within 2–2.5$\times R_{\max}$ as indicated by the overlaid ruler (units are in multiples of $R_{\max}$).

cavitation event. The beam was then redirected into the back aperture of the objective by a 532 nm notch dichroic reflector (Semrock, Rochester, NY), and expanded to fill the back aperture of the imaging objective using a variable beam expander (Thorlabs, Newton, NJ). Upon passing through the objective, pulses converged at the image plane as validated by a continuous exposure alignment of a 635 nm laser diode (LDM635; Thorlabs, Newton, NJ) and were imaged using bright-field microscopy at either 270,000 fps on a Phantom V2511 (Vision Research, Inc., NJ, USA) or at 1,000,000 fps on a Shimadzu HPV-X2 (Shimadzu Corporation, Kyoto, Japan). The condenser aperture was reduced as much as possible without overly reducing image intensity to minimize effects of non-parallel light interacting with the bubble. As each 3D collagen gel had dimensions of 3 mm radius and 1.2 mm height,

and to reduce potential biological effects of cellular death factors and mechanical effects of introduced boundaries, only one cavitation event was generated in each non-control sample at the approximate middle z-plane of 600 μm.

3.2.7 Cavitation Bubble Determination

Input : High-speed bubble `.tif` stacks of bubble kinematic images I_t
Output: Bubble radii $R(t)$

Convert all images to grayscale if needed, `rgb2gray`;
for *all clear images after reference,* $t > 0$ **do**
  if *there exists a well-defined pre-cav image* I_0 **then**
    Remove baseline reference ($D = I_t - I_0$);
    Normalize and threshold to make binary mask $BW =$ `ceil`($\hat{D}-$thresh);
    Get `regionprops`;
    if *bubble is split into two parts by the image walls* **then**
      Combine two largest connected regions into one;
    end
  else
    First-pass segmentation to find mean frame-wise background intensity $\bar{I}_t$;
    Binarize image by $BW = I_t < \bar{I}_t - 2\sigma$(background pixels);
    Get `regionprops`;
    Smooth regions with 2-px `erode-dilate` to reduce overfitting
  end
  Determine connected mask regions, `bwconncomp`;
  Build convex hull of bubble from mask objects;
  Remove points on image edges;
  Fit circle using Taubin method, [R_t, centroid] = `CircleFitByTaubin`(convex hull points)
end

Algorithm 1: Calculating $R_{\max}$ and R_0 from high-speed bubble images

The general processing procedure for acquiring the maximum bubble radius and equilibrium radius from high speed video is outlined in Algorithm 1. Each time-series of images consisted of either 101 frames of 512×128 px from a Phantom v2511 high speed camera, or 256 frames of 400×250 from a Shimadzu HPV-X2 high speed camera. Imaging frame rates were set to 270k fps (3.7 μs/frame) for the Phantom v2511 and 1M fps (1 μs/frame) for the Shimadzu HPV-X2 with a calibration image of an etched calibration grid taken for each to set the μm/pixel ratio for each time-series (v2511, 1.38μm/pixel; HPV-X2, 1.62μm/pixel). For cases where there was a well-defined reference image, the first image in each time-series

Input : Laser scanning confocal stacks of 1024×1024×11 (1.24×1.24×20 μm) images from before (I_0^z) and immediately after (I_t^z) cavitation injury
Output: Mechanical primary injury radius R_{PI} immediately post-cavitation
for *z = 1 to height of stack* **do**
  Gamma-shift confocal images, $I^z = (I^z)^{0.7}$;
  Determine background pixels BW_n from 2D Hessian-based Gaussian filter $\mathcal{H}_2$, $BW_n = \ \sim (\mathcal{H}_2(I^z))$;
  Determine image noise floor $\delta I^z = \mathrm{median}(I^z(BW_n)) + 2\ \mathrm{mad}(I^z(BW_n))$;
  Determine rigid drift u^z as median of $\boldsymbol{u}^z(x,y) = \texttt{qDIC}(I_0^z,\ I_t^z)$;
  Take 2D median filters $\mathcal{M}_2$ for differential images $D^z = \mathcal{M}_2\left(I_0^z\right) - \mathcal{M}_2\left(I_t^z - u^z\right)$;
end
$D = \max(D^z, z)$;
$\delta I_t = \mathrm{median}(\delta I_t^z, z)$;
Determine injury radius centroid $\{\bar{x}, \bar{y}\} = \left\{\sum_x D, \sum_y D\right\}$;
Make binary mask of damage using threshold $BW_D = D > \delta I_t$;
Define radial transform matrix $\boldsymbol{r}(x,y) = \sqrt{(x-\bar{x}).^2 + (y-\bar{y}).^2}$;
`// Create density field` ρ `by discretizing into` k `bands of` $\Delta\boldsymbol{r}$ `= 1 px`
Define density noise floor $\delta\rho = \mathrm{mean}(\rho) + 5\sigma_\rho$;
for *ring index k = 1 to edge of image* **do**
  $\rho(\boldsymbol{r} \in k) = \sum_{\boldsymbol{r}\in k} BW_0(\boldsymbol{r}) / \sum_{\boldsymbol{r}\in k} \texttt{ones}(\boldsymbol{r})$;
end
Determine cumulative linear density function $P = \int_0^r \rho dr / \int_0^r dr$;
$R_{\mathrm{PI}} = r(P = 97.5\%)$.

Algorithm 2: Calculating R_{PI} from laser scanning confocal image stacks.

was designated as a reference image I_0 of the gel before arrival of the laser pulse. For subsequent images of the bubble I_t, differential images $D = I_t - I_0$ were constructed, normalized, and thresholded to create binary masks. In cases without a reference image, a first-pass segmentation defined a background intensity threshold to create binary masks. The built-in function `bwconncomp` (Image Processing Toolbox, Matlab) was then used to segment the bubble area. A convex hull was constructed around the bubble object excluding points on the image boundaries. Finally, points along the convex hull were then fit using a generalized eigenvector fitting method developed by Taubin [144] for the specific case of a circle. Bubble images were overlaid with the circle fit outline and manually inspected to ensure accurate fitting.

Input : Immunofluorescence end-point image stack (I^z_{t+}) of $1024 \times 1024 \times 113$ ($0.5 \times 0.5 \times 1.35$ μm), post-cavitation live-image stack (I^z_t) of $1024 \times 1024 \times 11$ ($1.24 \times 1.24 \times 10$ μm), and the cavitation center $\{\bar{x}, \bar{y}\}$ in (I^z_t)
Output: Projection damage locations, ($\boldsymbol{\chi}^{(i)}$)

Find maximum projections $I_{t+} = \max_z I^z_{t+}$ and $I_t = \max_z I^z_t$;
Upsample I_t to match grid of I_{t+};
Manually register landmark coordinates (x_ℓ, y_ℓ) for I_t and I_{t+};
for *z = 1 to height of stack* **do**
    Find the corresponding z-slice of selected points,
    $z = max(mean(i \pm 10, j \pm 10), k)$;
end
Cross-correlate $I^z_t(x_t, y_t, z_t)$, and $I^z_\tau(x_\tau, y_\tau, z_\tau)$;
Compute cavitation centroid (x_τ, y_τ, z_τ) in (I^z_τ);
Find maximum projection of all slices $\pm 50 \mu m$ of z_τ, $I^{\pm 50}_{t+}$;
for *Each quadrant of* $I^{\pm 50}_{t+}$ **do**
    Manually select lateral locations of damaged projections (x_ρ, y_ρ)
end
Compute vertical heights to each point, z_ρ;
Discard non-unique fits, and any point within $\pm 5 \mu$m from top or bottom;

Algorithm 3: Calculating radial positions of damaged neural cellular projections

3.2.8 3D Image acquisition

Prior to laser-induced microcavitation, reference image stacks of 1024×1024×11 px (1.24×1.24 μm spacing in x-y, 10 μm spacing in z) images of Calcein AM-stained neural cells were acquired with a 10×/0.3 NA Plan Fluor objective (Nikon) centered at 600 μm above the top surface of the bottom coverslip. Rather than create a full 3D reconstruction, total volume size and laser settings were chosen to ensure minimal effects from phototoxicity, resulting in a pseudo-3D confocal volume stack. Following initial imaging, cavitation was generated as described above, consistent with prior work [127, 145]. Samples were imaged and cavitated as described above in sets of 6-8 to reduce the time delay between cavitation and post-imaging. After completing a set of samples, the dichroic was removed and the 10×/0.3 NA Plan Fluor objective was repositioned to acquire a post-cavitation stack of images, again with dimensions 1024×1024×11 px (1.24×1.24 μm in x-y, 10 μm spacing in z). Laser scanning multiphoton imaging of immunolabelled subcellular structures was performed using a

25×/1.1 NA Apochromat water immersion objective (Nikon Instruments, Japan). Multiphoton image stacks of 1024×1024×113 px (0.5×0.5×1.35 μm spacing) were taken post-fixation for structural regions of interest.

3.2.9 3D Image processing

The general processing procedure for determining the primary injury radius from the reference and post-injury confocal image stacks of cells stained with Calcein AM is outlined in Algorithm 2.

Each z-image in an image stack was first gamma-shifted by a factor of 0.7, and subsequently processed by a Hessian-based Gaussian filter [146] kernel with σ ranging from 1 to 3 to determine a slice-wise noise floor. Due in part to drift, switching imaging optics, and to the cavitation event itself, some rigid translation occurred between each image before and after cavitation; registering image drift is a common part of image differencing techniques to get accurate results [147]. For this study, we corrected for rigid motion drift by running a quality-factor based digital image correlation method [148] and shifting the second image by the determined median image displacement. Corresponding images in the reference configuration were then compared to rigid-motion-corrected images in the damaged configuration at times immediately after cavitation. Differences between the image pairs, called *differential* images, were then median-filtered, summed in the stack-direction, and thresholded automatically by the Hessian-determined noise floor. A binary mask was constructed as the values in the differential image stack sum, D, above the threshold. This binary mask represents all pixels that significantly drop in intensity between the undamaged and damaged images, and physically represents local ceasing of intracellular esterase activity. To assess disruption of esterase activity radially, the epicenter of the cavitation injury $(\bar{x}, \bar{y})$ is calculated from the 2D median of the cumulative sum of the rows and columns of $\boldsymbol{D}$.

A distance transform matrix $\boldsymbol{r}(x, y)$ is constructed as the distance away from the bubble epicenter location for each pixel (x, y) in D. From the center of the bubble at $r = 0$, it is convenient to take the relative density difference as a radial measure of damage, that is, the high density of fluorescent intensity loss concentrated in the bubble region is considered

the damaged zone. Intensity loss density ρ was determined by defining $\Delta \boldsymbol{r}$-width concentric rings, summing the lost pixels (where the mask is 1), and normalizing by the number of pixels in each ring. The density noise floor is user-adjustable, but was conservatively taken as 5 standard deviations above the median far-field density in this study. The radius of mechanical disruption or primary injury of the plasma membrane immediately after cavitation, R_{PI}, was then defined via the linear integral of the radial density; specifically, where 97.5% of the cumulative fluorescent intensity loss (i.e. two standard deviations above the median) occurs.

The general immunofluorescence image processing procedure for determining the locations of damaged projections is outlined in Algorithm 3. Immunofluorescence end-point image stacks (I^z_{t+}) of $1024 \times 1024 \times 113$ ($0.5 \times 0.5 \times 1.35$ μm) are used to manually determine the location in three dimensional space of damaged projections for each immunofluorescence marker. Here, a damaged projection is defined as any continuous projection originating from a cell soma that terminates abrubtly and without intuitive cause to the observer with experience examining the healthy morphological state of 3D neural cell cultures. A calcein AM post-cavitation live-image stack (I^z_t) of $1024 \times 1024 \times 11$ ($1.24 \times 1.24 \times 10$ μm) is upsampled to match the grid size of I^z_{t+} and manually registered with a combination of manual landmark matching and image cross-correlation. An input cavitation epicenter $(\bar{x}, \bar{y})$—assumed to fall in the mid-plane of I^z_t $(\bar{z})$—is then converted from the known coordinates in I^z_t to the corresponding coordinates in I^z_{t+}. Maximum projections are computed from all slices of I^z_{t+} determined to fall within $\pm 50\mu$m of $\bar{z}$ and a quadrant-wise manual point selection is completed to localize the lateral location of damaged projections. All lateral$(x - y)$ positions manually identified are registered in along the z-axis by computing the maximum value of the median intensity within a window constructed about each x, y point along z. Any point determined to fall within the top or bottom 5μm of the image stack are neglected to avoid image clipping; additionally, any point without a unique maximum value is excluded from further processing.

3.3 Results

To resolve the pathology and critical injury thresholds of high-rate deformations on neural cell populations, a 3D *in vitro* neural tissue model [56] was integrated with our recently developed, laser-based microcavitation technique as a means to mechanically load the cellular constructs. The *in vitro* model consists of neural cells dissociated from the cortices of post-natal p0-p1 Sprague Dawley rat pups and encapsulated in a collagen-I hydrogel in a glass-bottomed 48 well plate. The neural cell population undergoes neurogenesis over the course of 7 days *in vitro* during which the cells form healthy network connections consistent with previous work [13, 56] as seen in Figure 3.1a. Cells were determined to be well-encapsulated by collagen fibers using reflectance confocal and auto-fluorescence microscopy (Figure 3.1b). To mechanically deform the cells at high loading rate, a single microcavitation bubble was generated inside the neural tissue model via a spot-focused, ∼4 nanosecond pulsed laser aligned into the back port of an inverted microscope. Briefly, the deposited laser energy nucleates a microcavitation bubble, which grows and rapidly stretches the surrounding neural tissue as it expands to a maximum radius, $R_{\max}$ (Figure 3.1c). The general bubble dynamics feature several, exponentially decaying oscillatory expansion-collapse cycles [127] until the bubble reaches its final stress-free, quasi-static equilibrium bubble radius, R_0, over the course of $\sim 120\mu$s. High-speed video of bubble dynamics from each experiment was recorded by one of two methods: at 270,000 frames per second using a Phantom v2511 (Vision Research Inc, Wayne, NJ) high-speed camera, or at 1 million frames per second with a Shimadzu HPV-X2 ultra-high speed camera (Shimadzu, Kyoto, Japan), both using bright field microscopy. An example set of high-speed images at cropped spatial and temporal resolution from the latter is shown in Figure 3.1c. Bubble radii were determined from these images using a custom image processing algorithm modified from our prior work [127].

To quantify the physical deformations that the neural cells experience during high-rate cavitation loading we begin by describing the change in position, or displacement, of each material point (cells and collagen) using a standard continuum mechanics representation [127]. We denote the current radial position of the bubble wall in time as $R(t)$, with an

associated "reference" radius R_0 of the bubble in the stress-free, equilibrium configuration at long times. The maximum radius, $R_{\max}$ is then defined as, $R(t=0) = R_{\max}$. Radial positions in the material are then functions of both the bubble radius and time, and are denoted as $r(r_0, t)$ and r_0 in the current and reference configurations, respectively. To relate the physical stretch experienced by the cells to the measured bubble radii $R(t)$ during cavitation, we first define the material deformation gradient tensor $\mathbf{F}$, as

$$\mathbf{F} = \begin{bmatrix} \frac{\partial r}{\partial r_0} & 0 & 0 \\ 0 & \frac{r}{r_0} & 0 \\ 0 & 0 & \frac{r}{r_0} \end{bmatrix}. \tag{3.1}$$

Considering the high-rate of loading, the material can be treated to be near-incompressible [149, 150], i.e., $\det(\mathbf{F}) = 1$, yielding the following relationship:

$$\frac{\partial r}{\partial r_0} = \left(\frac{r_0}{r}\right)^2. \tag{3.2}$$

Equation 3.2 can then be solved in terms of the current radial position $r(r_0, t)$ as

$$r(r_0, t) = \left(r_0^3 + R(t)^3 - R_0^3\right)^{1/3}, \tag{3.3}$$

establishing a geometric relationship between any spatial position within the gel, r, and the current and equilibrium bubble radii, R and R_0, respectively. Finally, we define the circumferential, or hoop, material stretch, λ_θ, during mechanical loading as

$$\lambda_\theta(r_0, t) = \frac{r(r_0, t)}{r_0}, \tag{3.4}$$

with the average maximum tissue stretch occurring at the bubble wall over all experiments during the time of largest bubble expansion defined as Λ_θ,

$$\Lambda_\theta = \lambda_\theta(R_0, t|_{R_{\max}}) = \frac{R_{\max}}{R_0}. \tag{3.5}$$

While a similar relationship can be established for the radial stretches, we focus on the predominantly tensile hoop (or circumferential) stretch, which prior work established to be one of the most injurious modes of deformation to cells [4]. Figure 3.1d provides representative projected micrographs of neural cells labeled with the live cell indicator Calcein AM that underwent a high-rate loading event, with the actual, measured hoop stretch magnitudes displayed by a distribution of radial rings. The maximum tensile hoop stretch occurs at the time when the bubble is largest, i.e. when $R(t) = R_{\max}$. We correspondingly write a quantity $\lambda_{\theta,\max}$ as the hoop stretch experienced by cells at different radial positions at the time of maximum bubble expansion,

$$\lambda_{\theta,\max}(r_0) = \lambda_\theta \left(r_0, t|_{R_{\max}}\right), \tag{3.6}$$

Thus, all hoop stretch levels $\lambda_{\theta,\max}$ shown in Figure 3.1 correspond to the maximum tensile stretches experienced by the cells as a function of radial distance from the bubble epicenter. Consistent with mechanics-based models of inhomogeneous deformations induced by an expanding and collapsing bubble, the deformation field decays rapidly with distance ($\sim 1/\mathrm{r}^3$) away from the bubble wall.

As can be seen from the individual insets in Figure 3.1d, there is a clear transition in cell morphology from a healthy network at stretches below $\lambda_{\theta,\max} \approx 1.05$, to a pathology marked by significant morphological degeneration at stretches of $\lambda_{\theta,\max} > 1.2$ to a complete loss in Calcein AM signal at stretches of 2 and above. As fluorescence produced by Calcein AM indicates intact function of intracellular esterases of living cells, complete loss in Calcein AM signal indicates probable cell death. Spatial distances measured from the bubble center directly correlate with the amount of physical stretch experienced by the cells (see Eqs. 3.3, 3.4). Therefore, we use a simple image subtraction procedure of the Calcein AM signal in images before and after mechanical loading (i.e., cavitation). Notably, both of these images are taken of the reference configuration, but the difference between them allows us to quantitatively extract the radial boundary beyond which complete Calcein AM signal was present and below which it was lost. We denote this significant position in the tissue as $r_0 = R_{\mathrm{PI}}$, which we call the primary injury radius.

Figure 3.2a illustrates the general analysis procedure for identifying critical injury thresholds associated with various pathological features shown in Figs. 3.1d and 3.3. Prior to cavitation-induced loading of each sample a 3D volumetric image is obtained as the healthy base, or reference, state. Next, we employ a modified form of our previously developed image fitting routines [127] to accurately extract the time-varying bubble radii, $R(t)$, from each of the high-speed image frames recorded during the cavitation event. Finally, a high-resolution 3D post-scan of the same volumetric image stack is obtained and cellular morphologies (labeled via Calcein AM or various immunocytochemical markers) different from their respective base state are spatially marked.

Figure 3.2b provides a representative overlay of the best fit of the maximum bubble radius, $R_{\max}$, and the final bubble equilibrium radius, R_0, onto the high-speed brightfield microscopy image. Across all performed experiments the values for $R_{\max}$ and R_0 ranged from $60 - 338$ μm ($N = 238$) and $10 - 55$ μm ($N = 219$), respectively, with the ratio between them defining the maximum material stretch. As can been seen from Figure 3.2d, the scaling between $R_{\max}$ and R_0 is highly linear (bisquare $R^2 = 0.971$) across a large distribution of maximum bubble radii with the median maximum bubble stretch ratio at the wall given by $\Lambda_\theta = R_{\max}/R_0 = 7.40$ (Figure 3.2d, black).

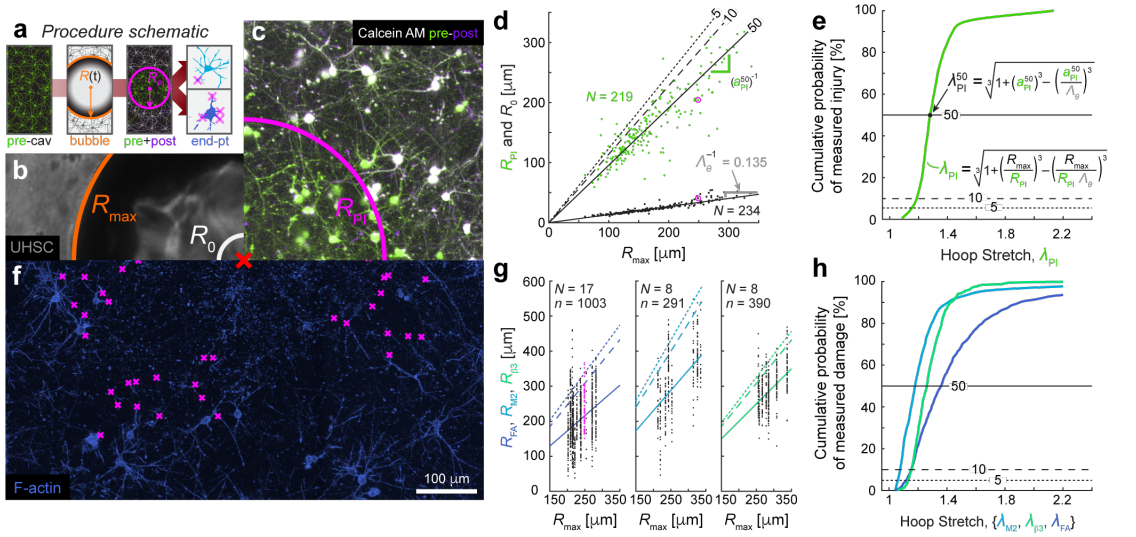

Figure 3.2: **Procedure and image processing-based quantification of neural injury and critical stretch-based injury thresholds.** (a) The mechanical history of a sample is defined by a chronological sequence of image sets: a 3D pre-cavitation reference set of live-stained cells, (b) a 2D ultra-high-speed video of the high-rate loading cavitation bubble dynamics, including maximum size $R_{\max}$ (orange) and quasi-equilibrium size R_0 (white), and (c) a 3D post-cavitation image stack of live-stained neural cells. Maximum projections of the pre- (green) and post-cavitation (purple) image stacks are overlaid as an anaglyph image to illustrate the region of complete cellular damage (white color indicates the time-colocalization of cells before and after injury). A customized image subtraction algorithm computes a radius of primary injury (R_{PI}, magenta) for each injured 3D volume. (d) Both the primary injury (PI, green, $N = 219$ experiments) and bubble equilibrium (black, $N = 234$) radii for each experiment (data points from (c) circled in magenta) scale linearly with maximum bubble radius, suggesting a constant and invariant critical strain value for primary mechanical injury. (e) Cumulative probability curve for defining the stretch-based thresholds for (or inverse tolerance of) primary injury based on Calcein AM (50%, solid; 10%, dashed; 5%, dotted). (f) Points were chosen for volumes (data from f highlighted in magenta) fluorescently labeled for f-actin (FA, royal blue; $n = 1003$ points over $N = 17$ volumes), MAP2 (M2, sky blue; $n = 291$, $N = 8$), and β3-tubulin (β3, spring green; $n = 390$, $N = 8$), converted into 3D radial measurements from the bubble center, and plotted versus the maximum bubble radius. (g) For a subset of samples, end-point, 3D immunofluorescence imaging provided further insight into structure-specific injury thresholds. Degenerate and damaged projections were manually tagged within each sample ('x', magenta) through visual inspection. (h) Cumulative probability curve for defining the stretch-based injury thresholds (or injury tolerance) for f-actin, β3-tubulin, and MAP2 (50%, solid; 10%, dashed; 5%, dotted). Scale bar for all images is 100 μm.

For each experiment pre- and post-cavitation, Calcein AM volumes are compared using a custom image subtraction scheme in tandem with a quality-factor-based image correlation technique [148] to determine a quantitative radial assessment for primary injury, R_{PI} (Figure 3.2c). Across all sampled values for $R_{\max}$, the primary injury radius-to-maximum bubble radius ratio, $a_{\mathrm{PI}} = R_{\mathrm{PI}}/R_{\max}$ was direct (bisquare $R^2 = 0.869$; $N = 219$) with median $a_{\mathrm{PI}}^{50} = 0.969$ (Figure 3.2d, green).

Due to the observation that injury occurs with less frequency further away from the bubble center, we construct an inverse injury tolerance curve, similar in spirit to the Wayne

State Injury Tolerance Curve [151], for neural cells (Figure 3.2e). Within the context of this study, injury is defined pathomorphologically using either Calcein AM or immunochemical markers for f-actin, $\beta 3-$tubulin, and MAP2. Morphologically degenerate cellular features are identified in comparison to the healthy base state prior to mechanical loading and spatially marked with respect to the center of the cavitation bubble. Using Eqns. 3.1–3.4, we can define critical injury or damage stretch thresholds based on their position within the 3D image and relative to the stress-free, equilibrium bubble by,

$$\lambda_i \equiv \lambda^i_{\theta,\max} = \lambda_{\theta,\max}(r_0 = R_i) = \left[1 + \left(\frac{R_i}{R_{\max}}\right)^{-3} - \left(\frac{R_0/R_{\max}}{R_i/R_{\max}}\right)^3\right]^{1/3} \tag{3.7}$$

where R_i corresponds to the radial position at equilibrium identifying morphologically degenerate cellular features within each 3D image (Figure 3.2) for each of the employed structural markers, i.e., $i = \{$primary injury (PI; Calcein AM), f-actin (FA), $\beta 3$-tubulin ($\beta 3$), MAP2 (M2)$\}$. To reduce subsequent notation burden, we will henceforth write the maximum hoop stretch at a position $r_0 = R_i$, $\lambda^i_{\theta,\max}$, much more simply as λ_i.

For example, to calculate the critical injury threshold for primary injury (characterized by a loss in Calcein AM signal, Figure 3.2c) Eq. 4.1 can be recast in terms of Λ_0 and a_{PI} using the information provided by Figure 3.2d (i.e. the slopes of $R_{\mathrm{PI}}/R_{\max}$ and $R_0/R_{\max}$) as,

$$\lambda_{\mathrm{PI}} \equiv \lambda_{\theta,\max}(r_0 = R_{\mathrm{PI}}) = \left[1 + (a_{\mathrm{PI}})^3 - \left(\frac{a_{\mathrm{PI}}}{\Lambda_0}\right)^3\right]^{1/3}. \tag{3.8}$$

The specific value of a critical injury threshold can then, in general, be defined according to any desired percentile value within the cumulative distribution function; we report the stretch values corresponding to 5% (dotted), 10% (dashed), and 50% (solid) values as intuitive potential threshold options. These stretch values represent the stretches below which we only observe injury in the corresponding percentage of samples. For example, the 5% injury threshold signifies a stretch value below which only 5% of the samples sustained injury at lower stretches, or alternatively, 95% of samples were injured at stretches greater than the 5% threshold value. The [5-10-50]-th percentile thresholds correspond to stretch values, λ_{PI}, can be found summarized in Table 3.3 and are on the order of ~ 1.2.

	Hoop Stretch λ_θ [−]			Hoop Strain $E_{\theta\theta}$ [−]		
Percentile:	**5th**	**10th**	**50th**	**5th**	**10th**	**50th**
Primary Injury	1.152	1.187	1.287	0.141	0.171	0.253
f-actin	1.118	1.151	1.362	0.111	0.140	0.309
MAP2	1.061	1.075	1.182	0.059	0.073	0.168
β3-Tubulin	1.132	1.153	1.261	0.124	0.143	0.232
	Hoop Strain Rate $\dot{E}_{\theta\theta} \times 10^4$ [s^{-1}]			**Cellular Stress** $\sigma_{\theta\theta}$ [kPa]		
Percentile:	**5th**	**10th**	**50th**	**5th**	**10th**	**50th**
Primary Injury	1.143	1.424	2.259	2.404	2.871	4.101
f-actin	0.879	1.133	2.917	1.928	2.386	4.956
MAP2	0.448	0.557	1.384	1.062	1.294	2.807
β3-Tubulin	0.987	1.154	2.029	2.128	2.421	3.781

Table 3.3: **Critical mechanical thresholds at {5,10,50}-th percentile thresholds.** Critical stretch, hoop strain, hoop strain rate, and cellular stress estimates at the [5,10,50]-th percentiles of the cumulative injury function (Figs. 3.2 and 3.5) for each of the examined cellular and cytoskeletal damage features.

To provide more detail on the pathological outcome of commonly reported structural constituents within the neural cells, we performed immunocytochemistry on a subset of samples. In contrast to the primary injury radii which are determined per sample (N), determination of critical injury thresholds for f-actin, $\beta 3-$tubulin, and MAP2 are calculated at all manually tagged locations (n) within the immunofluorescence image of each sample (Figure 3.2f). More details on the identification and tagging procedure is described in Chapter 3 Section 3.1. Analogous to calculating the primary injury critical stretch threshold, we calculate the critical point-wise stretch values via Eq. 4.1 for f-actin ($N = 17, n = 1003$), $\beta 3-$tubulin ($N = 8, n = 380$), and MAP2 ($N = 8, n = 291$) using their respective radii ratios shown in Figure 3.2g. As before, we construct a cumulative distribution function to determine critical structural injury thresholds for the [5-10-50]-th percentile of damaged projections for each marker (Figure 3.2h). The stretch values for the 5%, 10% and 50% injury thresholds of $\{\lambda_{\text{f-actin}}, \lambda_{\text{MAP2}}, \lambda_{\beta\text{3-tubulin}}\}$ are summarized in Table 3.3 and range from approximately 1 to 1.7.

To visually illustrate how well each of the above determined injury thresholds compares with representative micrographs for each of the identified structural markers, we overlay

the calculated injury risk percentiles on maximum intensity projections of representative 3D volumes which experienced approximately equivalent maximum bubble expansion and hoop stretch ($R_{\max}$, Figure 3.3). Figure 3.3a highlights the superposition of Calcein AM images taken before and after mechanical loading as an anaglyph image, while Figure 3.3b–d are immunofluorescence images selecting for f-actin, MAP2, and β3-tubulin, respectively. Figure 3.3e–h highlights cells around the 5th, 10th and 50th percentile injury thresholds, with the primary injury radius R_{PI} highlighted by the magenta line, and several damaged projections highlighted by magenta triangles. Qualitatively, these images show that injury threshold percentiles between 10% and 50% provide a good lower (conservative) bound for predicting high-rate cellular injury. Up to this point, we have computed critical, stretch-based injury thresholds for Calcein AM, f-actin, MAP2, and β3-tubulin, and provided both a qualitative and quantitative assessment of the accuracy of these metrics in predicting structural (or primary) injury in our 3D *in vitro* model of TBI (Figs. 3.1-3.3). However, it is important to note that the deformations applied by the expanding and collapsing microcavitation bubble occur in a rapid, oscillatory fashion (Figure 3.4a-b) subjecting cells to significant changes in the applied loading rate. Instead of expressing the rate of deformation in terms of a stretch rate, we utilize the widely used metric of strain rate.

The advantage here is that both strain rate and strain are commonly-employed quantification metrics of mechanical deformations used in cell mechanics, biophysics [4, 95, 141, 152, 153] and computational modeling of brain injury [10, 11, 154, 155]. Conveniently, the logarithmic, or Hencky, strain is simply defined as the natural log of the material stretch, i.e., $E_{\theta\theta} = E_{\phi\phi} = \ln(\lambda_\theta)$, and $E_{rr} = -2\ln(\lambda_\theta)$, where both strain and stretch are functions of position r_0 and time t. As neural cells are commonly considered to be susceptible to tensile deformations [20, 156–159], we concern ourselves primarily with the tensile hoop strain components $E_{\theta\theta} = E_{\phi\phi}$, just as we did in the case for the hoop stretch, λ_θ. The strain rate is then the material (or total) time derivative of the material hoop strain, $\frac{dE_{\theta\theta}}{dt}$ denoted $\dot{E}_{\theta\theta}$. The selection of strain reporting criteria is up to the end-user, and conversion of our reported Hencky strain to other commonly used strain metrics (e.g., Equivalent von Mises strain and maximum principal strain (MPS)) can be accomplished as described below.

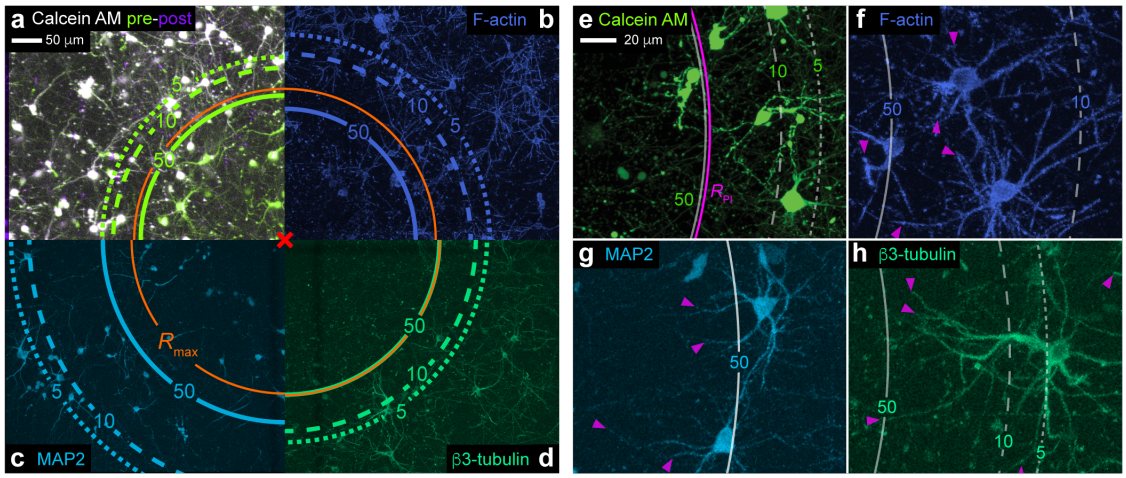

Figure 3.3: **Representative maximum intensity projection micrographs of neural cell injury pathology and associated injury thresholds limits.** (a) Anaglyph maximum projection image of pre- (green) and post-cavitation (purple) states of neural cells in 3D culture illustrating the damaging effect of a high-rate mechanical loading event; cells remaining healthy and intact are shown in white (indicating colocalization in both pre- and post-cavitation images). End-point maximum intensity projection images of immunocytochemical markers show (b) f-actin (royal blue), (c) MAP2 (sky blue), and (d) β3-tubulin (spring green) post-cavitation. For a-d, the bubble epicenter is located at the respective image corner (red 'x'), and overlaid are the sample-specific $R_{\max}$ size (orange). Scale bar, 50 μm. Expanded maximum projection micrographs of (e) live-stained neural cells (green) with (dataset-specific) associated primary injury radius (R_{PI}, magenta) and cytoskeletal components (f) f-actin (royal blue), (g) MAP2 (sky blue), and (h) β3-tubulin (spring green) with (dataset-specific) tagged damaged projections (triangles, magenta) after high-rate mechanical loading. For (e-h), scale bar, 20 μm. For all panels, overlaid are the corresponding 50% (solid line), 10% (dashed line), and 5% (dotted line) injury percentiles from the population analysis (Figure 3.2), scaled by the sample-specific maximum bubble radii $R_{\max}$.

Equivalent, or von Mises Strain. In general, a deformation-based primary strain injury criteria $\bar{E}_c$ first assumes that failure is just a function of (e.g. Hencky) strain, e.g. $f(\mathbf{E}) = \bar{E}_c$. If the failure criterion for cells is considered to be isotropic, the function f depends only on the principal invariants of $\mathbf{E}$, namely $I_1 = \mathrm{tr}(\mathbf{E})$ (in our case, zero due to the assumption of incompressibility), $I_2 = E_{ij}E_{ij}$, and $I_3 = \det(\mathbf{E})$, implying $f(I_2, I_3) = \bar{E}_c$. It is important to note that cells may be affected differently in compression and tension; various studies have imposed different types of quasistatic deformation or moderate strain-rate deformation fields [4,95,141] and found different types of resulting cytoskeletal and plasmalemma damage. As the case of ultra-high-rate tensile versus compressive deformation on neural cells has not yet been well characterized, we could remove reliance of $\bar{E}_c$ on I_3, which encodes the difference between compressive and tensile deformation. Sole dependence on I_2 allows us to conveniently formulate the injury criterion $\bar{E}_c$ using the equivalent, or von Mises strain $\bar{E}$, written generally as

$$\bar{E} = \sqrt{\frac{2}{3}E'_{ij}E'_{ij}}, \tag{3.9}$$

where E'_{ij} is the deviatoric portion of the hencky strain, and in the specific case of spherical bubble motion with local incompressibility we can define the equation for logarithmic (or Hencky), strain straightforwardly as the natural log of the material stretch, i.e., $E_{\theta\theta} = E_{\phi\phi} = \ln(\lambda_\theta)$, and $E_{rr} = -2\ln(\lambda_\theta)$, as previously discussed. This yields the relation that the Equivalent strain is given by,

$$\bar{E} = \sqrt{\frac{2}{3}\left[4\ln(\lambda_\theta)^2 + \ln(\lambda_\theta)^2 + \ln(\lambda_\theta)^2\right]} = 2\ln(\lambda_\theta). \tag{3.10}$$

Maximum Principal Strain. Since the bubble is spherically symmetric, and the system is considered to not rotate during bubble motion, the deformation state is purely that of normal stretches. By definition, a deformation state comprised only of normal stretches is a *principal state*. The further assumption of incompressibility defines the relation between radial and hoop (in both angular directions) stretches and strains. The deformation gradient

tensor for the incompressible, spherically symmetric bubble is given by:

$$\mathbf{F} = \begin{bmatrix} \lambda_\theta^{-2} & 0 & 0 \\ 0 & \lambda_\theta & 0 \\ 0 & 0 & \lambda_\theta \end{bmatrix}, \tag{3.11}$$

where $\lambda_\theta(r_0, t) = r(r_0, t)/r_0$ is the circumferential, or hoop stretch experienced by a material point originally located at a radial position r_0 at later times, t. The logarithmic (true, or Hencky) strain in the material outside the bubble is then the logarithm of this matrix, resulting in

$$\mathbf{E} = \begin{bmatrix} -2\ln(\lambda_\theta) & 0 & 0 \\ 0 & \ln(\lambda_\theta) & 0 \\ 0 & 0 & \ln(\lambda_\theta) \end{bmatrix}. \tag{3.12}$$

The maximum principal strain (MPS), or largest value of strain, then depends on whether the bubble is larger or smaller than the equilibrium radius. For a bubble larger than the equilibrium radius, $\mathrm{MPS}(R(t) > R_0) = E_{\theta\theta} = E_{\phi\phi} = \ln(\lambda_\theta)$. In a state where the bubble is smaller than the equilibrium radius the MPS is instead the radial component of strain, or $\mathrm{MPS}(R(t) > R_0) = E_{rr} = -2\ln(\lambda_\theta)$.

In line with the literature indicating the susceptibility of neural cells to tensile deformations as discussed earlier, the remainder of this work will utilize logarithmic strain metrics. Figures 3.4b and 3.4c provide a general overview of the dynamic changes in hoop stretch (Figure 3.4b), hoop strain and strain rate (Figure 3.4c) at the bubble wall, which is the location of maximum stretch and strain generated in the material. One apparent feature in each of the plots in Figures 3.4b and 3.4c are the sharp curvature points around the various bubble collapse points (e.g., $t \simeq 20\mu s, 40\mu s$, etc.), which produces some of the highest loading rates observed in the material ($\dot{E}_{\theta\theta} > 10^7$ s^{-1}). To fully resolve these transitions in bubble and material behavior we utilize our previously developed inertial microcavitation rheometry (IMR) technique, which allows for both least squares fitting and temporal interpolation of the entire cavitation process.

During maximum expansion, logarithmic hoop strains near the bubble wall are large

and finite, peaking at $E_{\theta\theta} = 1.81$ for the representative sample in Figure 3.4c (blue curve). Logarithmic strain rates (Figure 3.4c, red dotted curve) are similarly large, reaching peak values of $\dot{E}_{\theta\theta} = 10^{7.4}$ 1/s at the time of bubble collapse, t_c. At all times, the applied strain rates as shown in Figure 3.4c are significantly higher than those commonly reported in the blunt and mild TBI literature [4, 95, 129, 160], consistent with high-loading rate phenomena encountered in blast, cavitation or pressure-driven (sonic) scenarios. Analogous to our stretch calculations, we compute the time-maxima of the hoop strain due to the cavitation bubble, $E_{\theta\theta}^{\text{marker}} \equiv \max_t (E_{\theta\theta}(r_0 = R_{\text{marker}}, t))$, and of its associated strain rate, $\dot{E}_{\theta\theta}^{\text{marker}}$, at the percentile damage threshold locations. The critical hoop strains, $\{E_{\theta\theta}^{\text{PI}}, E_{\theta\theta}^{\text{FA}}, E_{\theta\theta}^{\text{M2}}, E_{\theta\theta}^{\beta 3}\}$, and maximum strain rates, $\{\dot{E}_{\theta\theta}^{\text{PI}}, \dot{E}_{\theta\theta}^{\text{FA}}, \dot{E}_{\theta\theta}^{\text{M2}}, \dot{E}_{\theta\theta}^{\beta 3}\}$ at the [5-10-50]-th percentile damage threshold locations are summarized in Table 3.3 and are on the order of 0.06 to 0.25, and $\sim 10^4 \text{s}^{-1}$, respectively. It is notable that the peak instantaneous strain rate, $\dot{E}$, occur at the time of first collapse.

Since neural cells, like many other bodily tissues, are well-described as rate-dependent viscoelastic materials, one way to account for both the large strains and high strain rates experienced by the cells is to introduce a rate-dependent, large deformation constitutive model for estimating actual cell stresses. Such an approach is quite common for biological scenarios that show strong loading rate dependence [161, 162]. To estimate the deviatoric (i.e. removing the effect of the atmospheric baseline pressure, p_∞) cellular stresses we employ a simple, non-linear Neo-Hookean Kelvin-Voigt model capable of both describing the large strain elastic, and high-rate viscous behavior. Furthermore, based on our prior work [4], we assume displacement continuity across the cell-collagen gel interface, allowing us to prescribe the same strains and strain rates to the cells as measured by IMR in our neural tissue model (Figure 3.4c). The deviatoric hoop stress for a non-linear Kelvin-Voigt material takes the form of:

$$\sigma_{\theta\theta} = \frac{G}{3}\left(\lambda_\theta^2 - \lambda_\theta^{-4}\right) + \frac{2\mu\dot{\lambda_\theta}}{\lambda_\theta}, \tag{3.13}$$

where G and μ denote the dynamic shear modulus and viscosity of the material, respectively. It can be seen from Eq. 3.13 that the total cell stress in the Kelvin-Voigt model is a straightforward addition of the elastic and viscous stress terms.

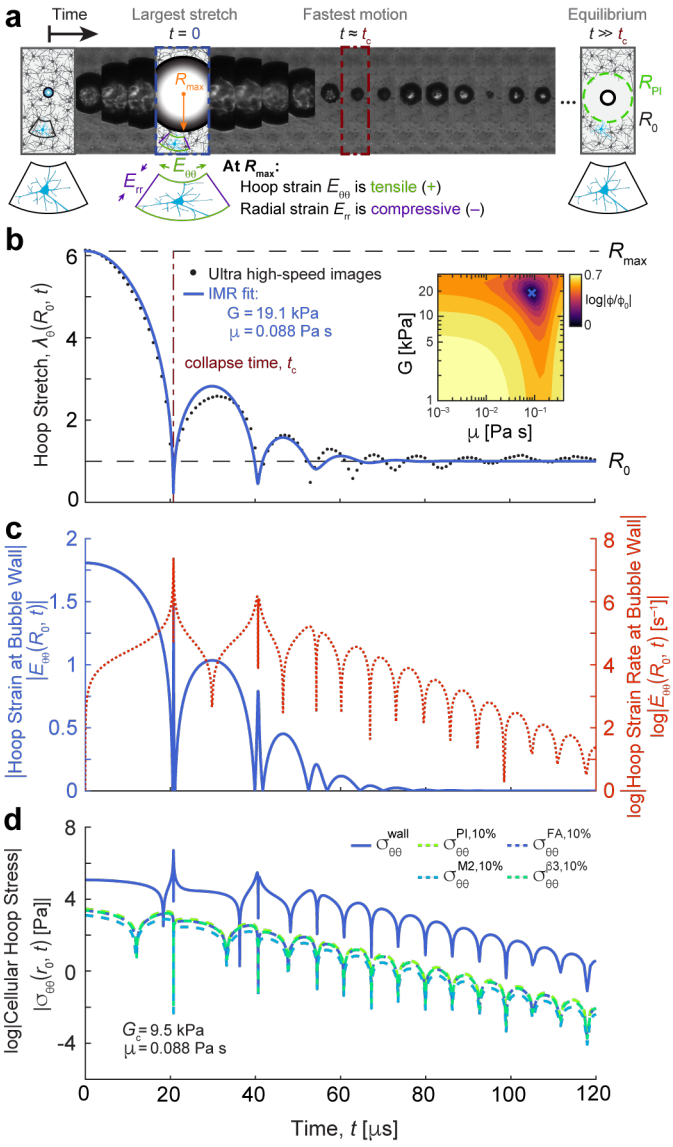

Figure 3.4: **Temporal evolution of the applied and experienced cellular deformations and stresses.** (a) High-speed time-lapse image series of a representative oscillating cavitation bubble generated inside the 3D neural tissue scaffold. $R_{\max}$ and R_0 denote the maximum and equilibrium bubble radii, respectively, from which all relevant deformation quantities are calculated. (b) Generated material hoop stretch at the bubble wall, $\lambda_\theta(R_0, t)$, due to the microcavitation bubble. Black dots indicate experimental data points extracted from high-speed videography to compute hoop stretch. Solid blue lines denote best fit, demonstrated by a defined minimum in the least squares error cost function space $\phi(G, \mu)$ (inset), of the cavitation dynamics using our previously developed IMR technique [127] and assuming the neural tissue to be well-described by a non-linear Kelvin-Voigt material model (See Chapter 3 Section 3.2). (c) Temporal evolution of the absolute magnitude of the logarithmic (Hencky) hoop strain, $E_{\theta\theta}(R_0, t)$ (blue line), and the temporal evolution of the log of the magnitude of the hoop strain rate, $\dot{E}_{\theta\theta}$ (dashed orange line), each computed from the IMR best-fit material properties in (b). (d) Absolute cellular hoop stress estimates over time, assuming a nonlinear Kelvin-Voigt constitutive model with $G = 9.5$ kPa and $\mu = 0.088$ Pa·s, at the bubble wall (solid blue) and spatial locations corresponding to the 10% damage thresholds for primary injury (PI, dashed green), β3-tubulin (β3, dashed spring green), MAP2 (M2, dashed sky blue), and f-actin (FA, dashed royal blue).

To compute cellular stresses we estimate both G and μ from previously published literature estimates. The elastic properties for neural cells can vary based on the examined subcellular compartment, with somatic values approaching several hundred Pa [163] and stiffness estimates of axonal projections ranging from 9.5-12 kPa [164,165]. Considering that most of our pathology overwhelmingly presents degeneration and damage along cytoskeletal projections, we adopt $G = 9.5$ kPa as our elastic parameter for estimating the mechanical stresses within neural cell projections. Given a scarcity of viscosity measurements for cells, particularly for neural cells under high loading rates, we estimate the dynamic viscosity, μ, for our neural cells using a combination of material calibration measurements via IMR, and

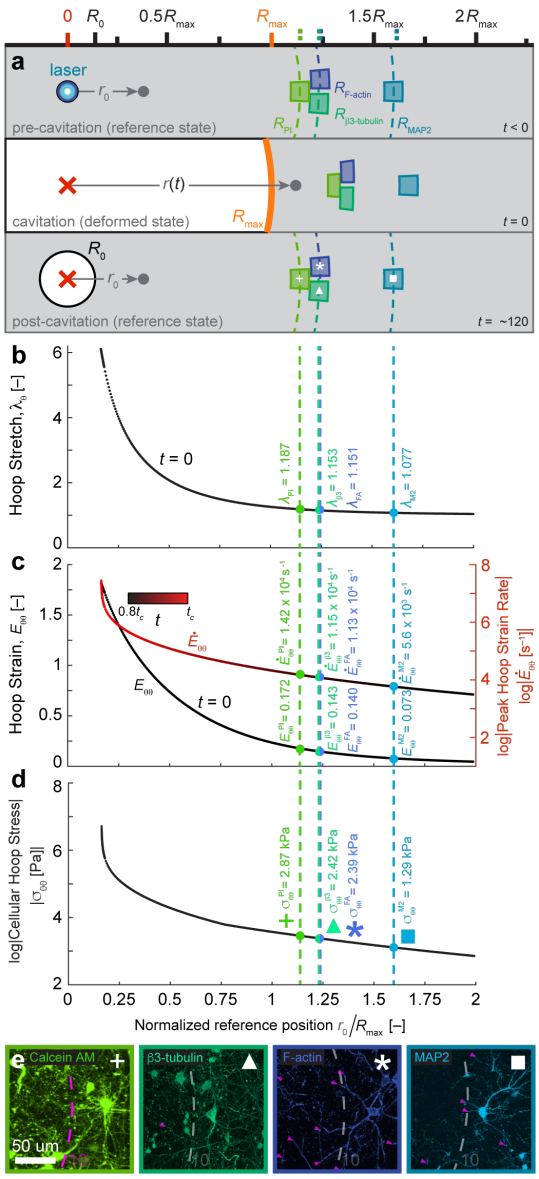

Figure 3.5: **Critical injury thresholds for neural cells in terms of stretch, logarithmic (Hencky) strain and strain rate, and cellular stress as a function of normalized position r_0/R_{max}.** (a) Shown is a to-scale three-panel schematic of our neural tissue just before cavitation ($t < 0$), at maximum bubble size ($t = 0$), and at quasi-equilibrium post-cavitation ($t \gg 0$). Highlighted are representative volumes at the true spatial locations of the 10th injury percentile for primary injury (PI; green plus), and degenerate projections for β3-tubulin (β3, spring green, triangle), f-actin (FA royal blue, star), and MAP2 (M2, sky blue, square). During maximum bubble expansion volumes are displaced and stretched, with volumes closer to the bubble wall experiencing higher strain than those farther away. (b) Hoop stretch, λ_θ, as a function of normalized radial distance within the neural tissue at time of maximum bubble expansion/tissue stretch and to-scale with (a). (c) Hoop strain at maximum bubble expansion (black) and strain-rate (red to black gradient) as a function of position in the material during the full dynamic cavitation process. (d) Cellular hoop stresses as a function of position corresponding to the positions of 10th percentile injury (e) Representative fluorescent maximum intensity projections of injured cells at positions of the 10% damage thresholds for primary injury, β3-tubulin, f-actin, and MAP2.

a scaling argument based on literature values. First, using IMR we determined the dynamic viscosity of our 3D collagen-cell *in vitro* model to be approximately 0.088 Pa·s (Figure 3.4b). Since the volume fraction of neural cells within our collagen scaffold is less than one percent, we assume that the viscous behavior is predominantly driven by the collagen fibers. When comparing our high-rate, dynamic viscosity measurement to low, or quasi-static rate ($\sim$ 0.1–1 Hz) estimates from the literature for type I collagen gels, i.e., values around $\sim$ 2–3 Pa·s [166, 167], we, consistent with the literature, attribute this discrepancy to the well-known shear-thinning effect of collagen at high-rate [168, 169]. Since quasi-static, low frequency estimates on the dynamic viscosity in neurons have been reported to be around

$\sim$ 2–3 Pa·s [170], which is very similar to type I collagen at low frequencies, we assume a similar scaling on the high-rate dynamic viscosity as we did with collagen, and thus assign the same value of our cell-gel system to the cells directly, i.e., $\mu = 0.088$ Pa·s.

Figure 3.4d displays the temporally evolving cytoskeletal cell stresses at the bubble wall (solid blue), as well as at the locations corresponding to the 10th percentile injury probability for each of the cytoskeletal structures (dashed). Estimates of the maximum stress experienced by cells at positions of interest, $\sigma_{\theta\theta}^{\text{marker}} \equiv \max_t \left(|\sigma_{\theta\theta}^{\text{marker}}(r_0 = R_{\text{marker}}, t)|\right)$, corresponding to the [5,10,50]-th damage thresholds for $\{\sigma_{\theta\theta}^{\text{PI}}, \sigma_{\theta\theta}^{\text{FA}}, \sigma_{\theta\theta}^{\text{M2}}, \sigma_{\theta\theta}^{\beta 3}\}$, are summarized in Table 3.3 and range from $\sim$1-5 kPa. Since the cellular stresses are a sum of the rate-dependent viscous and rate-independent elastic stress contributions, the shape and evolution of the cell stresses present a temporal shape evolution in between $E_{\theta\theta}$ and $\dot{E}_{\theta\theta}$ (Figure 3.4c), with the highest stresses occurring closest to the bubble wall ($\sim$ 5.2 MPa).

3.4 Discussion

Our current ability to predict, diagnose, and mitigate high-rate tissue injuries such as those that arise during advanced, sonic- and laser-based medical treatments, or in hazardous environments including blast and directed energy exposures, is limited by our understanding of the unique pathology of high-rate injury itself and the resolution of associated critical injury thresholds. By carefully integrating a physiologically relevant, 3D *in vitro* neural tissue culture model with our recently pioneered inertial microcavitation rheology (IMR) technique, we provide high-resolution, structural information on the unique injury pathology of cells experiencing high-rate mechanical loading, i.e., strain rates in excess of 10^3 1/s. Using 3D volumetric image reconstruction via confocal and multiphoton imaging in tandem with IMR, we provide quantitative estimates of several key physical quantities producing this pathology (Figure 3.5). Specifically, we provide estimates of critical stretch, strain, strain rate and cell stress thresholds for the failure of neural projections containing common subcellular structural components such as microtubules, filamentous actin (f-actin), and microtubule-associated protein-2 (MAP2).

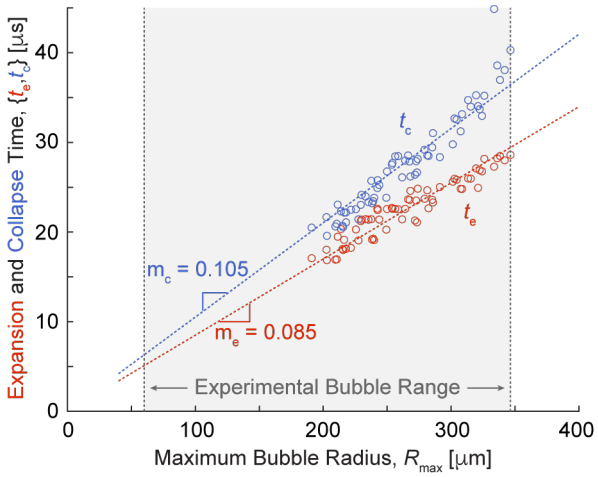

Figure 3.6: **Bubble expansion and collapse times as a function of maximum bubble radius.** Time from nucleation to maximum bubble radius (t_e; red circles) and the time from maximum bubble radius to collapse (t_c; blue circles) as a function of maximum bubble radius, R_{max}, estimated as the roots of a quartic function fit to the first expansion-collapse cycle of all high sampling frequency (1.0 MHz) data. Linear regression coefficients ($m_e = 0.085, m_c = 0.105$) are used to estimate expansion times for data within the experimental bubble range (grey shaded region).

In particular, we observe differing stretch tolerances of projections containing different subcellular components, which can be found summarized in Table 3.3 and Figure 3.5. To estimate an effective loading strain rate leading to maximum tissue strain ($E_{\theta\theta}$), we compute the average loading strain rate, $\overline{\dot{E}}_{\theta\theta}$, as the maximum tissue strain, i.e., $E_{\theta\theta}$ at the time of R_{max}, divided by the time to full bubble expansion, t_e (Figure 3.6). Since t_e is dependent on the actual final bubble size (R_{max}), whereas the maximum tissue stretch and strain are only dependent upon the ratio of R_{max}/R_0, we can only provide a general range of average loading strain rates for a nominally single value of critical injury stretch (Table 3.4). In analyzing the relatively conservative 10th percentile stretch damage thresholds we find that, in order of decreasing stretch sensitivity, projections containing MAP2 are damaged at the lowest strains of $E_{\theta\theta}^{\mathrm{M2}} = 7.3\%$ ($2.5{\times}10^3 \lesssim \bar{\dot{E}}_{\theta\theta}^{\mathrm{M2}} \lesssim 1.4{\times}10^4\ s^{-1}$), followed by f-actin- and β3-tubulin-containing projections at strains of $E_{\theta\theta}^{\mathrm{FA}}, E_{\theta\theta}^{\beta 3} \simeq 14\%$ ($4.9 \times 10^3 \lesssim \bar{\dot{E}}_{\theta\theta}^{\beta 3}, \bar{\dot{E}}_{\theta\theta}^{\mathrm{FA}} \lesssim 2.8 \times 10^4\ s^{-1}$) (Figure 3.5c). The total disruption of overall cellular architecture (R_{PI})—specifically the depletion of intracellular esterase activity—was found to require the largest strains of $E_{\theta\theta}^{\mathrm{PI}} = 17\%$ ($6.0 \times 10^3 \lesssim \bar{\dot{E}}_{\theta\theta}^{\mathrm{PI}} \lesssim 3.4 \times 10^4\ s^{-1}$).

Average Loading Strain Rate ('Largest — Smallest' Bubble Size), $\overline{\dot{E}_{\theta\theta}}$ $[s^{-1}]$		
	Wall	**5th-PCTL**
Bubble Wall	$6.3 \times 10^4 - 3.6 \times 10^5$	—
Primary Injury	—	$8.8 \times 10^3 - 5.0 \times 10^4$
F-actin	—	$1.1 \times 10^4 - 6.1 \times 10^4$
MAP2	—	$5.9 \times 10^3 - 3.3 \times 10^4$
β3-Tubulin	—	$8.1 \times 10^3 - 4.6 \times 10^4$
	10th-PCTL	**50th-PCTL**
Bubble Wall	—	—
Primary Injury	$6.0 \times 10^3 - 3.4 \times 10^4$	$4.9 \times 10^3 - 2.8 \times 10^4$
F-actin	$4.9 \times 10^3 - 2.8 \times 10^4$	$3.8 \times 10^3 - 2.2 \times 10^4$
MAP2	$2.5 \times 10^3 - 1.4 \times 10^4$	$2.1 \times 10^3 - 1.2 \times 10^4$
β3-Tubulin	$5.0 \times 10^3 - 2.8 \times 10^4$	$4.3 \times 10^3 - 2.5 \times 10^4$

Table 3.4: **Effective loading strain rate ranges.** Lower and upper bounds estimates of effective loading strain rate for the largest to smallest bubbles observed experimentally, respectively, at [5,10,50]-th percentiles of the cumulative injury function for each of the examined cellular and cytoskeletal damage features.

The selection of the cytoskeletal markers examined here are intended to provide granularity with respect to the susceptibility of cell-type and neuronal sub-compartments to high-rate, stretch-induced damage. Given the nature of our polyculture of neuronal and glial cells used here, the selection of β3-tubulin for microtubules provides specificity for neuronal projections, whereas f-actin is general to the full neural cell population (including astrocytes) providing a more general projection failure criteria across all cell-types [56]. The measured failure of f-actin- and microtubule-containing projections, in aggregate, under nearly equivalent loading, is intuitive at diffraction-limited length scales for the following reason. F-actin and microtubules are co-localized throughout the majority of the cytostructure of most neural cells despite having different intracellular organization and persistence lengths based on the sub-compartment and cell type examined [46, 158, 159]. For example, in the axon of a neuron, f-actin forms periodic ring structures with spectrin and other proteins, while microtubules form long aligned structures along the length of the projection [171]. Both f-actin and microtubule components have been shown to exhibit a rate-dependent susceptibility *in silico* to tensile failure in neural cells with an increased dependence on the rate of deformation [157–159]. These high-rate ($10^8 - 10^9$ 1/s) molecular dynamics (MD) simulations

indicate that onset of failure for microtubules and actin-spectrin structures begins at different logarithmic strain thresholds of ~ 0.15 and ~ 0.17, respectively [157,159]. The closeness of our measured 10th percentile stretch damage thresholds (at strains of ~ 0.14) for both f-actin and microtubules, coupled with the MD prediction of different failure criteria for f-actin and microtubules, suggests that in the combined system microtubules may act as the limiting component of the projection structure. It might also suggest that beyond a critical strain rate, i.e., $\dot{E}_{\theta\theta} \sim \mathcal{O}(\gtrsim 10^3\ 1/\text{s})$, that the critical injury strain, or strain to failure, may be relatively strain rate insensitive. Finally, The damage of projections containing MAP2, which is generally consigned to microtubules of the dendrites of mature neurons [172], occuring at lower strain thresholds (~ 0.07) than the general neuronal microtubule-containing (~ 0.14 strain) projections suggests the existence of a dependence on the micro-structural differences of axons vs. dendrites [171] with respect to strain tolerance. We thus interpret the apparent failure of MAP2-containing, or dendritic, projections (under equivalent loading) at a lower strain threshold as the potential existence of a stress-dependent injury criterion.

The existence of a stress-dependent injury criterion can be intuitively understood through the notion that a load exerted on a structure will be experienced differently depending on the organization and interaction between the structural components within the system. A more nuanced interpretation comes from an understanding of the role the organization and structure of the cytoskeleton of different subcellular compartments play in the cells' susceptibility to injury. The arrangement of microtubules differs between neuronal compartments. Axons can consist of $\sim 10 - 100$ microtubules organized into uniform bundles with the plus-end oriented toward the synapse; these bundles are stabilized through binding with tau proteins [63], whereas in dendrites the microtubule orientation is diverse, with many microtubules oriented with the minus-end oriented away from the cell body stabilized by MAP2 [63,172]. Similarly, the organization of f-actin in the axon and dendrites differ. In the axon, f-actin and spectrin form periodic rings along the length of the axon, whereas the dendrites consist of a mix of linear and branched f-actin networks [60,171]. The rate dependence for failure of these structures has been shown to relate to protein associations within the

structure, including the susceptibility of spectrin unfolding under high-rate loading for f-actin failure [157], and sliding-stretching behavior of microtubules through the viscous unfolding and dissociation of microtubule-associated proteins [173]. The rate-dependent protein association and micro-scale structural protein architecture differences signal the importance of mechanical thresholds that take into account the complexity of the stresses experienced at locations of cellular failure. To address this, we provide initial estimates of the cellular stress for neural projection failure (Figure 3.5c), as summarized in Table 3.3 at the [5-10-50]-th stretch damage thresholds. While these estimates incorporate the non-linear elastic, and linear viscous/rate-dependent contributions of the physical structure of each neural cell, they only provide whole system (i.e., the entire cellular projection modeled as one) stress estimates, rather than stress estimates on the actual subcellular structural units. Resolution of subcellular, protein-level-specific injury stresses is an exciting area of active research, and current modeling efforts should shed more light onto the distribution of internal stresses within the overall structure-level stresses presented here. The representative morphology of cellular damage metrics is highlighted at the 10th percentile damage thresholds in Figure 3.5e, where example degenerate projections can be seen highlighted.

Lastly, we note that all of the observed cellular injury falls within 2.5 times of the maximum bubble radius for each data set (Figure 3.1d), beyond which all strains and elastic stress contributions become negligible (e.g., $E_{\theta\theta} < 2.5\%$) Figure 3.5c-d. Interestingly, the strain rate remains non-zero (Figure 3.5c) leading to a small remnant deviatoric viscous stress (< 400 Pa), which we do not observe to be injurious. These spatial scaling observations are consistent with our previous analysis of inertial cavitation bubbles showing that most of the significant material deformations occur within 2.5 times $R_{\max}$ from the bubble center [127].

While our work has focused on the acute pathology and structural metrics of injury, future work will investigate potential additional injury sequelae often seen in cellular and tissue injuries, including, but not limited to, the inflammatory response and activation of glial cells including astrocytes and microglia. One of the significant advantages of the high-rate loading model presented here is its optical nature and modularity, that is, it can be

straightforwardly adapted to introduce high-rate loading in tissues of heightened physiological relevance including cortical spheroids, organoids, and *in vivo* tissues [136,174]. It should be noted that while our cavitation-based approach is minimally invasive and modular, the nature of the applied deformations are intrinsically tied to the resulting cavitation bubble dynamics, often introducing an oscillatory, repeated loading pattern of spatiotemporally varying strain and strain-rate. This is a deviation from much of the previous literature on TBI, in which most experimental platforms subjected cells and tissues to relatively simple, single, and uniform deformation profiles [4, 13, 95, 141, 160]. However, one could argue that the cyclic loading profile of the oscillating bubble reflects a more physically realistic loading scenario during real-world events or in clinical applications [136]. As a final note, laser-induction of cavitation (LIC) is inherently a thermal process, and as such it is important to discuss any potential effects of thermal energy deposition on the system. While the temperature fields at the center of the bubble can indeed be significant (upwards of 5000K for a duration on the order of nanoseconds), the critical injury thresholds reported in this paper are a direct result of the mechanical rather than the thermal loading for the following reasons: Prior high-fidelity simulation work has shown that most of the material outside the bubble is near isothermal and ambient temperature conditions and that there is little effective heat transfer across the bubble wall, in particular during the time interval when the material and cells experience maximum stretch and strain [175, 176]. Considering that our critical injury thresholds are derived from measurements significant distances away from the bubble wall (no injury measure was derived from inside the bubble), any possible thermal effect should be negligible. Secondly, due to the stochastic nature of our laser-induced cavitation experiments, several samples where exposed to the same laser pulse but did not cavitate. Yet none of these samples showed any quantifiable change in intracellular esterase signal or cell morphology on the timescales examined or several hours after the regular post-(non-)cavitation imaging when compared to our unexposed control samples.

Our IMR technique is not just limited to investigations detailing neural injury, but rather can be employed broadly across many different tissue models and anatomical constituents.

Finally, while IMR provides a highly controlled and repeatable means of introducing high-rate mechanical loading to cellular and tissue constructs, the theoretical backbone of IMR also allows for the extraction of relevant high-rate material properties from the tissue system under interrogation. In the case for our collagen-based neural cell tissues we showed that using a non-linear Kelvin-Voigt material model, IMR determined the dynamic shear modulus and viscosity to be $G = 19.1$ kPa, and $\mu = 0.088$ Pa·s, which falls within the the range of prior characterization results on brain and brain-like tissues [177,178]. Thus, the IMR framework allows for the inverse determination of the physical properties (for example, the elastic shear modulus, dynamic viscosity, and analogous parameters for other viscoelastic models [15]) for various tissues and cellular systems at high-rate (e.g., ballistic and blast loading rates), which remain to be a significant challenge to obtain via traditional characterization methods. Coupled with data-driven methods for constitutive model identification [179], IMR has considerable potential for high-rate material calibration for these complex biomaterial systems.

In summary, in this study we provide significant new insight into the cellular pathology of neural cells undergoing high-rate deformations such as those arising in advanced sonic and laser-based medical procedures or hazardous environments that feature significant internal or external pressure exposures (e.g., directed-energy or blast exposures). Specifically, we provide quantitative information on the critical stretch, strain and stress values required to injure neural cells during high rating exposures, which should provide a scientific basis for the development of advanced brain injury predictive diagnostics, and mitigation strategies in medical procedures to limit collateral tissue damage, especially in the central nervous system.

Chapter 4

Contribution of Extracellular Matrix Constituents on Neural Cellular Injury Tolerance Thresholds

4.1 Introduction

The natural extension of the work presented in Chapter 3 is to release the samples from the time scale of a purely mechanical, or primary, injury and allow the cells to develop a secondary biochemical, or pathway-dependent, injury pathology in response to high-rate mechanical loading [4,26,31,95,120]. While an experimentally simple extension of this work, requiring the cells be provided only additional time *in vitro* following injury and prior to end-point analysis being completed, it is not without conceptual hurdles.

First, knowledge of the initial pathway drivers responsible for the downstream activation of mechanically-induced cell death in TBI are at present insufficiently understood [120]. As it is widely accepted that mechanotransduction-based pathway activation in response to forces into (and out of) the cell is dependent on the specific connections between the cell and the extracellular space (i.e., integrins, cahderins, etc.), these connections potentially carry important implications for biological outcomes following injury [73, 118–120]. While

collagen-I hydrogels, such as those used in chapter 3, provide a reproducible mechanical system [4, 25, 26, 56] mechanotransduction is limited to signal transmission through $\alpha 1\beta 1$ and $\alpha 2\beta 1$ integrins [86, 87]. Comparatively, integrin connectivity in the CNS is known to be supported through interactions between nine currently documented integrin-ligand pairs [73,86,87]. This presents an overly limited array of avenues for the experimental activation of mechanotransduction-based pathways in response to mechanical loading, making delineation of mechanically-dependent secondary injury thresholds challenging.

Additionally, when considering the development of injury tolerance thresholds for secondary pathway activation it is important to remain conservative. As cells at or above the primary injury tolerance thresholds (Chapter 3) have a higher probability of experiencing projection blunting, or axotomy, it is reasonable to conclude that they would develop a secondary biological pathway response analogous to the observation of Wallerian degeneration following axotomy in the peripheral nervous system (PNS) [25, 180]. While Wallerian degeneration has not specifically been described in neurons of the central nervous system, the existence of this pathway in the PNS shifts the delineation of conservative injury tolerance thresholds beyond cells exclusively experiencing projection blunting or axotomy. Further, given that the deformation field surrounding the injurious cavitation bubble decays rapidly with distance ($\sim 1/\mathrm{r}^3$) away from the bubble wall a conservative secondary injury threshold should reasonably be associated with cells experiencing small stretches and strains below the threshold required for projection blunting. In other words, where cells following deformation remain morphologically in-tact while still presenting with a secondary biochemical injury pathology (e.g., Apoptosis, Reactive Oxygen Species generation, DNA damage, etc.). As the sensitivity of different avenues for the introduction of mechanically-activated cell death through different integrins is unknown [120], it is important to not unduly restrict the availability of cells to form diverse connections to the environment.

Finally, consistent with the potential for an integrin-dependency in secondary injury mechanotransduction discussed above, we cannot reasonably preclude the possibility of an integrin-dependency on a cell's experience of the primary injury loading event. The current understanding of the physical connection between the cytoskeleton and the cytoplasmic

domain of a focal adhesion is believed to be supported by the β-subunit of integrins [90]. Of the nine documented integrin pairs in the CNS, eight have been described as carrying a $\beta 1$ subunit [73, 86, 87]. In this way the examination of high-rate injury phenomenon in a collagen-I system comprised of β subunits consistent with the majority β subunit-type in the native CNS, remains supported. However, as neural cells are considered highly susceptible to tensile deformations [20,156–159] and the application of tensile loading to a cell is dependent on the ability of a cell to maintain its connection to the extracellular space, a potential for an integrin dependent blunting of neural projections from direct mechanical loading remains.

Work in this chapter will begin the exploration of primary mechanical injury in a 3D *in vitro* hydrogel model of increased ligand-diversity to determine whether an integrin-dependency exists within primary mechanical injury at high loading rates. To accomplish this initial work, a 3D hydrogel-based cell culture platform will be created using a mixture cortical neural cells from Sprague-Dawley rat pups and reconstituted basement membrane proteins, or Matrigel, following previously established protocols from Laplaca et al. in their book chapter on 3D neural cell culture [78]. The hydrogel model will be integrated with a laser-induced cavitation system, allowing for spatially-focused application of spherically symmetric deformation fields on neural cellular populations consistent with the methodology employed in Chapter 3. This chapter will aim to validate the assumption that $\alpha 1\beta 1$ and $\alpha 2\beta 1$ integrins are alone sufficient to provide a representative model of physiologically realistic primary mechanical injury pathology *in vitro*.

4.2 Methods

4.2.1 Preparation of 3D Matrigel Hydrogels

**Note: Common reagent mixtures can be found in Chapter 2*

Matrigel (Dow Corning, Tewksbury, MA) hydrogel samples were made to a final concentration of 7.5 mg/mL according to the manufacturer's standard protocol. Stock Matrigel (22 mg/mL) was thawed on ice at 4^oC overnight prior to the day of dissection. As stock

Matrigel is highly viscous, the stock solution is first diluted to an intermediate concentration of $\sim$ 9.5 mg/mL on ice with cortical complete media to aid in the accurate pipette mixing of the solution. After initial dilution, Matrigel is quickly vortexed before being placed back on ice. Matrigel is then diluted to a final concentration of 7.5 mg/mL with cell suspension and triturated on ice until the solution is well mixed ($\sim$10-15 times). Matrigel samples are then cast in the inset well of a glass-bottomed 48-well plate (MatTek, Ashland, MA) by pipetting 60 μL of Matrigel/cell solution into each individual well. The resulting sample geometry is a 6 mm diameter by $\sim$ 2 mm tall cylindrical hydrogel.

Samples were allowed to polymerize in a humidified incubator at 37^{o}C and 5% CO_2 for approximately 20 minutes after which 300 μL of cortical complete media was added to each well. Cells were incubated for 7 days *in vitro* and fed every 24-48 hours to undergo neurogensis, after which time neural cells showed a high degree of network connectivity (Figure 4.1a) consitent with previous work [25].

4.2.2 Live- and fixed-cell Labeling and Image Acquisition

Consistent with protocols outlined in Chapters 2 and 3, Matrigel-based cellular populations were stained for Calcein Acetoxymethyl (AM) to obtain live-cell morphological data analysis. Calcein AM staining protocols were completed in HA+B$-$27 media at a concentration of 20 μM, the incubation time was experimentally extended from previous protocols to a 90 minute incubation in a humidified incubator at 37^{o}C and 5% CO_2 to sufficiently label the Matrigel-embedded neural cells. Following incubation, staining media was replaced with naïve HA+B$-$27 media for imaging in the absence of a CO_2 environment. For all live-cell experiments, calcein AM imaging protocols were extended to a 1$\times$2 large image stitch three-dimensional format, consisting of 1024$\times$1946$\times$11 (1.24$\times$1.24 μm spacing in x-y, 10 μm spacing in z) image z-stacks of neural cells immediately prior to and immediately following the generation of laser-induced cavitation. Images were acquired using a Nikon A-1 multiphoton system, mounted on a Ti2 inverted optical microscope controlled by NIS-elements software (Nikon, Tokyo, Japan). Physiological conditions were approximated via a thermally-controlled 37°C scope-top incubator box with a closed-loop Air-Therm heater

(World Precision Instruments, Sarasota, FL). Samples were secured during imaging using a well plate holder (Ti-SH-W; Nikon), as in previous work, to reduce rigid motion over the course of the experiment. Multiphoton z-stack images of the calcein AM signal were acquired $\pm 50\mu$m above and below the cavitation epicenter (z-height: 600 μm) with a 10 μm z-increment resulting in a pseudo-3D multiphoton volume stacks, consistent with prior work [25]. Samples were deformed through the deposition of a single cavitation event spatially-focused 600 μm above the bottom cover glass within the calcein AM volume. The initiation and recording of cavitation dynamics were acquired consistent with methodologies described in detail in Chapters 2 and 3 [25]. Briefly, 256 frames of 250×400 pixel high-speed videography were acquired for each cavitation event using a Shimadzu HPV-X2 (Shimadzu Corporation, Kyoto, Japan) with time synchronized 10 ns pulsed laser illumination provided by a CaviLux-640 system (Cavitar Ltd., Tampere, Finland). To further decrease the time-delay between cavitation generation and post-cavitation imaging, samples were chemically fixed immediately following cavitation while simultaneously being imaged for the post-cavitation configuration rather than delaying fixation until post-cavitation imaging was completed.

Cellular fixation was accomplished with 4% (v/v) paraformaldehyde and 8% (w/v) sucrose for 30 minutes, before being washed with 1X PBS four times, for 15 minutes each. Samples were subsequently immunolabelled for cytoskeletal markers β3-tubulin and filamentous actin (f-actin) following procedures outlined in chapter 2 and 3 at the concentrations reported in table 3.2. High-resolution immunofluroescence confocal z-stack acquisiton was expanded to acquire 2×3 large image stitches of 1946×2868×101 (0.5×0.5 μm spacing in x-y, 1.5 μm spacing in z) multiphoton micrographs $\pm$75-μm centered 600 μm above the cover glass, as before. The confocal z-stack images were acquired with a 25×/1.15 microscope objective (Nikon Instruments, Japan) with a μm to pixel ratio of 0.5 μm per pixel.

4.2.3 Cavitation Bubble Radial Determination

The general processing procedure for acquiring the maximum bubble radius and equilibrium bubble radius from high-speed video is outlined in Algorithm 1, consistent with previous

work in Chapter 3. Each time series of 256 frames of 400×250 pixels from the Shimadzu HPV-X2 high-speed camera is processed to obtain a single measure of the bubble radii at a frequency of 1.0 MHz (1 μs/frame). Image data is processed in line with established protocols described in detail in Chapter 3 [25].

4.3 Experimental and Analytical Limitations

It is important to note that cavitation initiation in Matrigel samples yielded a significantly higher frequency of asymmetric, or non-spherical, bubble dynamics as compared to Collagen-I samples. This asymmetry is likely attributable to well documented heterogeneous composition of the basement membrane extracellular matrix proteins that make up Matrigel [78]. Discussion of experimental platform improvements required to negate this effect and recover consistent axisymmetric bubble behavior while maintaining the intergrin-ligand interaction diversity afforded by Matrigel are explored below in the 'Initial Results & Discussion' section. Additionally, inherent to platform instabilities of the Matrigel hydrogel system, while pre-cavitation live-cell Calcein AM data represent high-quality analytically process-able data, unfortunately, the post-cavitation Calcein AM data presents with a previously undocumented consistent and distinct z-dependent rigid drift artifact. The observed z-drift is traditionally characteristic of sample movement during image acquistion. Sample movement can be attributed through careful consideration of the experimental platform to either sample delamination from the cover glass substrate at the base of the well or a long timescale, $\mathcal{O}$(minutes), viscoelastic material relaxation following inertial cavitation deposition. Due to corrupted post-cavitation images, image processing through the analytical algorithm described in Chapter 3 is unfeasible. In light of this, discussion of results and findings in this section will carry the important and not to be understated stipulation that further experimental confirmation is required before numerical, quantitative threshold values can be confidently determined, as in Chapter 3. Discussion in this section will represent initial direction setting results indicating the validity of continued work in a Matrigel-based or other suitable integrin diverse ECM composite, as discussed in the 'Initial Results & Discussion' section below.

4.3.1 3D Image Processing

Multiphoton z-stack micrographs acquired in this section were successfully acquired with minimal rigid drift with respect to the site of cavitation initiation, in line with previous imaging protocols [25]. To determine qualitative primary injury radii, R_{PI}, post-cavitation multiphoton z-stack data are manually compared and segmented to attain a single radial measure per sample. To mitigate information biasing of this analysis, manual segmentation of samples were completed blinded from the high-speed videography (radius verses time) data for each sample. Sample processing for cytoskeletal immunofluorescence data as outlined in Algorithm 3 is tied directly to the analytically derived cavitation epicenter and a registration workflow determined in Algorithm 2. This processing workflow was necessarily altered to an initial manual delineation method for aligning Calcein AM and immunofluorescence data sets. Manual cavitation epicenter segmentation was obtained and the midplane of the 150 μm confocal z-stack used as the cavitation epicenter for each sample. Multi-channel cytoskeletal paired samples held a single, consistent, epicenter value for all associated data sets. In line with Algorithm 3 radial distance calculations for each manually segmented blunted projection in 3D were computed with respect to the cavitation epicenter.

4.4 Initial Results & Discussion

To fully investigate the integrin dependence of primary mechanical injury pathology and the critical injury thresholds of neural cells following high-rate mechanical deformations, a 3D *in vitro* hydrogel model of increased integrin diversity is required. In this chapter our recently published work examining the injury tolerance thresholds of neural cells in a collagen-I hydrogel platform is extended into a 3D *in vitro* Matrigel-based hydrogel cell culture platform. The Matrigel *in vitro* model consists of primary dissociated cortical neural cell isolates harvested from P0-P1 Sprague-Dawley rat pups and encapsulated in a 3D Matrigel microenvironment consisting of reconstituted basement membrane proteins, including Laminin and Collagen IV. Neural cellular populations are cultured for 7 days *in vitro*, during which time the cells undergo neurogenesis to form healthy and randomly oriented

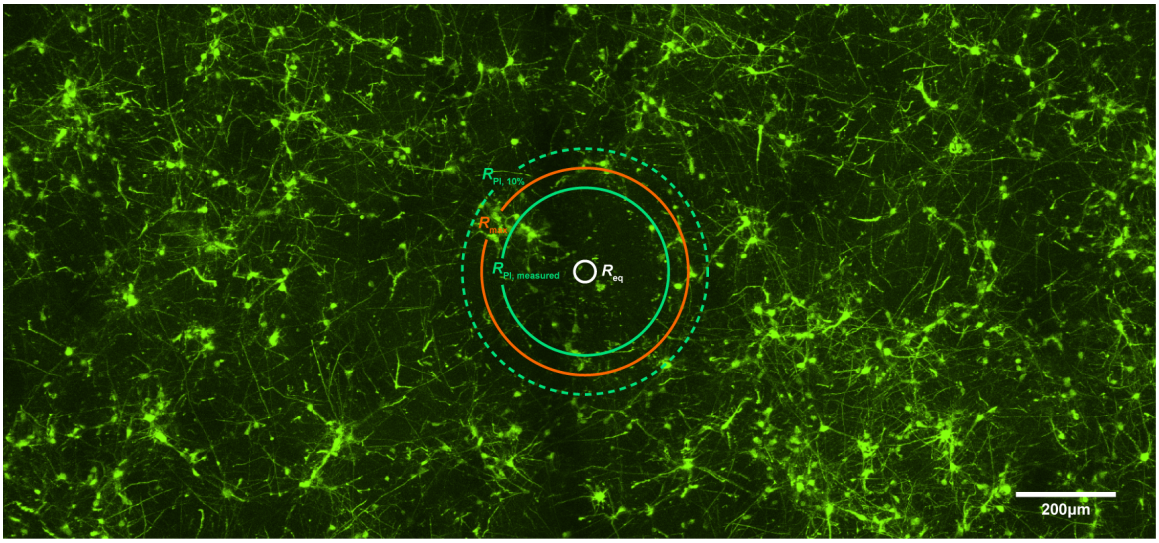

Figure 4.1: **Representative maximum intensity projection multiphoton micrographs of neural cell injurys in Matrigel-based 3D *in vitro* Culture.** Neural cells (Calcein AM; Green) are cultured in a 3D Matrigel-based (7.5 mg/mL) hydrogel cell culture platform. Cells undergo neurogenesis over the course of 7 days *in vitro* forming diverse interconnected networks.

interconnected networks as seen in Figure 4.1. Cells are deformed at high loading rates, following previously established protocols [25], using a single spatially-focused laser-induced inertial cavitation event. Inertial cavitation high-rate mechanical loading is characterized by multiple exponentially decaying oscillitory regimes of bubble expansion and collapse, which rapidly, and repeatedly deform the surrounding cells and material. Cavitation bubble dynamics are recorded using high-speed videography and are processed to segment the bubble radius as a function of time, consistent with previous work [25, 127].

The physical deformations induced by the inertial cavitation loading on neural cells embedded in the Matrigel substrate are quantified following the methodology described in detail in Chapter 3 Section 3.3. To reiterate briefly for the reader, the displacement of the cells and extracellular material surrounding the bubble is represented through a standard continuum mechanics representation utilizing the assumption of a spherically symmetric deformation field [25]. As such, the final quantification of the mechanical stretch of cells at different radial positions at the time of maximum bubble expansion is defined as,

$$\lambda_i \equiv \lambda^i_{\theta,\max} = \lambda_{\theta,\max}(r_0 = R_i) = \left[1 + \left(\frac{R_i}{R_{\max}}\right)^{-3} - \left(\frac{R_0/R_{\max}}{R_i/R_{\max}}\right)^3\right]^{1/3} \tag{4.1}$$

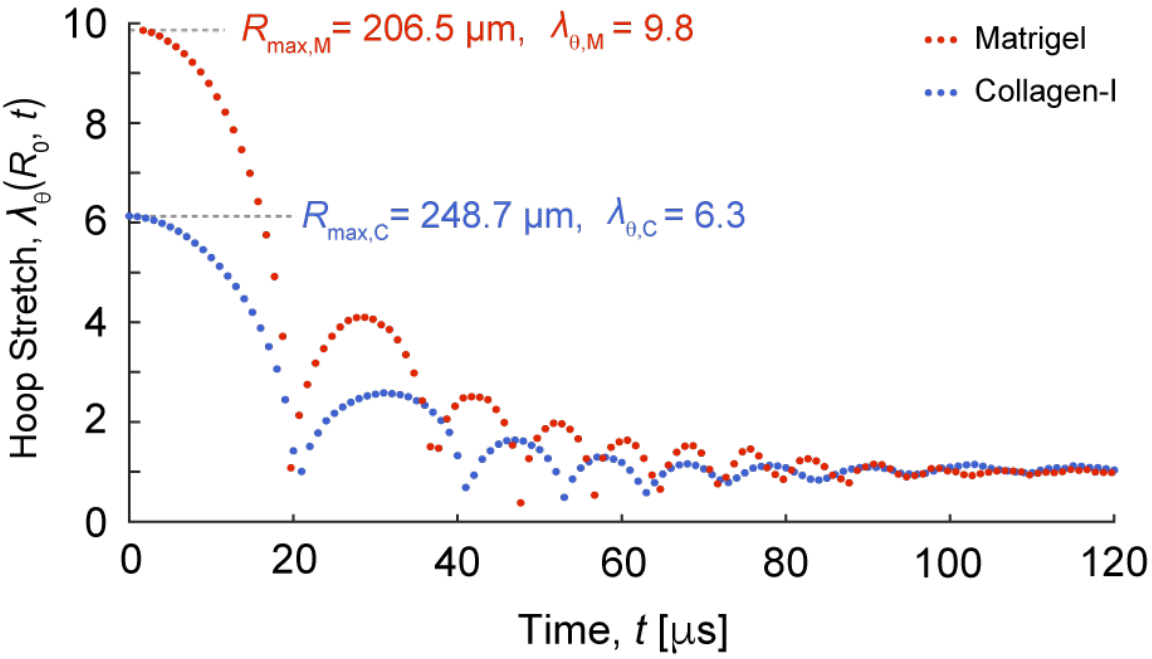

Figure 4.2: **Comparison of Representative Dynamics of Collagen-I and Matrigel Inertial Microcavitation Dynamics** Laser-induced inertial microcavitation events are generated through spatially-focused laser pulses. Cavitation dynamics in Matrigel (red dots) achieve a maximum critical stretch, $\lambda_{\theta,\mathrm{M}} = 9.8$ compared with a population average of $\lambda_{\theta,\mathrm{M}} = 8.83$ over $N = 6$. Collagen-I (blue dots) dynamics obtain a maximum maximum critical stretch, $\lambda_{\theta,\mathrm{C}} = 6.3$ as compared to the population average of $\lambda_{\theta,\mathrm{C}} = 7.40$ over $N = 234$

where R_i corresponds to the radial position of morphologically degenerate cellular features within each 3D image with respect to the equilibrium configuration (Figure 4.2).

Sample-to-sample comparisons of the maximum material and cellular stretches are assessed as the ratio of the radius of maximum bubble expansion, $R_{\max}$, to the quasi-stable equilibrium bubble radius, R_0, with the maximum material stretch defined as the ratio between them (Figure 4.3a; black). The effects of spherically symmetric deformations by the bubble on cellular populations can then assessed through a comparison of the pre- and post-cavitation live-cell images, from which a radius of primary injury, R_{PI}, is defined (Figure 4.3a; green). Initial results in the collagen-I hydrogel system (considered in detail in Chapter 3) across all sampled values for $R_{\max}$ show that the scaling between $R_{\max}$ and R_0 was determined to be highly linear (bisquare $R^2 = 0.971$) across a large distribution of maximum bubble radii with the median maximum bubble stretch ratio at the bubble wall given by $\Lambda_{\theta,\mathrm{C}} = R_{\max}/R_0 = 7.40$ Additionally, the primary injury radius-to-maximum bubble radius ratio, $a_{\mathrm{PI,C}} = R_{\mathrm{PI}}/R_{\max}$ was direct (bisquare $R^2 = 0.869$; $N = 219$) with median

$a^{50}_{\mathrm{PI,C}} = 0.969$.

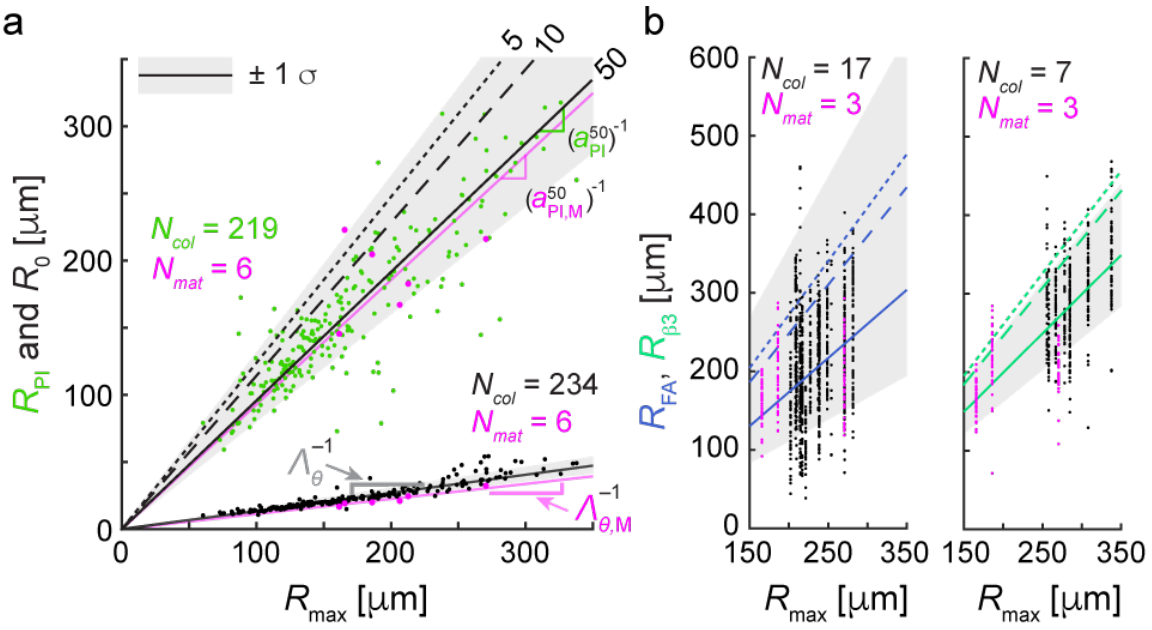

Figure 4.3: **Comparative analysis of R_{PI} and R_0 data for collagen-I and Matrigel hydrogel systems.** (a) In the collagen-I hydrogel system both the primary injury (PI, green, $N = 219$ experiments) and bubble equilibrium (black, $N = 234$) radii for each experiment scale linearly with maximum bubble radius, suggesting a constant and invariant critical strain value for primary mechanical injury. Matrigel primary injury data (Magenta, $N = 6$) falls within ± 1 standard deviation from the mean ratio of $R_{\max}$ to R_0 suggesting primary injury in matrigel is consistent with primary injury in collagen-I (b) For a subset of samples, points were manually segmented from volumes fluorescently labeled for f-actin (FA, royal blue; $n = 1003$ points over $N = 17$ volumes) and β3-tubulin (β3, spring green; $n = 390$, $N = 8$), converted into 3D radial measurements from the bubble center, and plotted versus the maximum bubble radius. A qualitative comparison of matrigel processed analogously for FA (magenta, $N = 3$, $n = 137$) and β3 (magenta, $N = 3$, $n = 126$) further show good agreement with trends from collagen-I data.

Comparatively, within the Matrigel-based hydrogel system the scaling between $R_{\max}$ and R_0 was additionally determined to be linear (bisquare $R^2 = 0.923$, $N = 6$) having a median maximum bubble stretch ratio at the wall given by $\Lambda_{\theta,\mathrm{M}} = R_{\max}/R_0 = 8.8261$. When $\Lambda_{\theta,\mathrm{M}}$ is compared to maximum stretch in collagen, the Matrigel data presents a unique population distinct from collagen with a bisquare value of only $R^2 = 0.254$ when considered with respect to the expected values from median maximum stretch value of $\Lambda_{\theta,\mathrm{C}} = 7.40$. The primary injury radius-to-maximum bubble radius ratio of Matrigel samples, $a_{\mathrm{PI,M}} = R_{\mathrm{PI}}/R_{\max}$ had a median value of $a^{50}_{\mathrm{PI,M}} = 0.946$ ($N = 6$), however, a bisquare value of $R^2 = -1.49$ suggests that additional data, across a wider range of $R_{\max}$ values, is required before robust injury tolerance thresholds can be drawn from Matrigel independently, as previously demonstrated with collagen-I samples. Qualitative comparisons of the relationship of R_{PI} to

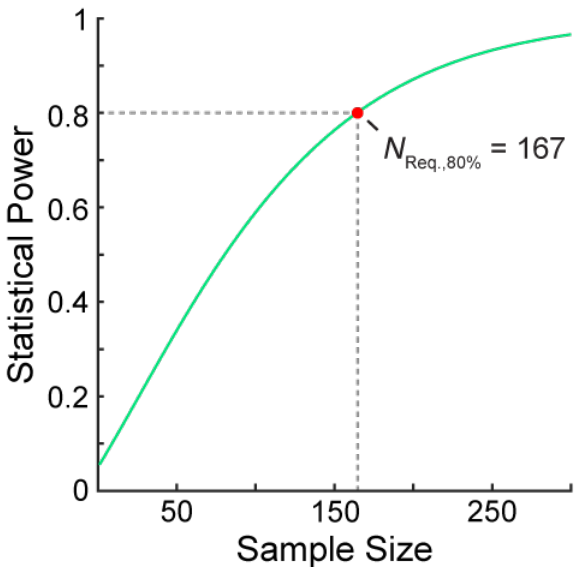

Figure 4.4: **Power Analysis for accurate distinction between Matrigel and Collagen-I R_{PI} data** Power analysis to determine the required sample size ($N = 167$) to correctly reject the null hypothesis with an 80% certainty using a students t-test when comparing Collagen-I and Matrigel populations of R_{PI} normalized by R_{max} with a mean value of 0.969, and standard deviation of 0.172 for Collagen-I and a mean of 1.01 for Matrigel. Null hypothesis: All data comes from the same population.

R_{max} for Matrigel (Figure 4.3a; pink dots) and for collagen-I (Figure 4.3a; green dots) show that the two populations are in general in good agreement, with all values for R_{PI} in the Matrigel system falling within ± 1 standard deviation from the mean for all collagen-I data (Figure4.3; grey shading). Further, power analysis (Figure 4.4) performed to determine the sample size required for a students t-test to provide an 80% confidence in disproving the null hypothesis that 'all data originates from the same population' is $N = 167$ individual samples. Power analysis was calculated using the mean and standard deviations from data in Chapter 3 and represents a significant increase in sample size over currently available data. Given the general good agreement between Matrigel and collagen-I R_{PI} data, and the predicted large sample size required to differentiate the populations, we can initially treat the primary mechanical injury phenomena as a single data set of $N = 225$ and recompute the stretch injury tolerance thresholds for the radius of primary injury for comparative purposes. As previously stated, and discussed further below, additional data is required in a more stable integrin-diverse experimental platform prior to the extension of injury threshold tolerances more than qualitatively. The stretch injury tolerance threshold for R_{PI} can be computed as in Chapter 3 equation 3.8 for the 50-th percentile. Prior to inclusion of the

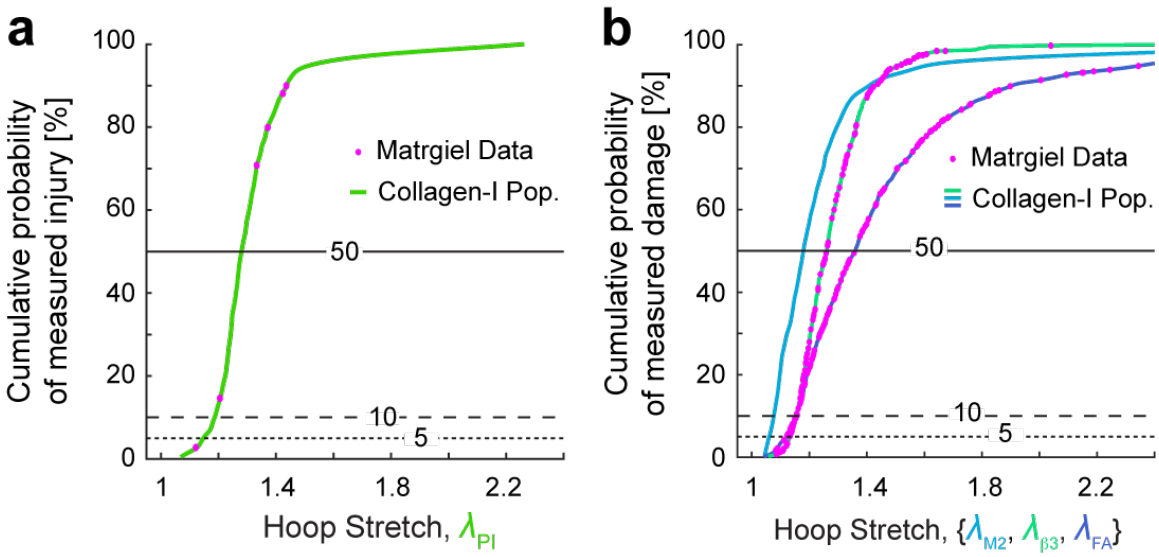

Figure 4.5: **Comparison of Matrigel stretch injury data to Collagen-I stretch injury population** (a) Cumulative probability curve for defining the stretch-based thresholds for (or inverse tolerance of) primary injury based on Calcein AM (50%, solid; 10%, dashed; 5%, dotted). (b) Cumulative probability curve for defining the stretch-based injury thresholds (or injury tolerance) for f-actin, β3-tubulin, and MAP2 (50%, solid; 10%, dashed; 5%, dotted). Matrigel data (pink dots) show good agreement with the previously computed thresholds from Collagen-I (solid lines) population data with the majority of matrigel injury markers occuring at greater than the previously reported 10-th percentile injury thresholds.

Matrigel data sets the median stretch tolerance threshold for the disruption of total cellular morphology was determined to be $\lambda_{\mathrm{PI}} = 1.287$. Following inclusion of the Matrigel data sets, the median remains un-changed and the standard deviation of the population shifts minorly from $\sigma = 0.1644$ to $\sigma = 0.1635$ indicating no appreciable shift in injury tolerance thresholds. Comparisons of the stretch injury tolerance data for matrigel (pink dots) and collagen-I (solid lines) hydrogel models can be seen highlighted in figure 4.5. Belaying the need to recalculate the tolerance thresholds determined in Chapter 3, and highlighted in table 3.3.

As with the qualitative comparison for R_{PI} performed for Matrigel and Collagen-I, a comparison of the spatial locations of morphologically degenerate cellular features (i.e., blunted projections) in Matrigel data sets can be completed. Matrigel post-cavitation samples immunlablled for f-actin and β3-tubulin are in good general agreement with trends observed in collagen-I data (Figure 4.3b, pink dots). Within Matrigel imunlabelled datasets, 62.1%

of blunted β3-tubulin projections, and 94.2% of blunted f-actin projections as fell within ± 1 standard deviation (σ) of the mean of collagen-I data. Due to spatial fidelity concerns associated with the incompatibility of preliminary data with the full analysis pipelines employed in Chapter 3, stretch and strain tolerance thresholds cannot be confidently recomputed with the inclusion of Matrigel immunolabelled projection damage data at this time. This is due in part to the rapid change in mechanical stretch as a function of radial distance from the bubble wall ($\sim 1/\mathrm{r}^3$), as a direct implication of the deformation field relatively small shifts in radial position represent potentially large changes to computed stretch and strain tolerance thresholds.

Experimental and analytical issues with preliminary data presented in this chapter can be attributed to heterogeneity within the Matrigel-based hydrogel platform. Matrigel is a commonly employed substrate for the culture of neural cellular populations, and consists of a mixture of reconstituted basement membrane proteins and growth factors that support healthy cell cultures [6, 78]. According to manufacturer specifications for the composition of Matrigel a resultant mixture consists of approximately ~60% Laminin, 30% collagen IV, and roughly 8% entactin (Dow Corning, Tewksbury, MA). Unfortunately, a known limitation of the isolation method used to obtain Matrigel limits lot-to-lot consistency of these components. Structurally, Collagen IV and Laminin, are interconnected in the matrigel platform through associations with entactin, and various proteoglycans. This imparts an unavoidable local concentration dependence on the availability of proteins in solution resulting in local heterogeneity at the protein level. This local heterogeneity is evidenced by the higher frequency of asymmetric bubble dynamics observed in preliminary experiments ($> 75\%$), as compared to similar fibrillar hydrogel systems like collagen-I where ~30% of samples behave asymmetrically. Examinations of matrix architecture of relevant concentrations of collagen-I and Matrigel, performed with scanning electron microscopy indicate that Matrigel exists as a more heterogeneous structure than 2 mg/mL collagen-I fibirillar hydrogels, as seen in figure 4.6 adapted from van Goeller et al., 2010 [181]. The observed Matrigel architecture exists as a more tightly packed mesh of short interconnected fibers with more spatially-variant density when compared to collagen-I hydrogels. As axisymmetric bubble

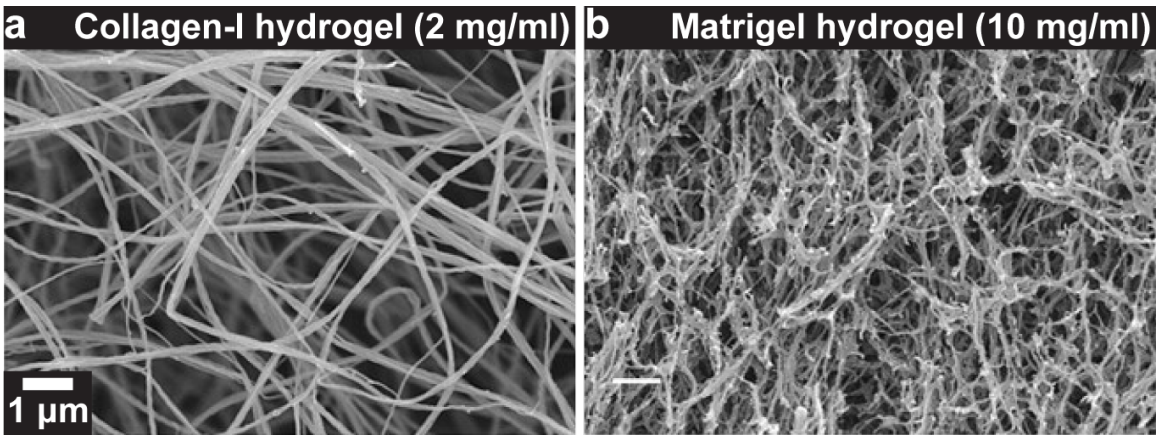

Figure 4.6: **Scanning electron microscopy (SEM) comparison of matrigel and collagen-I microscale architecture** (a) scanning electron micrograph of 2 mg/mL collagen-I hydrogel fibrillar architecture. (b) scanning electron micrograph of 10 mg/mL Matrigel microscale architecture; scale bar 1 μm. Adapted from van Goeller et al., 2010 [181]

dynamics can be attributed to non-uniform pressure differentials across the bubble wall, and can be driven through differences local material properties or densities in the bubble surroundings, Matrigel 3D hydrogels are a difficult candidate for continued cavitation-based injury experimentation.

The intention of a system design utilizing the incorporation of Matrigel for 3D *in vitro* cell culture of neural cells was successfully demonstrated in this initial work. By providing the neural cell populations a more diverse extracellular protein culture substrate, cells were demonstrated to be able to successfully deformed under high loading rates through more complex integrin associations to the extracellular environment. Through the incorporation of Matrigel into the experimental model, integrin interactions were extended to include $\alpha1\beta1$, $\alpha3\beta1$, $\alpha6\beta1$, $\alpha7\beta1$, and $\alpha3\beta5$ on laminin and collagen IV proteins [73, 131]. Cells were additionally afforded the ability to interact with the cellular environment through various non-integrin associations including those of the IgCAM family of extracellular space connection proteins [57,120]. Despite this more diverse extracellular association, initial work presented in this chapter indicates that the primary mechanical injury event does not appear to be highly dependent on the specific extracellular associations maintained by neural cells, though additional work is necessary to fully quantify this phenomenon.

Future work to validate these initial findings should incorporate employ a diverse integrin microenvironment capable of providing consistent and reproducible strains to more faithfully recapitulate the response of neural cells to high-rate mechanical loading in an experimentally feasible mechanical platform. Improvements to the experimental design are required to improve the feasibility of attaining larger sample sizes in an efficient manner. These improvements should aim to mitigate the local heterogeneity of material properties presented by the native Matrigel-based 3D *in vitro* hydrogel models. Potential avenues for improvement of the experimental platform include embedding Matrigel at the desired concentration (7.5 mg/mL) within more structurally uniform microenvironments capable of supporting cell culture. Generating interpenetrating networks of differing extracellular components has been shown to allow for tuneable microstructures and material properties as has been successfully demonstrated in Alginate/Collagen-I interpenetrating networks [182]. Additional work should then be completed to ensure that the model behaves in a reproducible mechanical fashion under high rate loading without significant, long timescale, viscoelastic material behavior, or plastic deformations. These improvements will allow a more integrin diverse culture platform allow to provide consistent data acquisition aligned with existing data processing procedures.

Chapter 5

Conclusions and Future Work

5.1 Summary

The aim of this thesis was to quantify injury tolerance metrics for the high-rate mechanical failure, or primary cellular injury, of neural cells through integrin-based adhesion to the extracellular space. Chapter 1 provides an introduction to the rate dependency of Traumatic Brain Injuries (TBI), and provides detailed examination of our current understanding of the superstructural and cytoskeletal organization of the neuron. This examination aims to inform the reader on how TBIs are experienced at the cellular scale and act as a primer on key biological concepts necessary to fully appreciate the biomechanics of cellular injury as in work presented in Chapter 3, as well as the importance of consideration of extracellular interactions presented in Chapter 4. Chapter 2 explores the isolation of high-viability primary neural cells from the corticies of Sprague-Dawley rat pups and presents a means of generating 3D collagen-I hydrogel-based cell culture platforms for the extended culture of primary cortical cells *in vitro* [56]. Additionally, a methodology and experimental platform for the administration of spatially-localized high strain rate mechanical deformations through the deposition of laser-induced inertial microcavitation events is introduced [15, 25, 127]. Finally, a detailed examination of immunohistochemical techniques within the context of large (several mm^3) hydrogel constructs is described. In Chapter 3 the first ever quantitative mechanical injury tolerance thresholds for neural cells at strain rates of $\mathcal{O}(10^3 - 10^8)1/s$

are presented. Specifically, 3D collagen-I *in vitro* cell cultures are mechanically deformed at high loading rates using spatially-focused laser induced inertial cavitation events in order to apply spherically symmetric deformation fields to neural cellular populations in 3D hydrogels. Fluorescent live- and fixed-cell imaging is performed to delineate the stretch, strain, and stress values required to mechanically disrupt cellular projections and total cell morphology. In Chapter 4, the high rate injury pathology of neural cells are examined in a cell culture model designed to present a more diverse battery of biological connections to cellular microenvironment as compared to work in Chapter 3. Work in this chapter qualitatively validates the continued exploration of more diverse integrin microenvironments by extending previously established methodologies into a Matrigel-based 3D *in vitro* cell culture platform. This work will require additional experimental platform improvements to provide quantitative confirmation of the experimental results presented showing good general agreement with the thresholds and trends discussed in Chapter 3.

5.2 Recommendations for Future Work

This thesis discusses and develops the first high-rate mechanical injury tolerance thresholds for total disruption of neural cellular morphology and the disruption of neural cellular projections containing filamentous actin, β3-tubulin, and microtubule associated protein-2. Many avenues of continued exploration are available and necessary to translate these results from the innate limitations of *in vitro* systems to more physiologically relevant experimental platforms and to inform modeling efforts aimed at mitigating Traumatic Brain Injuries.

The thresholds dileneated in this thesis are limited to the purely mechanical injury of neural cellular populations and the disruption of neural cellular projections in a 3D *in vitro* collagen-I based cell culture model. One limitation of the cell culture platform utilized in this work is dependence of cellular connection to the microenviroment being limited to two integrin subtypes. An extension of this technique could include a more integrin-diverse culture platforms (as with Matrigel in Chapter 4), or additionally high-cell density culture platforms where cadherin-based interactions to the extracellular space are prevalent.

This extension of the technique is necessary to ensure that the assumption that the injury tolerance thresholds are not dependent on the specific extracellular connection but instead the mechanical deformations themselves remains valid.

An additional limitation of the work presented in this thesis is that thresholds presented are a result of purely mechanical degradation of the cells. The secondary, or time-based, biochemical activation of cell death and degradation pathways are not conducted here. An important and experimentally demanding extension of this work is the inclusion of secondary injury pathway examination following mechanical loading. It remains unknown whether cells distal to the cavitation epicenter which experience loading below the thresholds required for cellular injury experience a biochemically-dependent injury pathology such as those seen in lower rate injury models using this culture platform [4, 26]. An experimentally straightforward approach to beginning this work would straightforwardly examine downstream activation of cell-death, and DNA damage pathway markers such as executioner caspases 3 & 7, as well as proteins upregulated in response to DNA damage such as protein p53.

Further, at present the specific pathway activation that results in the downstream activation of cellular death pathways in neural cells following mechanical deformations remains unknown [120]. As mechanotransduction is biologically diverse and dependent on both the type and magnitude of mechanical force applied to the cell this experimental platform provides an excellent platform for the evaluation of biochemical injury. This injury platform provides a mechanically feasible way to examine injury-specific pathway biology dependent on mechanotransduction. Cells in this platform $\sim$2 times the maximum bubble radius away from the epicenter of the cavitation event remain physically undeformed and morphologically in-tact. This allows for the examination of an in-sample mechanical injury control with which to examine the activation of purely chemically-induced biochemical pathway activation. Such examinations could include, chemically-induced kinase activity, astroglial activation and recruitment, among others.

The cavitation injury platform is solely dependent on optical transparency to deliver the spatially-focused laser energy required to nucleate cavitation and to facilitate the acquisition of high speed videography. In this way, a wide variety of culture platforms are compatible

with the deformation of cells in this way. By modifying the type of extracellular material, and subsequently the type of extracellular connection the cells maintain, mechanotransduction pathway activation through specific focal adhesions can be examined. These examinations, however, do require that the extracellular material is capable of allowing for the completion of neurogenesis and allows for sufficient nutrient diffusion from culture media as to maintain cellular viability throughout the culture period.

Bibliography

[1] S. T. DeKosky, M. D. Ikonomovic, and S. Gandy, "Traumatic Brain Injury — Football, Warfare, and Long-Term Effects," *New England Journal of Medicine*, vol. 363, pp. 1293–1296, Sept. 2010.

[2] M. C. Dewan, A. Rattani, S. Gupta, R. E. Baticulon, Y.-C. Hung, M. Punchak, A. Agrawal, A. O. Adeleye, M. G. Shrime, A. M. Rubiano, J. V. Rosenfeld, and K. B. Park, "Estimating the global incidence of traumatic brain injury," *Journal of Neurosurgery*, vol. 130, pp. 1080–1097, Apr. 2019.

[3] S. Parikh, M. Koch, and R. K. Narayan, "Traumatic Brain Injury," *International Anesthesiology Clinics*, vol. 45, no. 3, pp. 119–135, 2007.

[4] E. Bar-Kochba, M. T. Scimone, J. B. Estrada, and C. Franck, "Strain and rate-dependent neuronal injury in a 3D in vitro compression model of traumatic brain injury," *Scientific Reports*, vol. 6, p. 30550, Aug. 2016.

[5] D. K. Cullen and M. C. LaPlaca, "Neuronal Response to High Rate Shear Deformation Depends on Heterogeneity of the Local Strain Field," *Journal of Neurotrauma*, vol. 23, pp. 1304–1319, Sept. 2006.

[6] D. K. Cullen, V. N. Vernekar, and M. C. LaPlaca, "Trauma-Induced Plasmalemma Disruptions in Three-Dimensional Neural Cultures Are Dependent on Strain Modality and Rate," *Journal of Neurotrauma*, vol. 28, pp. 2219–2233, Nov. 2011.

[7] D. M. Geddes-Klein, K. B. Schiffman, and D. F. Meaney, "Mechanisms and Consequences of Neuronal Stretch Injury *In Vitro* Differ with the Model of Trauma," *Journal of Neurotrauma*, vol. 23, pp. 193–204, Feb. 2006.

[8] B. E. Dabiri, "An In Vitro Model of Traumatic Brain Injury (TBI)," p. 37.

[9] S. Haniff and P. A. Taylor, "In silico investigation of blast-induced intracranial fluid cavitation as it potentially leads to traumatic brain injury," *Shock Waves*, vol. 27, pp. 929–945, Nov. 2017.

[10] M. K. Nyein, A. M. Jason, L. Yu, C. M. Pita, J. D. Joannopoulos, D. F. Moore, and R. A. Radovitzky, "In silico investigation of intracranial blast mitigation with relevance to military traumatic brain injury," *Proceedings of the National Academy of Sciences*, vol. 107, pp. 20703–20708, Nov. 2010.

[11] R. W. Carlsen, A. L. Fawzi, Y. Wan, H. Kesari, and C. Franck, "A quantitative relationship between rotational head kinematics and brain tissue strain from a 2-D parametric finite element analysis," *Brain Multiphysics*, vol. 2, p. 100024, 2021.

[12] R. M. Wright, A. Post, B. Hoshizaki, and K. T. Ramesh, "A Multiscale Computational Approach to Estimating Axonal Damage under Inertial Loading of the Head," *Journal of Neurotrauma*, vol. 30, pp. 102–118, Jan. 2013.

[13] M. T. Scimone, H. C. Cramer, P. Hopkins, J. B. Estrada, and C. Franck, "Application of mild hypothermia successfully mitigates neural injury in a 3D in-vitro model of traumatic brain injury," *PLOS ONE*, vol. 15, p. e0229520, Apr. 2020.

[14] A. F. Bower, *Applied Mechanics of Solids*. Boca Raton: CRC Press, 2010.

[15] J. Yang, H. C. Cramer, and C. Franck, "Extracting non-linear viscoelastic material properties from violently-collapsing cavitation bubbles," *Extreme Mechanics Letters*, vol. 39, p. 100839, Sept. 2020.

[16] S. Haniff and P. A. Taylor, "In silico investigation of blast-induced intracranial fluid cavitation as it potentially leads to traumatic brain injury," *Shock Waves*, vol. 27, pp. 929–945, Nov. 2017.

[17] S. Haniff, P. Taylor, A. Brundage, D. Burnett, C. Cooper, A. Gullerud, and R. Terpsma, "Virtual Simulation of the Effects of Intracranial Fluid Cavitation in Blast-Induced Traumatic Brain Injury," in *Volume 3: Biomedical and Biotechnology Engineering*, (Houston, Texas, USA), p. V003T03A062, American Society of Mechanical Engineers, Nov. 2015.

[18] S. B. Shively, I. Horkayne-Szakaly, R. V. Jones, J. P. Kelly, R. C. Armstrong, and D. P. Perl, "Characterisation of interface astroglial scarring in the human brain after blast exposure: A post-mortem case series," *The Lancet Neurology*, vol. 15, pp. 944–953, Aug. 2016.

[19] D. H. Smith, V. E. Johnson, and W. Stewart, "Chronic neuropathologies of single and repetitive TBI: Substrates of dementia?," *Nature Reviews Neurology*, vol. 9, pp. 211–221, Apr. 2013.

[20] D. H. Smith, D. F. Meaney, and W. H. Shull, "Diffuse Axonal Injury in Head Trauma:," *Journal of Head Trauma Rehabilitation*, vol. 18, pp. 307–316, July 2003.

[21] C. A. Tagge, A. M. Fisher, O. V. Minaeva, A. Gaudreau-Balderrama, J. A. Moncaster, X.-L. Zhang, M. W. Wojnarowicz, N. Casey, H. Lu, O. N. Kokiko-Cochran, S. Saman, M. Ericsson, K. D. Onos, R. Veksler, V. V. Senatorov, A. Kondo, X. Z. Zhou, O. Miry, L. R. Vose, K. R. Gopaul, C. Upreti, C. J. Nowinski, R. C. Cantu, V. E. Alvarez, A. M. Hildebrandt, E. S. Franz, J. Konrad, J. A. Hamilton, N. Hua, Y. Tripodis, A. T. Anderson, G. R. Howell, D. Kaufer, G. F. Hall, K. P. Lu, R. M. Ransohoff, R. O. Cleveland, N. W. Kowall, T. D. Stein, B. T. Lamb, B. R. Huber, W. C. Moss, A. Friedman, P. K. Stanton, A. C. McKee, and L. E. Goldstein, "Concussion, microvascular injury, and early tauopathy in young athletes after impact head injury and an impact concussion mouse model," *Brain*, vol. 141, pp. 422–458, Feb. 2018.

[22] J. T. Weber, "Experimental models of repetitive brain injuries," in *Progress in Brain Research*, vol. 161, pp. 253–261, Elsevier, 2007.

[23] "Consensus Recommendations for the Postmortem Diagnosis of Alzheimer's Disease," *Neurobiology of Aging*, vol. 18, pp. S1–S2, July 1997.

[24] S. B. Shively, I. Horkayne-Szakaly, R. V. Jones, J. P. Kelly, R. C. Armstrong, and D. P. Perl, "Characterisation of interface astroglial scarring in the human brain after blast exposure: A post-mortem case series," *The Lancet. Neurology*, vol. 15, pp. 944–953, Aug. 2016.

[25] J. B. Estrada, H. C. Cramer, M. T. Scimone, S. Buyukozturk, and C. Franck, "Neural cell injury pathology due to high-rate mechanical loading," *Brain Multiphysics*, vol. 2, p. 100034, 2021.

[26] M. T. Scimone, H. C. Cramer, P. Hopkins, J. B. Estrada, and C. Franck, "Application of mild hypothermia successfully mitigates neural injury in a 3D in-vitro model of traumatic brain injury," *PLOS ONE*, vol. 15, p. e0229520, Apr. 2020.

[27] I. Cernak and L. J. Noble-Haeusslein, "Traumatic Brain Injury: An Overview of Pathobiology with Emphasis on Military Populations," *Journal of Cerebral Blood Flow & Metabolism*, vol. 30, pp. 255–266, Feb. 2010.

[28] D. F. Meaney, B. Morrison, and C. Dale Bass, "The Mechanics of Traumatic Brain Injury: A Review of What We Know and What We Need to Know for Reducing Its Societal Burden," *Journal of Biomechanical Engineering*, vol. 136, p. 021008, Feb. 2014.

[29] A. Kondo, K. Shahpasand, R. Mannix, J. Qiu, J. Moncaster, C.-H. Chen, Y. Yao, Y.-M. Lin, J. A. Driver, Y. Sun, S. Wei, M.-L. Luo, O. Albayram, P. Huang, A. Rotenberg, A. Ryo, L. E. Goldstein, A. Pascual-Leone, A. C. McKee, W. Meehan, X. Z. Zhou, and K. P. Lu, "Antibody against early driver of neurodegeneration cis P-tau blocks brain injury and tauopathy," *Nature*, vol. 523, pp. 431–436, July 2015.

[30] A. J. Moszczynski, W. Strong, K. Xu, A. McKee, A. Brown, and M. J. Strong, "Pathologic Thr ^{175} tau phosphorylation in CTE and CTE with ALS," *Neurology*, vol. 90, pp. e380–e387, Jan. 2018.

[31] I. Cernak, Z. Wang, J. Jiang, X. Bian, and J. Savic, "Cognitive deficits following blast injury-induced neurotrauma: Possible involvement of nitric oxide," *Brain Injury*, vol. 15, pp. 593–612, July 2001.

[32] T. L. Tanielian and L. Jaycox, *Invisible Wounds of War: Psychological and Cognitive Injuries, Their Consequences, and Services to Assist Recovery.* Santa Monica, CA: RAND, 2008.

[33] G. B. Effgen, E. W. Vogel, K. A. Lynch, A. Lobel, C. D. Hue, D. F. Meaney, C. R. D. Bass, and B. Morrison, "Isolated Primary Blast Alters Neuronal Function with Minimal Cell Death in Organotypic Hippocampal Slice Cultures," *Journal of Neurotrauma*, vol. 31, pp. 1202–1210, July 2014.

[34] R. Mejía-Alvarez, J. Kerwin, S. Vidhate, P. Sandherr, E. Patton, B. Dávila-Montero, A. Yucesoy, and A. Willis, "Large cross-section blast chamber: Design and experimental characterization," *Measurement Science and Technology*, vol. 32, p. 115902, Nov. 2021.

[35] G. B. Effgen, C. D. Hue, E. Vogel, M. B. Panzer, D. F. Meaney, C. R. Bass, and B. Morrison, "A Multiscale Approach to Blast Neurotrauma Modeling: Part II: Methodology for Inducing Blast Injury to in vitro Models," *Frontiers in Neurology*, vol. 3, 2012.

[36] K. R. Hansen, G. J. DeWalt, A. I. Mohammed, H.-a. Tseng, M. E. Abdulkerim, S. Bensussen, V. Saligrama, B. Nazer, W. D. Eldred, and X. Han, "Mild Blast Injury Produces Acute Changes in Basal Intracellular Calcium Levels and Activity Patterns in Mouse Hippocampal Neurons," *Journal of Neurotrauma*, vol. 35, pp. 1523–1536, July 2018.

[37] C. E. Brennen, "CAVITATION IN BIOLOGICAL AND BIOENGINEERING CONTEXTS," p. 9.

[38] R. L. Swanson, S. Hampton, J. Green-McKenzie, R. Diaz-Arrastia, M. S. Grady, R. Verma, R. Biester, D. Duda, R. L. Wolf, and D. H. Smith, "Neurological Manifestations Among US Government Personnel Reporting Directional Audible and Sensory Phenomena in Havana, Cuba," *JAMA*, vol. 319, p. 1125, Mar. 2018.

[39] A. M. Dagro, J. W. Wilkerson, T. P. Thomas, B. T. Kalinosky, and J. A. Payne, "Computational modeling investigation of pulsed high peak power microwaves and the potential for traumatic brain injury," *Science Advances*, vol. 7, p. eabd8405, Oct. 2021.

[40] D. O'Donohue, "Joint Electromagnetic Spectrum Operations," No. JP 3-85, May 2020.

[41] D. L. Miller and R. M. Thomas, "Ultrasound contrast agents nucleate inertial cavitation in vitro," *Ultrasound in Medicine & Biology*, vol. 21, pp. 1059–1065, Jan. 1995.

[42] M. W. Miller, D. L. Miller, and A. A. Brayman, "A review of in vitro bioeffects of inertial ultrasonic cavitation from a mechanistic perspective," *Ultrasound in Medicine & Biology*, vol. 22, pp. 1131–1154, Jan. 1996.

[43] C. C. Church, "Spontaneous homogeneous nucleation, inertial cavitation and the safety of diagnostic ultrasound," *Ultrasound in Medicine & Biology*, vol. 28, pp. 1349–1364, Oct. 2002.

[44] M. Trendowski, "The promise of sonodynamic therapy," *Cancer and Metastasis Reviews*, vol. 33, pp. 143–160, Mar. 2014.

[45] C. C. Church, "A theoretical study of cavitation generated by an extracorporeal shock wave lithotripter," *The Journal of the Acoustical Society of America*, vol. 86, pp. 215–227, July 1989.

[46] Z. Xu, Z. Fan, T. L. Hall, F. Winterroth, J. B. Fowlkes, and C. A. Cain, "Size Measurement of Tissue Debris Particles Generated from Pulsed Ultrasound Cavitational Therapy – Histotripsy," *Ultrasound in Medicine & Biology*, vol. 35, pp. 245–255, Feb. 2009.

[47] A. D. Maxwell, C. A. Cain, A. P. Duryea, L. Yuan, H. S. Gurm, and Z. Xu, "Non-invasive Thrombolysis Using Pulsed Ultrasound Cavitation Therapy – Histotripsy," *Ultrasound in Medicine & Biology*, vol. 35, pp. 1982–1994, Dec. 2009.

[48] V. Venugopalan, A. Guerra, K. Nahen, and A. Vogel, "Role of Laser-Induced Plasma Formation in Pulsed Cellular Microsurgery and Micromanipulation," *Physical Review Letters*, vol. 88, p. 078103, Feb. 2002.

[49] A. V. Cherian and K. R. Rau, "Pulsed-laser-induced damage in rat corneas: Time-resolved imaging of physical effects and acute biological response," *Journal of Biomedical Optics*, vol. 13, no. 2, p. 024009, 2008.

[50] J. J. Macoskey, S. W. Choi, T. L. Hall, E. Vlaisavljevich, J. E. Lundt, F. T. Lee, E. Johnsen, C. A. Cain, and Z. Xu, "Using the cavitation collapse time to indicate the extent of histotripsy-induced tissue fractionation," *Physics in Medicine & Biology*, vol. 63, p. 055013, Mar. 2018.

[51] J. R. Sukovich, C. A. Cain, A. S. Pandey, N. Chaudhary, S. Camelo-Piragua, S. P. Allen, T. L. Hall, J. Snell, Z. Xu, J. M. Cannata, D. Teofilovic, J. A. Bertolina, N. Kassell, and Z. Xu, "In vivo histotripsy brain treatment," *Journal of Neurosurgery*, vol. 131, pp. 1331–1338, Oct. 2019.

[52] A. Adnan, S. Qidwai, and A. Bagchi, "Viscoelastic Response of Microtubule—Tau Proteins Assembly During Axonal Stretch: Combined Atomistic and Continuum Predictions," p. 10.

[53] H. Ahmadzadeh, D. H. Smith, and V. B. Shenoy, "Viscoelasticity of Tau Proteins Leads to Strain Rate-Dependent Breaking of Microtubules during Axonal Stretch Injury: Predictions from a Mathematical Model," *Biophysical Journal*, vol. 106, pp. 1123–1133, Mar. 2014.

[54] M. C. LaPlaca and L. E. Thibault, "Dynamic mechanical deformation of neurons triggers an acute calcium response and cell injury involving the N-methyl-D-aspartate glutamate receptor," p. 10.

[55] J. S. Sadick, M. E. Boutin, D. Hoffman-Kim, and E. M. Darling, "Protein characterization of intracellular target-sorted, formalin-fixed cell subpopulations," *Scientific Reports*, vol. 6, p. 33999, Sept. 2016.

[56] M. T. Scimone, H. C. Cramer III, E. Bar-Kochba, R. Amezcua, J. B. Estrada, and C. Franck, "Modular approach for resolving and mapping complex neural and other cellular structures and their associated deformation fields in three dimensions," *Nature Protocols*, vol. 13, pp. 3042–3064, Dec. 2018.

[57] S. T. Brady, G. J. Siegel, R. W. Albers, D. L. Price, and J. Benjamins, eds., *Basic Neurochemistry: Principles of Molecular, Cellular, and Medical Neurobiology*. Amsterdam ; Boston: Elsevier/Academic Press, 8th ed ed., 2012.

[58] M. J. Aminoff and R. B. Daroff, eds., *Encyclopedia of the Neurological Sciences*. Amsterdam ; Boston: Academic Press, 1st ed ed., 2003.

[59] M. Ludwig, D. Apps, J. Menzies, J. C. Patel, and M. E. Rice, "Dendritic Release of Neurotransmitters," *Comprehensive Physiology*, vol. 7, pp. 235–252, Dec. 2016.

[60] A. J. Koleske, "Molecular mechanisms of dendrite stability," *Nature Reviews Neuroscience*, vol. 14, pp. 536–550, Aug. 2013.

[61] C. Conde and A. Cáceres, "Microtubule assembly, organization and dynamics in axons and dendrites," *Nature Reviews Neuroscience*, vol. 10, pp. 319–332, May 2009.

[62] J. Al-Bassam, R. S. Ozer, D. Safer, S. Halpain, and R. A. Milligan, "MAP2 and tau bind longitudinally along the outer ridges of microtubule protofilaments," *Journal of Cell Biology*, vol. 157, pp. 1187–1196, June 2002.

[63] L. C. Kapitein and C. C. Hoogenraad, "Building the Neuronal Microtubule Cytoskeleton," *Neuron*, vol. 87, pp. 492–506, Aug. 2015.

[64] K. Xu, G. Zhong, and X. Zhuang, "Actin, Spectrin, and Associated Proteins Form a Periodic Cytoskeletal Structure in Axons," *Science*, vol. 339, pp. 452–456, Jan. 2013.

[65] R. Mohan and A. John, "Microtubule-associated proteins as direct crosslinkers of actin filaments and microtubules: ROLE OF MAPs IN THE ACTIN-MICROTUBULE NETWORK," *IUBMB Life*, vol. 67, pp. 395–403, June 2015.

[66] P. C. Georges, N. M. Hadzimichalis, E. S. Sweet, and B. L. Firestein, "The Yin–Yang of Dendrite Morphology: Unity of Actin and Microtubules," *Molecular Neurobiology*, vol. 38, pp. 270–284, Dec. 2008.

[67] F. Korobova and T. Svitkina, "Molecular Architecture of Synaptic Actin Cytoskeleton in Hippocampal Neurons Reveals a Mechanism of Dendritic Spine Morphogenesis," *Molecular Biology of the Cell*, vol. 21, pp. 165–176, Jan. 2010.

[68] A. Yuan, M. V. Rao, Veeranna, and R. A. Nixon, "Neurofilaments at a glance," *Journal of Cell Science*, vol. 125, pp. 3257–3263, July 2012.

[69] M. K. Lee and D. W. Cleveland, "Neurofilament function and dysfunction: Involvement in axonal growth and neuronal disease," *Current Opinion in Cell Biology*, vol. 6, pp. 34–40, Feb. 1994.

[70] N. Hirokawa, M. A. Glicksman, and M. B. Willard, "Organization of mammalian neurofilament polypeptides within the neuronal cytoskeleton.," *Journal of Cell Biology*, vol. 98, pp. 1523–1536, Apr. 1984.

[71] A. R. Costa, R. Pinto-Costa, S. C. Sousa, and M. M. Sousa, "The Regulation of Axon Diameter: From Axonal Circumferential Contractility to Activity-Dependent Axon Swelling," *Frontiers in Molecular Neuroscience*, vol. 11, p. 319, Sept. 2018.

[72] A. Yuan, H. Sershen, Veeranna, B. S. Basavarajappa, A. Kumar, A. Hashim, M. Berg, J.-H. Lee, Y. Sato, M. V. Rao, P. S. Mohan, V. Dyakin, J.-P. Julien, V. M.-Y. Lee, and R. A. Nixon, "Neurofilament subunits are integral components of synapses and modulate neurotransmission and behavior in vivo," *Molecular Psychiatry*, vol. 20, pp. 986–994, Aug. 2015.

[73] J. D. Humphries, A. Byron, and M. J. Humphries, "Integrin ligands at a glance," *Journal of Cell Science*, vol. 119, pp. 3901–3903, Oct. 2006.

[74] R. Zaidel-Bar, "Cadherin adhesome at a glance," *Journal of Cell Science*, vol. 126, pp. 373–378, Jan. 2013.

[75] M. A. Hemphill, S. Dauth, C. J. Yu, B. E. Dabiri, and K. K. Parker, "Traumatic Brain Injury and the Neuronal Microenvironment: A Potential Role for Neuropathological Mechanotransduction," *Neuron*, vol. 85, pp. 1177–1192, Mar. 2015.

[76] S. Yonemura, "Cadherin–actin interactions at adherens junctions," *Current Opinion in Cell Biology*, vol. 23, pp. 515–522, Oct. 2011.

[77] S. Huveneers and J. de Rooij, "Mechanosensitive systems at the cadherin–F-actin interface," *Journal of Cell Science*, vol. 126, pp. 403–413, Jan. 2013.

[78] M. C. LaPlaca, V. N. Vernekar, J. T. Shoemaker, and D. K. Cullen, "Three-Dimensional Neuronal Cultures," p. 19.

[79] E. A. Evans and D. A. Calderwood, "Forces and Bond Dynamics in Cell Adhesion," *Science*, vol. 316, pp. 1148–1153, May 2007.

[80] E. Puklin-Faucher and M. P. Sheetz, "The mechanical integrin cycle," *Journal of Cell Science*, p. 9.

[81] Y. Lad, D. S. Harburger, and D. A. Calderwood, "Integrin Cytoskeletal Interactions," in *Methods in Enzymology*, vol. 426, pp. 69–84, Elsevier, 2007.

[82] E. Syková and C. Nicholson, "Diffusion in brain extracellular space," *Physiological Reviews*, vol. 88, pp. 1277–1340, Oct. 2008.

[83] C. Nicholson and E. Syková, "Extracellular space structure revealed by diffusion analysis," *Trends in Neurosciences*, vol. 21, pp. 207–215, May 1998.

[84] D. Bonneh-Barkay and C. A. Wiley, "Brain Extracellular Matrix in Neurodegeneration," *Brain Pathology*, vol. 19, pp. 573–585, Oct. 2009.

[85] L. W. Lau, R. Cua, M. B. Keough, S. Haylock-Jacobs, and V. W. Yong, "Pathophysiology of the brain extracellular matrix: A new target for remyelination," *Nature Reviews Neuroscience*, vol. 14, pp. 722–729, Oct. 2013.

[86] R. S. Schmid, "Role of Integrins in the Development of the Cerebral Cortex," *Cerebral Cortex*, vol. 13, pp. 219–224, Mar. 2003.

[87] J. D. Parkin, J. D. San Antonio, V. Pedchenko, B. Hudson, S. T. Jensen, and J. Savige, "Mapping structural landmarks, ligand binding sites, and missense mutations to the collagen IV heterotrimers predicts major functional domains, novel interactions, and variation in phenotypes in inherited diseases affecting basement membranes," *Human Mutation*, vol. 32, pp. 127–143, Feb. 2011.

[88] R. Zaidel-Bar and B. Geiger, "The switchable integrin adhesome," *Journal of Cell Science*, vol. 123, pp. 1385–1388, May 2010.

[89] A. J. Maniotis, C. S. Chen, and D. E. Ingber, "Demonstration of mechanical connections between integrins, cytoskeletal filaments, and nucleoplasm that stabilize nuclear structure," *Proceedings of the National Academy of Sciences*, vol. 94, pp. 849–854, Feb. 1997.

[90] S. Na, O. Collin, F. Chowdhury, B. Tay, M. Ouyang, Y. Wang, and N. Wang, "Rapid signal transduction in living cells is a unique feature of mechanotransduction," *Proceedings of the National Academy of Sciences of the United States of America*, vol. 105, pp. 6626–6631, May 2008.

[91] R. W. O'Meara, J.-P. Michalski, and R. Kothary, "Integrin Signaling in Oligodendrocytes and Its Importance in CNS Myelination," *Journal of Signal Transduction*, vol. 2011, pp. 1–11, Dec. 2011.

[92] M. Fricker, A. M. Tolkovsky, V. Borutaite, M. Coleman, and G. C. Brown, "Neuronal Cell Death," *Physiological Reviews*, vol. 98, pp. 813–880, Apr. 2018.

[93] M. de Lera Ruiz and R. L. Kraus, "Voltage-Gated Sodium Channels: Structure, Function, Pharmacology, and Clinical Indications," *Journal of Medicinal Chemistry*, vol. 58, pp. 7093–7118, Sept. 2015.

[94] M. M. Aria, "Bioelectricity and excitable membranes," in *Electrophysiology Measurements for Studying Neural Interfaces*, pp. 1–23, Elsevier, 2020.

[95] M. C. LaPlaca, D. K. Cullen, J. J. McLoughlin, and R. S. Cargill, "High rate shear strain of three-dimensional neural cell cultures: A new in vitro traumatic brain injury model," *Journal of Biomechanics*, vol. 38, pp. 1093–1105, May 2005.

[96] J. A. Wolf, P. K. Stys, T. Lusardi, D. Meaney, and D. H. Smith, "Traumatic Axonal Injury Induces Calcium Influx Modulated by Tetrodotoxin-Sensitive Sodium Channels," *The Journal of Neuroscience*, vol. 21, pp. 1923–1930, Mar. 2001.

[97] B. Coste, B. Xiao, J. S. Santos, R. Syeda, J. Grandl, K. S. Spencer, S. E. Kim, M. Schmidt, J. Mathur, A. E. Dubin, M. Montal, and A. Patapoutian, "Piezo proteins are pore-forming subunits of mechanically activated channels," *Nature*, vol. 483, pp. 176–181, Mar. 2012.

[98] M. W. Tibbitt and K. S. Anseth, "Hydrogels as extracellular matrix mimics for 3D cell culture," *Biotechnology and Bioengineering*, vol. 103, pp. 655–663, July 2009.

[99] S. Bosi, R. Rauti, J. Laishram, A. Turco, D. Lonardoni, T. Nieus, M. Prato, D. Scaini, and L. Ballerini, "From 2D to 3D: Novel nanostructured scaffolds to investigate signalling in reconstructed neuronal networks," *Scientific Reports*, vol. 5, p. 9562, Aug. 2015.

[100] A. M. Hopkins, E. DeSimone, K. Chwalek, and D. L. Kaplan, "3D in vitro modeling of the central nervous system," *Progress in Neurobiology*, vol. 125, pp. 1–25, Feb. 2015.

[101] B. Morrison, H. L. Cater, C. D. Benham, and L. E. Sundstrom, "An in vitro model of traumatic brain injury utilising two-dimensional stretch of organotypic hippocampal slice cultures," *Journal of Neuroscience Methods*, vol. 150, pp. 192–201, Jan. 2006.

[102] L. Lossi, S. Alasia, C. Salio, and A. Merighi, "Cell death and proliferation in acute slices and organotypic cultures of mammalian CNS," *Progress in Neurobiology*, vol. 88, pp. 221–245, Aug. 2009.

[103] M. A. Lancaster, M. Renner, C.-A. Martin, D. Wenzel, L. S. Bicknell, M. E. Hurles, T. Homfray, J. M. Penninger, A. P. Jackson, and J. A. Knoblich, "Cerebral organoids

model human brain development and microcephaly," *Nature*, vol. 501, pp. 373–379, Sept. 2013.

[104] Y.-T. L. Dingle, M. E. Boutin, A. M. Chirila, L. L. Livi, N. R. Labriola, L. M. Jakubek, J. R. Morgan, E. M. Darling, J. A. Kauer, and D. Hoffman-Kim, "Three-Dimensional Neural Spheroid Culture: An *In Vitro* Model for Cortical Studies," *Tissue Engineering Part C: Methods*, vol. 21, pp. 1274–1283, Dec. 2015.

[105] M. E. Boutin, L. L. Kramer, L. L. Livi, T. Brown, C. Moore, and D. Hoffman-Kim, "A three-dimensional neural spheroid model for capillary-like network formation," *Journal of Neuroscience Methods*, vol. 299, pp. 55–63, Apr. 2018.

[106] F. Berthiaume and J. R. Morgan, eds., *Methods in Bioengineering: 3D Tissue Engineering*. The Artech House Methods in Bioengineering Series, Boston: Artech House, 2010.

[107] T. Xiao, W. Staub, E. Robles, N. J. Gosse, G. J. Cole, and H. Baier, "Assembly of Lamina-Specific Neuronal Connections by Slit Bound to Type IV Collagen," *Cell*, vol. 146, pp. 164–176, July 2011.

[108] J. A. Mitchel and D. Hoffman-Kim, "Cellular Scale Anisotropic Topography Guides Schwann Cell Motility," *PLoS ONE*, vol. 6, p. e24316, Sept. 2011.

[109] M. Frega, M. Tedesco, P. Massobrio, M. Pesce, and S. Martinoia, "Network dynamics of 3D engineered neuronal cultures: A new experimental model for in-vitro electrophysiology," *Scientific Reports*, vol. 4, p. 5489, May 2015.

[110] N. Prochnow, "Relevance of gap junctions and large pore channels in traumatic brain injury," *Frontiers in Physiology*, vol. 5, 2014.

[111] L. Sun, J. Gao, M. Zhao, J. Cui, Y. Li, X. Yang, X. Jing, and Z. Wu, "A novel cognitive impairment mechanism that astrocytic p-connexin 43 promotes neuronic autophagy via activation of P2X7R and down-regulation of GLT-1 expression in the hippocampus following traumatic brain injury in rats," *Behavioural Brain Research*, vol. 291, pp. 315–324, Sept. 2015.

[112] E. Scemes, S. O. Suadicani, G. Dahl, and D. C. Spray, "Connexin and pannexin mediated cell–cell communication," *Neuron Glia Biology*, vol. 3, pp. 199–208, Aug. 2007.

[113] J. A. Briggs, C. Weinreb, D. E. Wagner, S. Megason, L. Peshkin, M. W. Kirschner, and A. M. Klein, "The dynamics of gene expression in vertebrate embryogenesis at single-cell resolution," *Science*, vol. 360, p. eaar5780, June 2018.

[114] E. Dráberová, L. Del Valle, J. Gordon, V. Marková, B. Šmejkalová, L. Bertrand, J.-P. de Chadarévian, D. P. Agamanolis, A. Legido, K. Khalili, P. Dráber, and C. D. Katsetos, "Class III β-Tubulin Is Constitutively Coexpressed With Glial Fibrillary Acidic Protein and Nestin in Midgestational Human Fetal Astrocytes: Implications for Phenotypic Identity," *Journal of Neuropathology & Experimental Neurology*, vol. 67, pp. 341–354, Apr. 2008.

[115] M. L. Hendrickson, A. J. Rao, O. N. A. Demerdash, and R. E. Kalil, "Expression of Nestin by Neural Cells in the Adult Rat and Human Brain," *PLoS ONE*, vol. 6, p. e18535, Apr. 2011.

[116] D. S. Gary, O. Milhavet, S. Camandola, and M. P. Mattson, "Essential role for integrin linked kinase in Akt-mediated integrin survival signaling in hippocampal neurons: ILK and neuronal survival signaling," *Journal of Neurochemistry*, vol. 84, pp. 878–890, Jan. 2003.

[117] S. Zhang, E. Zhao, and B. A. Winkelstein, "A Nociceptive Role for Integrin Signaling in Pain After Mechanical Injury to the Spinal Facet Capsular Ligament," *Annals of Biomedical Engineering*, vol. 45, pp. 2813–2825, Dec. 2017.

[118] Z. Sun, S. S. Guo, and R. Fässler, "Integrin-mediated mechanotransduction," *Journal of Cell Biology*, vol. 215, pp. 445–456, Nov. 2016.

[119] T. D. Ross, B. G. Coon, S. Yun, N. Baeyens, K. Tanaka, M. Ouyang, and M. A. Schwartz, "Integrins in mechanotransduction," *Current Opinion in Cell Biology*, vol. 25, pp. 613–618, Oct. 2013.

[120] M. A. Hemphill, S. Dauth, C. J. Yu, B. E. Dabiri, and K. K. Parker, "Traumatic Brain Injury and the Neuronal Microenvironment: A Potential Role for Neuropathological Mechanotransduction," *Neuron*, vol. 85, pp. 1177–1192, Mar. 2015.

[121] M. M. Bercu, H. Arien-Zakay, D. Stoler, S. Lecht, P. I. Lelkes, S. Samuel, R. Or, A. Nagler, P. Lazarovici, and U. Elchalal, "Enhanced Survival and Neurite Network Formation of Human Umbilical Cord Blood Neuronal Progenitors in Three-Dimensional Collagen Constructs," *Journal of Molecular Neuroscience*, vol. 51, pp. 249–261, Oct. 2013.

[122] T. J. O'Shaughnessy, H. J. Lin, and W. Ma, "Functional synapse formation among rat cortical neurons grown on three-dimensional collagen gels," *Neuroscience Letters*, vol. 340, pp. 169–172, Apr. 2003.

[123] S. M. O'Connor, D. A. Stenger, K. M. Shaffer, and W. Ma, "Survival and neurite outgrowth of rat cortical neurons in three-dimensional agarose and collagen gel matrices," *Neuroscience Letters*, vol. 304, pp. 189–193, May 2001.

[124] J. H. Lee, H.-S. Yu, G.-S. Lee, A. Ji, J. K. Hyun, and H.-W. Kim, "Collagen gel three-dimensional matrices combined with adhesive proteins stimulate neuronal differentiation of mesenchymal stem cells," *Journal of The Royal Society Interface*, vol. 8, pp. 998–1010, July 2011.

[125] I. Cernak, Z. Wang, J. Jiang, X. Bian, and J. Savic, "Cognitive deficits following blast injury-induced neurotrauma: Possible involvement of nitric oxide," *Brain Injury*, vol. 15, pp. 593–612, July 2001.

[126] G. B. Effgen, C. D. Hue, E. Vogel, M. B. Panzer, D. F. Meaney, C. R. Bass, and B. Morrison, "A Multiscale Approach to Blast Neurotrauma Modeling: Part II: Methodology for Inducing Blast Injury to in vitro Models," *Frontiers in Neurology*, vol. 3, 2012.

[127] J. B. Estrada, C. Barajas, D. L. Henann, E. Johnsen, and C. Franck, "High strain-rate soft material characterization via inertial cavitation," *Journal of the Mechanics and Physics of Solids*, vol. 112, pp. 291–317, Mar. 2018.

[128] I. Akhatov, O. Lindau, A. Topolnikov, R. Mettin, N. Vakhitova, and W. Lauterborn, "Collapse and rebound of a laser-induced cavitation bubble," *Physics of Fluids*, vol. 13, pp. 2805–2819, Oct. 2001.

[129] B. Morrison, H. L. Cater, C. C.-B. Wang, F. C. Thomas, C. T. Hung, G. A. Ateshian, and L. E. Sundstrom, "A tissue level tolerance criterion for living brain developed with an in vitro model of traumatic mechanical loading," *Stapp Car Crash Journal*, vol. 47, pp. 93–105, Oct. 2003.

[130] J. S. Sadick, L. A. Crawford, H. C. Cramer, C. Franck, S. A. Liddelow, and E. M. Darling, "Generating Cell Type-Specific Protein Signatures from Non-symptomatic and Diseased Tissues," *Annals of Biomedical Engineering*, vol. 48, pp. 2218–2232, Aug. 2020.

[131] J. D. Humphrey, E. R. Dufresne, and M. A. Schwartz, "Mechanotransduction and extracellular matrix homeostasis," *Nature Reviews Molecular Cell Biology*, vol. 15, pp. 802–812, Dec. 2014.

[132] S. J. Tan, A. C. Chang, S. M. Anderson, C. M. Miller, L. S. Prahl, D. J. Odde, and A. R. Dunn, "Regulation and dynamics of force transmission at individual cell-matrix adhesion bonds," *Science Advances*, vol. 6, p. eaax0317, May 2020.

[133] S. Okuda, N. Takata, Y. Hasegawa, M. Kawada, Y. Inoue, T. Adachi, Y. Sasai, and M. Eiraku, "Strain-triggered mechanical feedback in self-organizing optic-cup morphogenesis," *Science Advances*, vol. 4, p. eaau1354, Nov. 2018.

[134] L. J. Simpson, J. S. Reader, and E. Tzima, "Mechanical Regulation of Protein Translation in the Cardiovascular System," *Frontiers in Cell and Developmental Biology*, vol. 8, p. 34, Jan. 2020.

[135] O. Chaudhuri, S. T. Koshy, C. Branco da Cunha, J.-W. Shin, C. S. Verbeke, K. H. Allison, and D. J. Mooney, "Extracellular matrix stiffness and composition jointly regulate the induction of malignant phenotypes in mammary epithelium," *Nature Materials*, vol. 13, pp. 970–978, Oct. 2014.

[136] C. E. Brennen, "Cavitation in medicine," *Interface Focus*, vol. 5, p. 20150022, Oct. 2015.

[137] M. K. Nyein, A. M. Jason, L. Yu, C. M. Pita, J. D. Joannopoulos, D. F. Moore, and R. A. Radovitzky, "In silico investigation of intracranial blast mitigation with relevance to military traumatic brain injury," *Proceedings of the National Academy of Sciences*, vol. 107, pp. 20703–20708, Nov. 2010.

[138] M. Rice, E. Arruda, and M. Thouless, "The use of visco-elastic materials for the design of helmets and packaging," *Journal of the Mechanics and Physics of Solids*, vol. 141, p. 103966, Aug. 2020.

[139] J. B. Estrada, C. Barajas, D. L. Henann, E. Johnsen, and C. Franck, "High strain-rate soft material characterization via inertial cavitation," *Journal of the Mechanics and Physics of Solids*, vol. 112, pp. 291–317, Mar. 2018.

[140] M. C. LaPlaca, D. Cullen, J. J. McLoughlin, and R. S. Cargill, "High rate shear strain of three-dimensional neural cell cultures: A new in vitro traumatic brain injury model," *Journal of Biomechanics*, vol. 38, pp. 1093–1105, May 2005.

[141] B. Morrison, B. S. Elkin, J.-P. Dollé, and M. L. Yarmush, "In Vitro Models of Traumatic Brain Injury," *Annual Review of Biomedical Engineering*, vol. 13, pp. 91–126, Aug. 2011.

[142] N. J. Braun, D. Liao, and P. W. Alford, "Orientation of neurites influences severity of mechanically induced tau pathology," *Biophysical Journal*, vol. 120, pp. 3272–3282, Aug. 2021.

[143] Y.-T. L. Dingle, M. E. Boutin, A. M. Chirila, L. L. Livi, N. R. Labriola, L. M. Jakubek, J. R. Morgan, E. M. Darling, J. A. Kauer, and D. Hoffman-Kim, "Three-Dimensional Neural Spheroid Culture: An *In Vitro* Model for Cortical Studies," *Tissue Engineering Part C: Methods*, vol. 21, pp. 1274–1283, Dec. 2015.

[144] G. Taubin, "Estimation of planar curves, surfaces, and nonplanar space curves defined by implicit equations with applications to edge and range image segmentation," *IEEE*

Transactions on Pattern Analysis and Machine Intelligence, vol. 13, no. 11, pp. 1115–1138, Nov./1991.

[145] J. Yang, H. C. Cramer, and C. Franck, "Extracting non-linear viscoelastic material properties from violently-collapsing cavitation bubbles," *Extreme Mechanics Letters*, vol. 39, p. 100839, Sept. 2020.

[146] A. F. Frangi, W. J. Niessen, K. L. Vincken, and M. A. Viergever, "Multiscale vessel enhancement filtering," in *Medical Image Computing and Computer-Assisted Intervention — MICCAI'98* (W. M. Wells, A. Colchester, and S. Delp, eds.), vol. 1496, pp. 130–137, Berlin, Heidelberg: Springer Berlin Heidelberg, 1998.

[147] R. Radke, S. Andra, O. Al-Kofahi, and B. Roysam, "Image change detection algorithms: A systematic survey," *IEEE Transactions on Image Processing*, vol. 14, pp. 294–307, Mar. 2005.

[148] A. K. Landauer, M. Patel, D. L. Henann, and C. Franck, "A q-Factor-Based Digital Image Correlation Algorithm (qDIC) for Resolving Finite Deformations with Degenerate Speckle Patterns," *Experimental Mechanics*, vol. 58, pp. 815–830, June 2018.

[149] J. B. Keller and M. Miksis, "Bubble oscillations of large amplitude," *The Journal of the Acoustical Society of America*, vol. 68, pp. 628–633, Aug. 1980.

[150] A. Prosperetti and A. Lezzi, "Bubble dynamics in a compressible liquid. Part 1. First-order theory," *Journal of Fluid Mechanics*, vol. 168, p. 457, July 1986.

[151] E. S. Gurdjian, H. R. Lissner, F. R. Latimer, B. F. Haddad, and J. E. Webster, "Quantitative Determination of Acceleration and Intracranial Pressure in Experimental Head Injury: Preliminary Report," *Neurology*, vol. 3, pp. 417–417, June 1953.

[152] D. K. Cullen, C. M. Simon, and M. C. LaPlaca, "Strain rate-dependent induction of reactive astrogliosis and cell death in three-dimensional neuronal–astrocytic co-cultures," *Brain Research*, vol. 1158, pp. 103–115, July 2007.

[153] S. E. Leggett, M. Patel, T. M. Valentin, L. Gamboa, A. S. Khoo, E. K. Williams, C. Franck, and I. Y. Wong, "Mechanophenotyping of 3D multicellular clusters using

displacement arrays of rendered tractions," *Proceedings of the National Academy of Sciences*, vol. 117, pp. 5655–5663, Mar. 2020.

[154] R. M. Wright and K. T. Ramesh, "An axonal strain injury criterion for traumatic brain injury," *Biomechanics and Modeling in Mechanobiology*, vol. 11, pp. 245–260, Jan. 2012.

[155] M. B. Panzer, B. S. Myers, B. P. Capehart, and C. R. Bass, "Development of a Finite Element Model for Blast Brain Injury and the Effects of CSF Cavitation," *Annals of Biomedical Engineering*, vol. 40, pp. 1530–1544, July 2012.

[156] R. M. Wright and K. T. Ramesh, "An axonal strain injury criterion for traumatic brain injury," *Biomechanics and Modeling in Mechanobiology*, vol. 11, pp. 245–260, Jan. 2012.

[157] M. I. Khan, S. F. Ferdous, and A. Adnan, "Mechanical behavior of actin and spectrin subjected to high strain rate: A molecular dynamics simulation study," *Computational and Structural Biotechnology Journal*, vol. 19, pp. 1738–1749, 2021.

[158] M. I. Khan, F. Hasan, K. A. H. A. Mahmud, and A. Adnan, "Recent Computational Approaches on Mechanical Behavior of Axonal Cytoskeletal Components of Neuron: A Brief Review," *Multiscale Science and Engineering*, vol. 2, pp. 199–213, Dec. 2020.

[159] Y.-T. Wu and A. Adnan, "Damage and Failure of Axonal Microtubule under Extreme High Strain Rate: An In-Silico Molecular Dynamics Study," *Scientific Reports*, vol. 8, p. 12260, Dec. 2018.

[160] D. M. Geddes, R. S. Cargill, and M. C. LaPlaca, "Mechanical Stretch to Neurons Results in a Strain Rate and Magnitude-Dependent Increase in Plasma Membrane Permeability," *Journal of Neurotrauma*, vol. 20, pp. 1039–1049, Oct. 2003.

[161] D. Ambrosi, G. Ateshian, E. Arruda, S. Cowin, J. Dumais, A. Goriely, G. Holzapfel, J. Humphrey, R. Kemkemer, E. Kuhl, J. Olberding, L. Taber, and K. Garikipati, "Perspectives on biological growth and remodeling," *Journal of the Mechanics and Physics of Solids*, vol. 59, pp. 863–883, Apr. 2011.

[162] S. Budday, R. Nay, R. de Rooij, P. Steinmann, T. Wyrobek, T. C. Ovaert, and E. Kuhl, "Mechanical properties of gray and white matter brain tissue by indentation," *Journal of the Mechanical Behavior of Biomedical Materials*, vol. 46, pp. 318–330, June 2015.

[163] E. Spedden, J. D. White, E. N. Naumova, D. L. Kaplan, and C. Staii, "Elasticity Maps of Living Neurons Measured by Combined Fluorescence and Atomic Force Microscopy," *Biophysical Journal*, vol. 103, pp. 868–877, Sept. 2012.

[164] H. Ouyang, E. Nauman, and R. Shi, "Contribution of cytoskeletal elements to the axonal mechanical properties," *Journal of Biological Engineering*, vol. 7, p. 21, Dec. 2013.

[165] R. Bernal, P. A. Pullarkat, and F. Melo, "Mechanical Properties of Axons," *Physical Review Letters*, vol. 99, p. 018301, July 2007.

[166] S. Nam, K. H. Hu, M. J. Butte, and O. Chaudhuri, "Strain-enhanced stress relaxation impacts nonlinear elasticity in collagen gels," *Proceedings of the National Academy of Sciences*, vol. 113, pp. 5492–5497, May 2016.

[167] D. Velegol and F. Lanni, "Cell Traction Forces on Soft Biomaterials. I. Microrheology of Type I Collagen Gels," *Biophysical Journal*, vol. 81, pp. 1786–1792, Sept. 2001.

[168] G. Lai, Y. Li, and G. Li, "Effect of concentration and temperature on the rheological behavior of collagen solution," *International Journal of Biological Macromolecules*, vol. 42, pp. 285–291, Apr. 2008.

[169] A. A. Salomé Machado, V. C. A. Martins, and A. M. G. Plepis, "Thermal and Rheological Behavior of Collagen. Chitosan blends," *Journal of Thermal Analysis and Calorimetry*, vol. 67, no. 2, pp. 491–498, 2002.

[170] Y.-B. Lu, K. Franze, G. Seifert, C. Steinhauser, F. Kirchhoff, H. Wolburg, J. Guck, P. Janmey, E.-Q. Wei, J. Kas, and A. Reichenbach, "Viscoelastic properties of individual glial cells and neurons in the CNS," *Proceedings of the National Academy of Sciences*, vol. 103, pp. 17759–17764, Nov. 2006.

[171] K. Xu, G. Zhong, and X. Zhuang, "Actin, Spectrin, and Associated Proteins Form a Periodic Cytoskeletal Structure in Axons," *Science*, vol. 339, pp. 452–456, Jan. 2013.

[172] I. Peng, L. I. Binder, and M. M. Black, "Biochemical and immunological analyses of cytoskeletal domains of neurons.," *Journal of Cell Biology*, vol. 102, pp. 252–262, Jan. 1986.

[173] H. Ahmadzadeh, D. H. Smith, and V. B. Shenoy, "Viscoelasticity of Tau Proteins Leads to Strain Rate-Dependent Breaking of Microtubules during Axonal Stretch Injury: Predictions from a Mathematical Model," *Biophysical Journal*, vol. 106, pp. 1123–1133, Mar. 2014.

[174] L. Mancia, E. Vlaisavljevich, N. Yousefi, M. Rodriguez, T. J. Ziemlewicz, F. T. Lee, D. Henann, C. Franck, Z. Xu, and E. Johnsen, "Modeling tissue-selective cavitation damage," *Physics in Medicine & Biology*, vol. 64, p. 225001, Nov. 2019.

[175] C. Barajas and E. Johnsen, "The effects of heat and mass diffusion on freely oscillating bubbles in a viscoelastic, tissue-like medium," *The Journal of the Acoustical Society of America*, vol. 141, pp. 908–918, Feb. 2017.

[176] I. Akhatov, O. Lindau, A. Topolnikov, R. Mettin, N. Vakhitova, and W. Lauterborn, "Collapse and rebound of a laser-induced cavitation bubble," *Physics of Fluids*, vol. 13, pp. 2805–2819, Oct. 2001.

[177] X. Nie, B. Sanborn, T. Weerasooriya, and W. Chen, "High-rate bulk and shear responses of bovine brain tissue," *International Journal of Impact Engineering*, vol. 53, pp. 56–61, Mar. 2013.

[178] D. F. Meaney, B. Morrison, and C. Dale Bass, "The Mechanics of Traumatic Brain Injury: A Review of What We Know and What We Need to Know for Reducing Its Societal Burden," *Journal of Biomechanical Engineering*, vol. 136, p. 021008, Feb. 2014.

[179] Z. Wang, J. Estrada, E. Arruda, and K. Garikipati, "Inference of deformation mechanisms and constitutive response of soft material surrogates of biological tissue by

full-field characterization and data-driven variational system identification," *Journal of the Mechanics and Physics of Solids*, vol. 153, p. 104474, Aug. 2021.

[180] M. Fricker, A. M. Tolkovsky, V. Borutaite, M. Coleman, and G. C. Brown, "Neuronal Cell Death," *Physiological Reviews*, vol. 98, pp. 813–880, Apr. 2018.

[181] E. Van Goethem, R. Poincloux, F. Gauffre, I. Maridonneau-Parini, and V. Le Cabec, "Matrix Architecture Dictates Three-Dimensional Migration Modes of Human Macrophages: Differential Involvement of Proteases and Podosome-Like Structures," *The Journal of Immunology*, vol. 184, pp. 1049–1061, Jan. 2010.

[182] C. Ort, Y. Chen, A. Ghagre, A. Ehrlicher, and C. Moraes, "Bioprintable, Stiffness-Tunable Collagen-Alginate Microgels for Increased Throughput 3D Cell Culture Studies," *ACS Biomaterials Science & Engineering*, vol. 7, pp. 2814–2822, June 2021.